VOLATILES, MAJOR OXIDE, TRACE ELEMENT AND ISOTOPE GEOCHEMISTRY IN THE SNAKE RIVER PLAIN AND COLUMBIA RIVER FLOOD BASALTS: IMPLICATIONS FOR THE EVOLUTION OF A CONTINENTAL HOTSPOT.

by

Christopher J. Stefano

A dissertation submitted in partial fulfillment
of the requirements for the degree of
Doctor of Philosophy
(Geology)
in The University of Michigan
2010

Doctoral Committee:

Professor Samuel B. Mukasa, Chair
Professor Rodney C. Ewing
Professor Rebecca A. Lange
Professor Lumin Wang
Professor Youxue Zhang

For Dad

Acknowledgements

First, I'd like to thank my advisor, Sam Mukasa, for giving me this opportunity to pursue a higher education at the University of Michigan. Also thanks to my committee members, Becky Lange, Youxue Zhang, Rod Ewing and Lumin Wang for their valuable input, that has greatly enriched and improved this manuscript. Several fellow graduate students also read parts of this manuscript and made suggestions that were essential, Sarah Rilling being perhaps the most important. Alex Andronikov helped in the field with the collection of the samples for this project, assisted in lab work, and provided input to the manuscript, and for these contributions I am most grateful.

To my college geology professors, Richard Heimlich, Ernie Carlson, Joe Ortiz, and Pete Dahl, for taking an interest in me, and getting me excited about a wide variety of subfields of geology. Without their enthusiastic support, graduate school may not have sounded like such a great idea.

Thanks also to my parents, who nurtured my curiosity and early obsession with dinosaurs, opening the door for my becoming a geologist. Particular thanks go to my father, Ron Stefano, who taught me (not always in the most orthodox ways!) to

question those in authority and established thought, and also never to give up. He was no scientist, but his keen interest in the sciences (and the occasional alien) kept me thinking.

There is no one deserving of greater thanks, for more reasons, than my wife, Cara Stefano. Not only is she the woman I love; not only has she put up with my obsession with geology and all that that entails, as well as my other idiosyncrasies; provided six years of moral support without which I could never have finished; she has also probably read this manuscript for grammar and typos more times than I have!

TABLE OF CONTENTS

LIST OF FIGURES

LIST OF TABLES

LIST OF APPENDICES

Abstract

It is becoming increasingly clear that volatiles, such as H_2O, CO_2, S, Cl, and F, play a major role in both the formation and evolution of mantle melts, and therefore, also in the formation and evolution of the Earth's crust. Volatile availability defines where melting is most likely to occur. It also directly drives melting in volcanic arcs associated with subduction zones. It has also become clear that "dry" melting is uncommon except at mid-ocean ridges. Although the body of knowledge surrounding volatile budgets in arc and MORB lavas has grown significantly in recent years, there remains only limited data for hotspots, particularly those that penetrate continental crust. The first part of this study reports volatile data, in concert with major oxide and trace element data, from olivine-hosted melt inclusions in basaltic lavas of the Snake River Plain (SRP) and the Columbia River Basalts (CRB), which are believed to be the surface expressions of the Yellowstone hotspot. Almost all samples analyzed record minimum H_2O concentrations in excess of 1 wt%, exceeding the largest values obtained for sub aerial eruptions in Hawaii of 0.8 wt%. The most H_2O rich lava in the SRP had 3.3 wt%, and in the Columbia River Basalts (CRB) values reach 4.2 wt% H_2O. Furthermore, these highest values are always found in the less differentiated melt inclusions, based on major oxide and trace element abundances, indicating that the volatiles are of deep origin, not

artifacts of crystallization in the upper crust. These highest values represent some of the largest H_2O concentrations yet observed outside of an arc-related setting. The last part of this study presents new Sr, Nd and the first Hf isotope data for basalts of the CRB and SRP as well as new $^{40}Ar/^{39}Ar$ dates to further constrain petrogenesis and eruption history. These data strongly support the conclusion that CRB and SRP lavas have undergone significant interaction with the crust in the area. This is supported by west to east change in Sr, Nd and Hf isotopic compositions in concert with the transition from accreted arc terranes in the west to North American Craton in the east. The Sr, Nd and Hf isotopic compositions are also related with H_2O data generated in the first part of the study. The result is a revelation that the surface expression of the Yellowstone hotspot may be strongly influenced by the availability of volatiles, particularly H_2O, left over from previous subduction events in the region. It is expected that other hotspots that penetrate areas where there has been previous subduction may also preserve records of a strong volatile influence.

Chapter 1

Introduction

The Yellowstone hotspot, resulting in the Columbia River Basalts (CRB) and Snake River Plain (SRP) basalts (Fig. 1.1) is perhaps the world's best studied feature of its kind on the continents. Its young age (<17 Ma), minimal alteration of the rocks, excellent exposure, and accessibility have all factored into the large number of studies so far produced on its eruptive products. Despite being well studied, however, many questions remain regarding the Yellowstone hotspot, not least of which is whether or not it is the result of a deep-seated mantle plume. Although there is now significant evidence in favor of a plume origin for this feature (e.g., Craig et al., 1978; Jordan et al., 2004; Yuan & Dueker, 2005), some dissenters remain (e.g., Christiansen et al., 2002). The study reported here was designed to delve into details of the petrogenetic processes involved in the Yellowstone hotspot, thereby providing a deeper understanding of its origin and evolution. For a more complete understanding of this, estimates of the volatile budget of the region are critical. Volatiles change melting parameters fundamentally, and their presence or absence is one of the most important driving forces behind the differences in arc basalts and MORB.

Volcanism began in the CRB province at ~17 Ma with the eruption of the Steens Basalts in southeastern Oregon; this is interpreted to represent the time at which impingement of the mantle plume head against the lithosphere occurred (Geist and Richards, 1993; Camp, 1995; Dodson et al., 1997; Camp and Ross, 2004; Brueseke et al. 2007). Volcanism then propagated eastward along the SRP as the North American Plate moved westward over the plume tail. Volcanism peaked with the eruption of the volumetrically dominant Grande Ronde basalts around the tri-state region of Washington, Oregon and Idaho in the northwestern United States at ~17-16 Ma. It then continued at progressively smaller volumes to the present, totaling ~200,000 km^3 of lavas (Reidel 1983; Mangan et al. 1986; Hooper 2002). The earliest basalts (Imnaha, Grande Ronde), which erupted over a ~1.5-My period, make up the bulk of that volume, and tend to be more evolved than the younger lavas (Saddle Mountains, Basalt of Malheur Gorge, etc.) (Hooper et al. 1993). Grande Ronde basalt, the volumetrically dominant unit of the CRB, is basaltic andesite in composition. It is largely aphyric, with a few phenocrysts in a limited number of areas. Late basalts of the region are generally more primitive, with higher abundances of olivine and plagioclase phenocrysts. Unlike earlier basalts, late volcanism in the CRB (~14 Ma to present) has been attributed to decompression melting due to Basin and Range extension (Camp et al. 2003). However, late volcanism may still sample the same mantle source region that produced the main-stage lavas of the CRB because of their proximity to the plume basalts.

The SRP is characterized by bimodal volcanism, and in each new area along the propagating hotspot track having been affected in similar ways. Each area went through

an initial phase of explosive rhyolitic eruptions, which produce large calderas, followed by basaltic volcanism which buries the calderas (Leeman, 1982; Christiansen, 2005; Shervais et al., 2006). The SRP calderas were initiated at ~16 Ma, with the McDermitt Caldera, and propagated northeastwards over a distance of some 700 km to the currently active Yellowstone caldera. This rate and trend of 3-4 cm/yr and NE, respectively, approximate the rate and direction (in the opposite sense) of the movement of North American Plate (Leeman, 1982; Pierce and Morgan, 1992).

The two strongest lines of evidence for the mantle plume forming the Yellowstone hotspot are elevated $^{3}He/^{4}He$ ratios as high as 16 R_A in basalts (Craig et al., 1978; Craig, 1993; Graham et al., 2009), and the discovery of a low-velocity anomaly beneath Yellowstone National Park to a depth of 500-600 km by Yuan & Dueker (2005). The plume head and/or lithosphere produce basaltic melts which then penetrate the crust to produce the basaltic volcanism pervasive throughout the region. The rhyolitic volcanism of the SRP is interpreted to have been generated by crustal anatexis resulting from heating by basaltic injection into the lower crust (Leeman, 1982; Carlson, 1984; Hart, 1985; Bonnichsen et al., 2008; Leeman et al., 2008). For example, Nash et al. (2006) interpreted Nd and Hf isotopic compositions of the rhyolites in the province to be consistent with the early inputs of basalt derived from a mantle plume source. Based on these and other geochemical data, as much as 30-40% of the rhyolite volume could be of mantle derivation (i.e., reprocessing of early intruded basaltic magma; Leeman et al., 2008; McCurry and Rodgers, 2009).

Little data exists for the volatile budget of hotspot basalts worldwide, and virtually none in continental settings. Because of the chemical heterogeneity observed in all hotspots (e.g., Weaver 1991; Kovalenko et al. 2007), it should be expected that the volatiles are also heterogeneous, both in concentration and relative proportions. The Yellowstone hotspot is particularly interesting because the associated continental lithosphere had a protracted and complex kinematic and volcanic history prior to impingement of the hypothesized plume against the lithosphere. For example, volatile concentrations in the YSRP magmatic systems could be elevated relative to other hotspots because of the history of subduction, and therefore mantle fluxing, along the Pacific margin of the North American Plate, not far from our study area when Basin and Range extension is palinspastically removed from the current lithospheric configuration.

This dissertation consists of three independent chapters. Chapters 2 and 3 present results of direct measurements of volatile concentrations associated with major oxide and trace element data for olivine-hosted melt inclusions taken from basalt samples collected in the SRP (chapter 2) and CRB (chapter 3). Chapter 4 provides new Sr, Nd and Hf isotopic data for Yellowstone hotspot basalts, along with $^{40}Ar/^{39}Ar$ dates for selected samples, and relates this new data to major oxide and trace element abundances, previous isotopic studies and some of the volatile observations from chapters 2 and 3.

Olivine-hosted melt inclusions provide a unique opportunity to directly measure pre-eruptive volatile concentrations of basaltic rocks, thereby helping to characterize

the source and perhaps even melting processes (Danyushevsky et al. 2002; Hauri 2002; Wallace 2005). Melt inclusions are trapped at depth during growth of olivine crystals. The trapped melt is isolated from the bulk magma and preserves a record of the composition of the magma at that time, although it tends to be modified somewhat by interaction with the host olivine. There is considerable evidence that some silicate melt inclusions may have retained their original volatile content, even in high H_2O environments such as arcs. For example, H_2O concentrations upwards of 8 wt% have been reported in silicate melt inclusions in Cascade and Central American arc magmas (Wallace 2005; Sadofsky et al. 2008; Vigouroux et al. 2008). There have been a number of successful studies using olivine-hosted melt inclusions to address the volatile budgets of arcs (Wallace 2007; Portnyagin et al. 2007; Sadofsky et al. 2008; Vigouroux et al. 2008), oceanic hotspots (Hauri et al. 2002; Moune et al. 2007), and MORBs (Kamenetsky and Gurenko, 2007).

Olivine is ideal for studies of melt inclusions because it crystallizes first in most basalt compositions (i.e., it is on the liquidus) and traps melt inclusions before extensive evolution of the magma. Evolution occurs as a result of any combination of factors, including crystallization/fractionation, degassing, oxidation, and crustal assimilation. Furthermore, olivine does not have any cleavage that may facilitate loss of volatiles from melt inclusions. However, it is important to interpret H_2O concentrations in reference to a proxy for magma evolution, because some crystallization, or other processes, may precede melt entrapment. Measurement of the H_2O and other volatile contents of the inclusion glass allow an estimate of the pre-eruptive volatile

concentration of the magma and provide a window into the nature of the source with respect to volatiles.

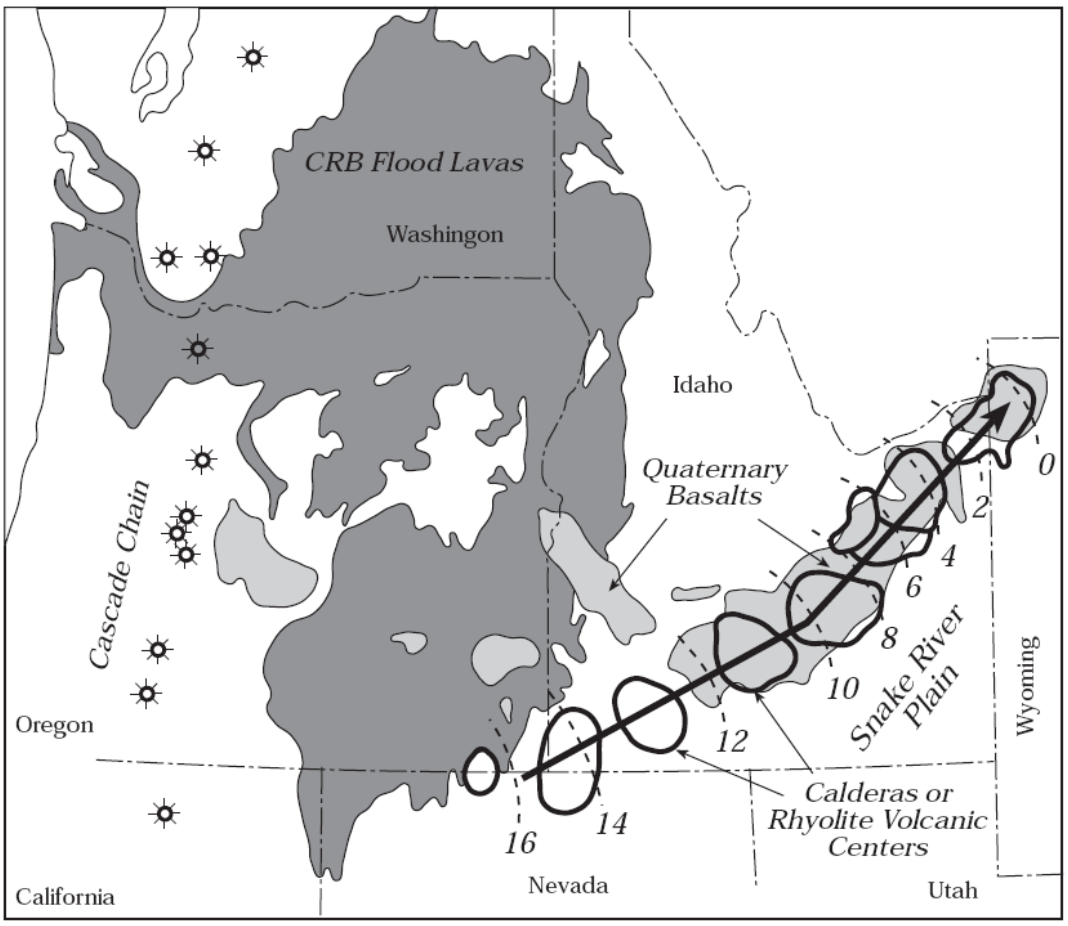

Figure 1.1 A schematic map of the Pacific Northwest region of the United States, showing the Yellowstone hotspot, consisting of the CRB basalts and calderas and basalts of the SRP. Also shown is the Cascades volcanic arc. The proximity of the Yellowstone hotspot track to the Cascades arc suggests the possibility of significant input of arc-derived volatiles into lavas erupted throughout the region.

References

Bonnichsen, B., W. P. Leeman, et al. (2008). "Miocene silicic volcanism in southwestern Idaho: geochronology, geochemistry, and evolution of the central Snake River Plain." Bulletin of Volcanology 70(3): 315-342.

Brueseke, M. E., M. T. Heizler, et al. (2007). "Distribution and geochronology of Oregon Plateau (USA) flood basalt volcanism: The Steens Basalt revisited." Journal of Volcanology and Geothermal Research 161(3): 187-214.

Camp, V. E. (1995). "Mid-Miocene propagation of the Yellowstone mantle plume head beneath the Columbia River Basalt source region." Geology 23(5): 435-438.

Camp, V. E. and M. E. Ross (2004). "Mantle dynamics and genesis of mafic magmatism in the intermontane Pacific Northwest." Journal of Geophysical Research-Solid Earth 109(B8).

Camp, V. E., M. E. Ross, et al. (2003). "Genesis of flood basalts and Basin and Range volcanic rocks from Steens Mountain to the Malheur River gorge, Oregon." Geological Society of America Bulletin 115(1): 105-128.

Carlson, R. W. (1984). "Isotopic Constraints on Columbia River Flood-Basalt Genesis and the Nature of the Subcontinental Mantle." Geochimica Et Cosmochimica Acta 48(11): 2357-2372.

Christiansen, R. L. "The Quaternary and Pliocene Yellowstone Plateau volcanic field of Wyoming, Idaho, and Montana."

Christiansen, R. L., G. R. Foulger, et al. (2002). "Upper-mantle origin of the Yellowstone hotspot." Geological Society of America Bulletin 114(10): 1245-1256.

Craig, H. (1993). "Yellowstone hotspot; a continetal mantle plume." Eos, Transactions, American Geophysical Union 74: 602.

Craig, H., J. E. Lupton, et al. (1978). "Helium Isotope Ratios in Yellowstone Park and Lassen Park Volcanic Gases." Geophysical Research Letters 5(11): 897-900.

Danyushevsky, L. V., A. W. McNeill, et al. (2002). "Experimental and petrological studies of melt inclusions in phenocrysts from mantle-derived magmas: an overview of techniques, advantages and complications." Chemical Geology 183(1-4): 5-24.

Dodson, A., B. M. Kennedy, et al. (1997). "Helium and neon isotopes in the Imnaha Basalt, Columbia River Basalt Group; evidence for a Yellowstone plume source." Earth and Planetary Science Letters 150(3-4): 443-451.

Geist, D. and M. Richards (1993). "Origin of the Columbia Plateau and Snake River plain; deflection of the Yellowstone plume." Geology 21(9): 789-792.

Graham, D. W., Reid, M. R., Jordan, B. T., Grunder, A. L., Leeman, W. P., Lupton, J. E. (2009). "Mantle Source Provinces Beneath the Northwestern USA Delimited by Helium Isotopes in Young Basalts." Journal of Volcanology and Geothermal Research 188(1-3): 128-140.

Hart, W. K. (1985). "Chemical and Isotopic Evidence for Mixing between Depleted and Enriched Mantle, Northwestern USA." Geochimica Et Cosmochimica Acta 49(1): 131-144.

Hauri, E. (2002). "SIMS analysis of volatiles in silicate glasses, 2: isotopes and abundances in Hawaiian melt inclusions." Chemical Geology 183(1-4): 115-141.

Hooper, P. R. and C. J. Hawkesworth (1993). "Isotopic and Geochemical Constraints on the Origin and Evolution of the Columbia River Basalt." Journal of Petrology 34(6): 1203-1246.

Hooper, P. R., G. B. Binger, et al. (2002). "Ages of the Steens and Columbia River flood basalts and their relationship to extension-related calc-alkalic volcanism in eastern Oregon." Geological Society of America Bulletin 114(1): 43-50.

Jordan, B. T., A. L. Grunder, et al. (2004). "Geochronology of age-progressive volcanism of the Oregon High Lava Plains: Implications for the plume interpretation of Yellowstone." Journal of Geophysical Research-Solid Earth 109(B10).

Kamenetsky, V. S. and A. A. Gurenko (2007). "Cryptic crustal contamination of MORB primitive melts recorded in olivine-hosted glass and mineral inclusions." Contributions to Mineralogy and Petrology 153(4): 465-481.

Kovalenko, V. I., V. B. Naumov, et al. (2007). "Volatiles in basaltic magmas of ocean islands and their mantle sources: I. Melt compositions deduced from melt inclusions and glasses in the rocks." Geochemistry International 45(2): 105-122.

Leeman, W. P. (1982). "Development of the Snake River plain-Yellowstone Plateau Province, Idaho and Wyoming; an overview and petrologic model." Bulletin - Idaho Bureau of Mines and Geology 26: 155-177.

Leeman, W. P., C. Annen, et al. (2008). "Snake River plain-Yellowstone silicic volcanism; implications for magma genesis and magma fluxes." Geological Society Special Publications 304: 235-259.

Mangan, M. T., T. L. Wright, et al. (1986). "Regional Correlation of Grande-Ronde Basalt Flows, Columbia River Basalt Group, Washington, Oregon, and Idaho." Geological Society of America Bulletin 97(11): 1300-1318.

McCurry, M., Rogers, D. W. (2009). "Mass transfer along the Yellowstone hotspot track I: Petrologic constraints on the volume of mantle-derived magma." Journal of Volcanology and Geothermal Research 188(1-3): 86-98.

Moune, S., O. Sigmarsson, et al. (2007). "Recent volatile evolution in the magmatic system of Hekla volcano, Iceland." Earth and Planetary Science Letters 255(3-4): 373-389.

Pierce, K. L. and L. A. Morgan (1992). "The track of the Yellowstone hot spot; volcanism, faulting, and uplift." Memoir - Geological Society of America 179: 1-53.

Portnyagin, M., K. Hoernle, et al. (2007). "Constraints on mantle melting and composition and nature of slab components in volcanic arcs from volatiles (H2O, S, Cl, F) and trace elements in melt inclusions from the Kamchatka Arc." Earth and Planetary Science Letters 255(1-2): 53-69.

Reidel, S. P. (1983). "Stratigraphy and Petrogenesis of the Grande-Ronde-Basalt from the Deep Canyon Country of Washington, Oregon, and Idaho." Geological Society of America Bulletin 94(4): 519-542.

Sadofsky, S. J., M. Portnyagin, et al. (2008). "Subduction cycling of volatiles and trace elements through the Central American volcanic arc: evidence from melt inclusions." Contributions to Mineralogy and Petrology 155(4): 433-456.

Shervais, J. W., S. K. Vetter, et al. (2006). "Layered mafic sill complex beneath the eastern Snake River Plain: Evidence from cyclic geochemical variations in basalt." Geology 34(5): 365-368.

Vigouroux, N., P. J. Wallace, et al. (2008). "Volatiles in high-K magmas from the western Trans-Mexican volcanic belt: Evidence for fluid fluxing and extreme enrichment of the mantle wedge by subduction processes." Journal of Petrology 49(9): 1589-1618.

Wallace, P., E. Johnson, et al. (2007). Ascent, degassing, crystallization and eruption of H2O-rich mafic arc magma: A melt inclusion perspective. 17th Annual V M Goldschmidt Conference, Cologne, GERMANY.

Wallace, P. J. (2005). "Volatiles in subduction zone magmas: concentrations and fluxes based on melt inclusion and volcanic gas data." Journal of Volcanology and Geothermal Research 140(1-3): 217-240.

Weaver, B. L. (1991). "The Origin of Ocean Island Basalt End-Member Compositions - Trace-Element and Isotopic Constraints." Earth and Planetary Science Letters 104(2-4): 381-397.

Yuan, H. Y. and K. Dueker (2005). "Teleseismic P-wave tomogram of the Yellowstone plume." Geophysical Research Letters 32(7).

Chapter 2

Water and Other Volatile Systematics of Olivine-Hosted Melt Inclusions from the Yellowstone Hotspot Track

Abstract

Major oxide, trace element and volatile (H_2O, CO_2, S, F, and Cl) compositions have been analyzed for olivine-hosted melt inclusions in eight basalt samples from Yellowstone National Park and the Snake River Plain (SRP) to identify the most primitive melt compositions and assess the volatile budget of the Yellowstone hotspot. These compositions have been evaluated with respect to lithospheric age, thickness and composition for an understanding of potential overprinting effects in the shallow mantle and crust of magmas derived from deeper levels. Maximum water concentrations of 3.3 wt% and CO_2 up to 1677 ppm have been observed in olivine-hosted melt inclusions from the Gerrit Basalts at Mesa Falls, Idaho (SRP region), which is significantly higher than the maximum concentrations measured in other hotspots such as Hawaii (~0.8-0.9 wt%). Water concentrations were generally highest in the least differentiated melt inclusions in terms of incompatible major oxide concentrations, indicating that high water concentrations are characteristic of the mantle or perhaps lower crustal source rather than being products of differentiation, even taking into account the fact that water behaves as an incompatible element during crystal fractionation. Low water

concentrations in some inclusions that have primitive melt compositions indicate post-entrapment degassing of some of the melt inclusions. Overall, diverse compositions of the studied melt inclusions suggest extensive heterogeneity in the mantle source; this is exhibited both within and between samples. Strong enrichment in Ba coupled with depletion in Th in many of the melt inclusions may indicate that volatiles in the Yellowstone hotspot have a subduction zone origin.

Introduction

Olivine-hosted melt inclusions provide a unique opportunity to directly measure pre-eruptive volatile concentrations of basaltic rocks, thereby helping to characterize volatile abundance and perhaps even melting processes (Danyushevsky et al. 2002; Hauri 2002; Wallace 2005). Melt inclusions are trapped at depth during growth of olivine crystals. The trapped melt is isolated from the bulk magma and preserves a record of the composition of the magma at that time, although it will be modified to some extent by interaction with the host olivine. The melt inclusions usually consist of glass $\pm$ gas bubbles $\pm$ daughter minerals; homogeneous inclusions are rare. In the case of a tuffaceous eruption, melt inclusions will be rapidly quenched and will remain glassy; therefore they can be studied directly (e.g., Luhr 2001; Sadofsky et al. 2008). Commonly, melt inclusions have undergone some crystallization, and, prior to being analyzed, they must be re-homogenized at elevated temperature and pressure in a piston cylinder apparatus (Danyushevsky et al. 2002).

There is considerable evidence that some silicate-melt inclusions may have retained their original volatile content at the time of entrapment, even in high H_2O environments such as arcs. For example, H_2O concentrations upwards of 8 wt% have been reported in silicate-melt inclusions in Cascade and Central American arc magmas (Wallace 2005; Sadofsky et al. 2008; Vigouroux et al. 2008), corresponding to high saturation pressures. Olivine is ideal for the study of melt inclusions because it crystallizes first in most basalt compositions and traps melt inclusions before extensive evolution occurs in the magma as a result of crystallization/fractionation, degassing, oxidation, or crustal assimilation. Furthermore, olivine does not have any cleavage that may facilitate loss of volatiles from melt inclusions. However, it is important to interpret H_2O concentrations in reference to a proxy for magma evolution, because some crystallization or other processes may precede melt entrapment. Measurement of the H_2O and other volatile contents of the inclusion glass preserved either from the time of magma crystallization or produced through homogenization, allow estimation of the pre-eruptive volatile concentration of the magma, and provide a window into the nature of the source with respect to volatiles. However, care must be taken when interpreting H_2O data from silicate-melt inclusions because a significant amount of diffusion may have occurred either during magma ascent or during the re-homogenization process in the laboratory. Dissociation of water in the inclusion glass might result in diffusion of H^+ to the host mineral with resulting oxidation and consequent precipitation of magnetite or hematite within the inclusions (i.e., oxidation of Fe^{2+}), lowering the original water content of the melt substantially (Sobolev and Danyushevsky,1994; Danyushevsky et al.,

2002). There have been a number of successful studies dealing with the volatile budgets of arcs (Wallace 2007; Portnyagin et al. 2007; Sadofsky et al. 2008; Vigouroux et al. 2008), oceanic hotspots (Hauri et al. 2002; Moune et al. 2007), and MORBs (Kamenetsky and Gurenko, 2007). Not surprisingly, all these studies indicate that arc lavas are a factor of 5-8 more hydrous than ocean island basalts.

This study focuses on the Yellowstone-Snake River Plain (YSRP) volcanic province which has been considered to be a manifestation of a hotspot that penetrates North American continental lithosphere proximal to a convergent boundary with the Juan de Fuca plate (cf. Manea et al., 2009). While some have expressed doubt about a mantle plume origin for the YSRP volcanic province (e.g., Christiansen et al. 2002), many others have presented evidence suggestive of such an origin (e.g., Craig et al. 1978; Jordan et al. 2004; Nash et al. 2006). Some studies have explored the detailed petrogenetic processes resulting in this magmatism (cf. Leeman et al., 2008; Leeman et al., 2009; McCurry and Rodgers, 2009), but critical to such endeavors is knowledge of the magmatic volatile contents.

The province is characterized by bimodal volcanism, consisting of an initial phase of explosive rhyolitic eruptions that produce large calderas, followed by basaltic volcanism that buries the calderas (Leeman 1982; Christiansen 2001; Shervais et al. 2006). Initiation of the calderas was age transgressive from SW (McDermitt Caldera, ~16 Ma) to NE (Yellowstone Caldera, ~2 Ma), over a distance of 700 km, which corresponds to a North American plate velocity of 3-4 cm per year assuming a stationary plume

conduit. This rate and trend approximate well the speed and direction of the North American Plate measured using other methods (Leeman, 1982; Pierce and Morgan, 1992) (Fig. 2.1). Magmatism is interpreted to have commenced with the arrival of the plume head at the base of the lithosphere at ~17 Ma, triggering the eruption of the Columbia River Flood Basalts (Geist and Richards 1993; Camp 1995; Dodson et al. 1997; Camp and Ross, 2004). The observed track of YSRP calderas is commonly attributed to interaction of the plume tail with the migrating lithospheric plate. The rhyolitic volcanism is interpreted to be a result largely of crustal anatexis resulting from injection of basalts into the crust (Leeman, 1982; Carlson 1984; Hart, 1985; Bonnichsen et al., 2008; Leeman et al., 2008). However, elevated $^{3}He/^{4}He$ ratios up to 16 Ra in YSRP basalts (Craig et al., 1978; Craig, 1993; Graham et al., 2009) implicate a sublithospheric source for this tracer. Furthermore, Nash et al. (2006) interpreted Nd and Hf isotopic compositions of the rhyolites in the province to be consistent with the early inputs of magmatic components (i.e., basalt) derived from a mantle plume source. Based on these and other geochemical data as much as 30-40% of the rhyolite volume could be of mantle derivation (e.g., via reprocessing of early intruded basaltic magma; Leeman et al., 2008; McCurry and Rodgers, 2009). Thus, YSRP basaltic magmatism appears to fundamentally drive the entire petrogenetic cycle from its beginning.

The presence of a low-velocity anomaly beneath Yellowstone extending to a depth of 500-600 km (Yuan & Dueker, 2005), has been interpreted as the manifestation of a rising plume elevated in temperature relative to the ambient mantle. However, the presence of a thick lithosphere lid might prevent decompression melting of ascending

plume mantle (Manea et al., 2009). Because the YSRP province transects Basin and Range structures that are observed south and north of the SRP (Leeman 1982; Nash et al. 2006), it is conceivable that YSRP basaltic volcanism is at least partly a consequence of regional extension (Bonnichsen et al., 2008; Leeman et al., 2008; cf. Harry and Leeman, 1995) – perhaps abetted by an upwelling mantle plume (e.g., to account for the heat required to produce anomalous magmatic volumes). On the other hand, Leeman et al. (2009) note petrogenetic, geochemical, and seismic tomographic data that point to derivation of YSRP basalts from shallow (lithospheric mantle) sources that are not unusually hot, in which case the presence of relatively fertile or hydrated mantle sources might explain the voluminous melt productivity associated with this province.

Little data exists for the volatile budget of hotspot basalts worldwide, and virtually none in continental settings. Because of the chemical heterogeneity observed in all hotspots (e.g., Weaver 1991; Kovalenko et al. 2007), it should be expected that the volatiles are also heterogeneous both in absolute concentration and relative proportions. The YSRP track is particularly interesting because the associated continental lithosphere had a protracted and complex kinematic and volcanic history prior to plume impingement against the lithosphere. For example, volatile concentrations in the YSRP magmatic systems could be elevated relative to other hotspots because of the history of subduction and arc volcanism along the Pacific margin of the North American Plate, not far from our study area when Basin and Range extension is palinspastically removed from the current lithospheric configuration. Because the silicic rocks likely do not have a direct link to mantle sources, basalts closely

related in age to the calderas are more likely to provide direct constraints on the volatile budget of the source. However, the earliest basaltic magmas in the YSRP system rarely erupted, presumably due to density filtering by the crust (Leeman et al., 2008). Basaltic lavas that erupted immediately following the initial rhyolite magmatism tend to be somewhat more differentiated and many exhibit evidence of interaction with the crust, suggesting that they may be modified during storage at crustal levels (Leeman, 1982). Relatively primitive and fresh basalts associated with the Yellowstone caldera system were selected for study to assess volatile contents in syn-caldera basaltic magmas. For comparison, several post-caldera basalts from the Snake River Plain were analyzed to evaluate temporal changes in volatile budgets; these basalts tend to be variably differentiated but still relatively primitive. Basic information on the samples studied, including their bulk compositions, is provided in Table 2.1. This paper primarily reports results of Fourier transform InfraRed (FTIR), Electron MicroProbe (EMP), Secondary Ion Mass Spectrometer (SIMS), and Laser Ablation-Inductively Coupled Plasma-Mass Spectrometer (LA-ICP-MS) study of melt inclusions from representative olivine grains separated from these samples.

Methods for Preparation and Homogenization of Olivine-Hosted Melt Inclusions

1. Sample Selection and Homogenization

Approximately 75 olivine grains 425 µm – 1 mm in size were separated from eight basalt samples and individually inspected under reflected light to identify

melt inclusions, which invariably are now crystalline. This required homogenization of melt inclusions in the High Pressure Laboratory at the University of Michigan using the piston cylinder apparatus (see Hui et al. 2008 for calibration). Between 10 and 15 olivine grains were placed in graphite powder at once in a single graphite capsule in a piston cylinder apparatus, using a barium carbonate pressure medium for heating to homogenize the melt inclusions. The charge was heated to 1300° C at a pressure of approximately 6 kbars in less than 1 minute, held there for 18-20 minutes and then quenched to below 200° C within 20 seconds. The temperature of 1300° C was chosen to be significantly above the basalt liquidus (usually in the range of 1100°-1200° C, depending on melt composition including H_2O content) so that melting and homogenization are rapid to minimize volatile diffusion before quench. The olivine grains were then individually mounted in epoxy resin, and then ground and polished until inclusions were exposed on both sides of the mount. Final thicknesses ranged approximately from 20 to 70 μm.

2. Water Analysis by FTIR

Polished melt inclusions were then analyzed at the University of Michigan for H_2O on a Perkin Elmer Spectrum GX FTIR spectrometer microscope attachment in an environment purged with N_2. Typical melt inclusion diameter is 50 μm, and infrared aperture of 20 μm by 20 μm was used. The thickness of the section is measured to a precision of 1 μm. The calibration of Dixon et al. (1995) was used to calculate the H_2O concentrations from the ~3500 cm^{-1} absorbance peak. In general, only one melt

inclusion could be analyzed in a given olivine grain, the exception being two inclusions in sample L00-35-11; the second inclusion was designated as L00-35-11b in TABLE 2.2.

3. Volatile and Trace Element Analysis of the Inclusions by SIMS and LA-ICP-MS

Selected melt inclusions from each sample were analyzed for H_2O, F, Cl and S using a 10 μm Cs^+ ion beam on the Cameca 1280 SIMS at the Woods Hole Oceanographic Institution following the method described in Le Voyer et al. (2008). Additionally four melt inclusions from sample GTMF-4, a Gerrit Basalt were analyzed for CO_2. A set of volatile-rich basaltic glasses was used for the calibration. We observed no systematic difference between the FTIR and SIMS data for inclusions with lower water concentrations (<2 wt%) whereas SIMS gave systematically higher water concentrations for the more water-rich inclusions, the discrepancy increasing with increasing concentration (2.5 wt% vs. 3.3 wt% in the most water-rich inclusion in this study). The difference is attributed to the fact that the Dixon et al. (1995) calibration did not include any glasses containing more than 2.5 wt% H_2O, whereas the SIMS calibration included standards with up to 6.5 wt% H_2O. Therefore, we have opted to report SIMS data for the inclusions with higher water concentrations over FTIR data when available.

A subset of 54 inclusions was analyzed for selected trace elements (Sc, Rb, Sr, Y, Zr, Nb, Ba, La, Ce, Pr, Nd, Sm, Eu, Gd, Dy, Er, Yb, Th, and U) using the laser ablation inductively coupled plasma mass spectrometer (LA-ICP-MS) at Oregon State University. The laser spot size was 50 μm, and the pulse rate was set to 4Hz. Analyses were

calibrated using the ^{43}Ca peak in the sample, while regularly monitoring the BCR-2G and BHVO-2G glass standards, as detailed by Kent et al. (2004).

4. Major Oxide Analysis and Correction for the Inclusions and Host-Olivine Grains

Major oxide concentrations for inclusions and host-olivine grains were determined on a Cameca SX100 Electron Microprobe at the University of Michigan. Measurements were made with an accelerating voltage of 15 kV, a beam current of 4 nA and a 5-µm defocused beam. Counting times were typically 20 seconds, with a sub-counting routine on Na to monitor for potential beam damage to the glasses. The sub-counting routine breaks counts for Na into 5-second increments, allowing the user to note time-dependent shifts in Na count rates that would indicate beam damage to the glass. The sub-counting routine also includes an algorithm that corrects for any beam damage by calculating back to t = 0 for any time-dependent change in Na count rate. Host olivine grains were analyzed in the same way, except that a beam current of 10 nA and a point beam were used. Elemental standardization was achieved with known natural silicate mineral samples.

Most inclusions showed evidence of host-olivine dissolution, thought to have occurred during inclusion homogenization, requiring the data to be corrected in order to achieve more accurate representations of magmatic volatile concentrations. This correction was achieved by incrementally subtracting the composition of the host olivine until the partition coefficient (k_D) for Fe-Mg exchange between the olivine and

glass reached ~0.3, assuming a Fe_2O_3/FeO of 0.18 (Leeman et al., 1976; Ross, 1983). Most inclusions required corrections of less than 10 wt% olivine removal. However, a few inclusions required more extreme corrections of as high as 25 wt% olivine removal. The results on the extent of olivine dissolution in the melt inclusions are roughly consistent with experimental data of diffusive olivine dissolution rate in basaltic melts, which would give dissolution distances of 9 μm in 20 minutes at 1300°C in one dimensional diffusive dissolution in a melt with 9 wt% MgO (Chen and Zhang 2008), especially when the finite melt volume in the inclusion and the MgO concentration difference are considered.

The major oxides and trace elements show much more scatter (Figs 2.2, 2.3 and 2.4) than can be explained by the correction procedure and are therefore interpreted to reflect actual heterogeneities either from the melt source or from crystallization during ascent. Despite the scatter, meaningful trends are evident, and these provide valuable information in deducing the origins of the volatiles measured in the olivine-hosted melt inclusions.

The correction procedure introduces its own error as a result of uncertainty with respect to the actual k_D for Fe/Mg exchange between olivine and liquid (see Toplis, 2005 for details). Even more important is the uncertainty with respect to the actual Fe_2O_3/FeO of the melt inclusions, which must be assumed to perform the correction accurately. Further uncertainty is added because some melt inclusions may have lost iron to sulfide globules, which do not homogenize during the piston cylinder procedure

(Danyushevksy et al. 2002). Sulfides are commonly observed in some inclusions in this study as small black spheres of less than 10% of the volume of the host inclusion. Rare inclusions containing excessive volumes of black spheres were avoided. MgO and FeO concentrations are particularly problematic, ranging to higher and sometimes lower values than seems reasonable for the bulk host basalts. For this reason, we used alkalis (Na_2O and K_2O) as proxies for evolution. Nevertheless, the procedure still resulted in more realistic data for other elements (including volatiles), which are much less sensitive to the assumptions made in the correction due to their absence in olivine. For these reasons FeO, and even more so, MgO, in the data set reported here are not particularly useful in the interpretations, and are shown only in the interest of completeness.

5. Host-Rock Analysis

Major oxides and the trace elements, Rb, Sr, and Zr for the bulk rock lavas were analyzed by x-ray fluorescence (XRF) and trace elements were measured by LA-ICP-MS at the XRF and ICP-HEX-MS Laboratories of the Washington State University Geoanalytical Laboratory following the methods of Knaack et al. (1994) and Johnson et al. (1999).

Results

Corrected major oxide, as well as trace element and volatile data for olivine-hosted melt inclusions and their associated whole rocks from eight basalt flows throughout the Snake River Plain are presented in TABLEs 2.1 and 2.2. The five samples

associated with the current Yellowstone-Island Park caldera complex (Fig. 2.1) are considered to be syn-caldera basalts and are all younger than the Lava Creek Tuff (0.6 Ma). The other three flows, from other parts of the SRP, are much younger than the nearest caldera and are considered to be post-caldera. These basalts may not be directly related to the hotspot, though as stated earlier they could conceivably be remobilized under-plated material originally derived from the hypothesized plume.

1. Olivine Compositions

Host olivine compositions for the syn-caldera melt inclusions show a range of ~Fo_{84-87} (host rock Mg#s range from 47-62). The post-caldera olivine grains are generally less magnesian, but are more heterogeneous, with a range of ~Fo_{69-82} (host rocks ranging 50-55). Forsterite contents in individual samples do not generally vary by more than 3 wt% (the exception being post-caldera sample L05-1, showing as much as 11 wt%), and do not correlate with water.

2. Major Element Compositions of the Melt Inclusions

Major oxide data for both syn-caldera and post-caldera melt inclusions display compositional trends, despite some scatter (Figs. 2.2, 2.3, 2.4). Observed trends show no changes in slope to indicate changes in the dominant crystallizing phase. However, some inclusions have anomalously low FeO for their SiO_2 content, which may indicate the formation of sulfides. However, there is no correlation between the FeO and S concentrations in the melt inclusions, indicating that formation of a sulfide phase within the inclusions is not the principal process governing iron and sulfur variability.

Most melt-inclusion and host-rock compositions fall in the basalt field in a total alkalis vs. silica diagram (Fig. 2.2); however, a wide variety of other compositions also occur. Post-caldera melt inclusions show less heterogeneity but are more alkaline on average than the syn-caldera inclusions, although a couple of extreme alkaline compositions are observed in some syn-caldera inclusions from Yellowstone. The melt inclusions' major oxide compositions are quite variable within a given sample, but the host-rock composition in each case is within the range defined by the melt inclusions found in the sample. Melt inclusions commonly range from less evolved than their host rocks to apparently more evolved (e.g., sample IP-5 has melt inclusions with Na_2O from 1.7 to 6.75 wt%, while the host rock has Na_2O of 2.13 wt%). MgO data are considered to be unreliable largely because of their high sensitivity to the choice of FeO/Fe_2O_3, and are therefore not discussed further here. For this reason we have chosen to use Na and K as the monitors for melt evolution. The wide scatter in the melt inclusion compositions was observed prior to applying the corrections described above, and therefore cannot be due to uncertainties in these corrections. Also, several samples have inclusions with anomalous compositions not easily related to the rest of the data. For example, each of the samples from Yellowstone (OS and AYS samples) yielded a single inclusion with anomalously high Na_2O (~8wt%) and low SiO_2 (~40wt%) (Fig. 2.3).

3. Trace Element Compositions of the Melt Inclusions

Most of the inclusions show trace element patterns that are broadly similar to those of their host rocks, but differences are observed for a few inclusions (Figs. 2.5,

2.6). The variability is particularly noticeable in the syn-caldera melt inclusions. This may indicate compositional heterogeneity of the source region or, more likely, represent microenvironments created by crystallization of the magma. Of particular note are some strong enrichments in Ba (>3000 ppm) for the syn-caldera melt inclusions relative to other inclusions and the host-rock lavas, often accompanied by a depletion in Th (also relative to the host-rock lavas), resulting in very high Ba/Th ratios (500 - >5000). The anomalous inclusion in Yellowstone sample AYS (see above) has one of the more extreme Ba/Th ratios (2573).

All melt inclusions have Ba/La of 15 or higher, with most of the lower values coming from the post-caldera lavas well west of the hypothesized current location of the hotspot at Yellowstone (Fig. 2.1). All three post-caldera rocks have melt inclusions that are generally similar to their host rocks with respect to major oxide and most trace element concentrations, with limited variability compared to the syn-caldera samples. However, the melt inclusions in all three post-caldera samples do show some enrichment in light rare earth elements (LREEs) relative to their respective host-rock compositions. Modest LREE enrichment (La/Sm to 3.5) is observed in some syn-caldera melt inclusions as well, though less pronounced than that observed in the post-caldera inclusions. Notably, two basalts from within Yellowstone show nearly flat REE patterns (Fig. 2.6).

4. Water in the Melt Inclusions

Water concentrations in the studied syn-caldera melt inclusions range from 0.3-3.3 wt%, with most inclusions showing concentrations <1 wt%. However, all samples have inclusions with >1 wt% water. The highest water concentrations (>2 wt%) are observed in flows of the Gerritt Basalt from Mesa Falls, Idaho (Fig. 2.3). More moderate water concentrations are observed in other syn-caldera flows, but all have higher maximum water concentrations than the highest values for post-caldera melt inclusions (Table 2.2). Some syn-caldera melt inclusions show general trends of increasing Na_2O and/or K_2O with decreasing water concentrations (Fig. 2.3), indicating that evolved inclusions are probably variably degassed, and that the observed concentrations should be interpreted as minima for all inclusions, including those with the highest H_2O concentrations. Post-caldera inclusions range from about 0.3 to 1.2 wt% H_2O, with most inclusions having less than 0.6 wt% H_2O. Trends for alkalis vs. H_2O also confirm that more evolved inclusions are variably degassed in the post-caldera inclusions (Fig. 2.4).

5. Other Volatiles in the Melt Inclusions

Sulfur concentrations in the syn-caldera melt inclusions range from <300 to 2,297 ppm. Maximum S in the post-caldera melt inclusions, however, was only 1,209ppm. Sulfide globules were observed in many inclusions, implying that the values reported here have to be minima for each inclusion analyzed. Chlorine concentrations range from 22 to 1100 ppm in the syn-caldera inclusions, though most are under 600 ppm, and from <10 to 614 ppm in post-caldera inclusions. Fluorine concentrations ranged from 92 to 689 ppm in the syn-caldera melt inclusions and from 64 to 1,460 ppm

in post-caldera inclusions. Fluorine is the only volatile analyzed where the higher concentrations are observed in the post-caldera melt inclusions, and may suggest a crustal contribution possibly from the dissolution of apatite. Fluorine concentrations also show a positive correlation with some incompatible elements (particularly K_2O) (Fig. 2.8), indicating that it is not degassing significantly during differentiation. This trend is observed in both syn-caldera and post-caldera melt inclusions. CO_2 was only analyzed in four melt inclusions from sample GTMF-4, ranging from 49.7-1677 ppm.

Discussion

1. Causes of Chemical Variability in Melt Inclusions

There is a great deal of heterogeneity with respect to major oxide, trace element and volatile compositions for the olivine-hosted melt inclusions both in the syn-caldera and post-caldera basalts scattered throughout the eastern Snake River Plain (ESRP). This heterogeneity may result from many factors, as expounded upon in the discussion below. Magmatic degassing may be detectable if it causes crystal growth, which would create trends of decreasing volatile concentrations with increasing concentrations of incompatible elements (Johnson et al. 2008). Fractionation will create commonly observed trends among major oxides, and may also lead to enrichment of volatiles in the residual melt. Another phenomenon, known as the edge effect, is caused by rapid crystal growth which exceeds the diffusion rates of some elements, and can cause the chemistry of the boundary layer of liquid near a crystal to become somewhat different from the bulk liquid. Zhang et al. (1989), Kress and Ghiorso (1995) and Chen and Zhang

(2008) presented data on elemental diffusion rates in basaltic liquids, which have bearing on this process. Because of this edge effect, melt inclusions trapped in this boundary layer will not be perfectly identical to the bulk liquid composition. A sulfide phase can form in trapped sulfur-rich melt inclusions, which primarily influences their composition by removing Fe and S from the residual melt inclusion, causing strongly affected inclusions to show anomalously low Fe and S concentrations (Danyushevsky et al. 2002). Interaction of the melt inclusion with olivine either soon after entrapment or during homogenization in the laboratory will either add host-olivine components to the inclusion or subtract olivine-compatible components from the inclusion, and is manifested primarily as anomalously low or high MgO concentrations. Moreover, this effect will produce anomalous apparent K_D values between olivine and the melt inclusion (Danyushevsky et al. 2002; Schiano et al. 2004; Churikova et al. 2007). Post-entrapment degassing of inclusions will only be detected if most inclusions form a trend between a volatile and some major oxide or trace element, in which case degassed inclusions will plot off the defined trend. This further supports the notion that measured water concentrations for all melt inclusions are minima compared to the actual maximum concentration of the original magma.

2. Post-entrapment Degassing

Evidence for post-entrapment degassing is observed in olivine-hosted melt inclusions from several syn-caldera basaltic samples in this study, in the form of a number of points plotting below the dominant trends (e.g., sample GTMF-2, Fig. 2.3).

There is little evidence for this effect in the drier post-caldera melt inclusions. High CO_2 concentrations observed in two water-rich melt inclusions from sample GTMF-4 indicate that the inclusions had undergone little prior degassing. Because melt inclusions with obvious ruptures were not analyzed, degassing must have occurred either through small, sub-microscopic fractures or by diffusion directly through the olivine, particularly when the inclusion occurred near the edge of a grain. This degassing may have occurred naturally en route to the surface, at the surface but before cooling, contemporaneously with eruption, or artificially during the homogenization process in the laboratory. However, degassing during homogenization should have been minimized by the higher solubility of water in magmas at higher pressure (Moore et al. 1998), and the short time at high temperature. Therefore, the most likely cause of the post-entrapment degassing is diffusion through the olivine grain and/or loss through sub-microscopic fractures at or shortly before the time of eruption (Portnyagin et al. 2008).

3. Major and Trace Element Trends: Equilibrium Crystallization or Edge-Effect Diffusional Exchange?

The observed trends between water and incompatible major oxides and trace elements cannot be explained entirely by edge effects occurring immediately prior to entrapment, which result from rapid crystallization, possibly caused by degassing of water (e.g., Johnson et al. 2008). Invoking edge effects to interpret these data seems unreasonable because no trends such as simultaneous enrichment of Al_2O_3, Na_2O and K_2O (these three show similar behaviors during olivine dissolution, Zhang et al. 1989; Chen and Zhang 2008) are evident. However, it is possible that some of the variability in

composition of lower water melt inclusions could be partially due to edge effects. Because melt inclusions trap only the residual liquid, not crystals produced during fractionation, it is possible for melt inclusions to preserve compositions more evolved than the bulk rock without the need for an edge effect. However, even if edge effects were important, water could easily remain in equilibrium with the bulk magma while incompatible elements shifted to more evolved compositions at the edge of a growing olivine crystal because water has a diffusion rate approximately an order of magnitude greater than most major and trace elements (~10^{-10} m^2/s, compared to ~10^{-11} m^2/s, respectively) (Zhang and Stolper 1991; Chen and Zhang 2008).

Trends observed between elemental (particularly SiO_2, Na_2O, K_2O) and water concentrations in melt inclusions are consistent with equilibrium crystallization of olivine and plagioclase. Trends between major oxide and water concentrations (Figs. 2.3 and 2.4) are generally diffuse, resulting from significant source heterogeneity, and some inclusions are interpreted to have degassed more after entrapment than others. Most major oxides in the syn-caldera basalts show nominally flat trends with respect to water; however, a weak negative correlation is observed between water and highly incompatible major oxides (SiO_2, Na_2O, and K_2O) and trace elements (Sc, U, and Sr) for some of the samples (Figs 2.3 and 2.6). In most of these plots, a flow of the Gerrit Basalt (sample GTMF-2) conforms most closely to the mentioned trends, indicating that samples have been variably affected by crystallization. Post-caldera basalts show similar trends in water versus major oxides (Fig. 2.4), and some diffuse negative correlations are observed in the trace elements Sc, and HREEs (Fig. 2.6). Fluorine behaves differently

compared to the other volatiles during evolution of the magma. Plots of volatile elements vs. incompatible elements (Fig. 2.8), particularly Sc, yield negative correlations, like water, for Cl and S, but a positive correlation for F. Fluorine correlates better with K_2O, which indicates that F is not degassing from magma in a similar manner to the other volatiles. Sadofsky et al. (2008) also observed similar behavior in F for the Central America Arc. These trends are observed in both syn-caldera and post-caldera basalts; although, again, the correlations are not as well developed in melt inclusions from the post-caldera lavas. Plots of K_2O vs. water for data from Vigouroux et al. (2008) also show this trend in the Mexican arc, and in all cases, the highest water concentrations are only observed in the least differentiated inclusions with respect to incompatible element concentrations.

It is important to note that the high water concentrations preserved in some of the melt inclusions rule out the possibility of long storage times in the shallow crust for the host magmas. Demouchy and Mackwell (2003) found water diffusion rates through olivine to be ~10^{-13} m^2/s, which means that water could diffuse through a 1-mm wall of olivine to escape an inclusion in just a few days. Therefore, the observed concentrations support the conclusion that these basalts are not likely to have been stored for very long, at least not after water was degassed. Portnyagin et al. (2008) found that "dry" olivine-hosted melt inclusions placed in a water-bearing melt could gain up to 2.5 wt% water after only two days at 1140° C. Although the conditions in the Portnyagin et al. (2008) study are very unlikely to occur in nature (ascent should be characterized by degassing of the host liquid, not addition of water), these experimental results provide

further evidence of how quickly water can diffuse in or out of a melt inclusion. Severs et al. (2007) found that melt inclusions in quartz from the Bishop Tuff lost most of their water after only seven days of heating at 800° C and one kbar of pressure. Johnson et al. (2008) examined melt inclusions from various stages of an eruption at Volcan Jorullo, Mexico, and found that early-erupted inclusions preserved high-water contents and had very short estimated olivine storage times; later in the eruption more evolved inclusions were found with much less water and much longer estimated storage times. These reports lend further support to the notion that any amount of storage would cause loss of water in melt inclusions. As soon as host magmas to the melt-inclusion-bearing olivine crystals degas their water, melt inclusions will begin to re-equilibrate with the drier magma and will do so on a scale of years to possibly even days. Therefore the only way for the high water concentrations observed in a number of the olivine-hosted melt inclusions from the Yellowstone hotspot to be preserved is for eruption to have occurred within a few days following degassing. Hence, it is expected that only a small proportion of inclusions would be able to maintain high H_2O concentrations.

4. Water-Fluxed Melting?

The association of highest water concentrations with the least differentiated melt inclusions was used by Sadofsky et al. (2008) to argue for water-fluxed melting in arc basalts from Central America. The argument was based on the idea that the addition of water would increase the melt fraction by depressing the peridotite solidus temperature, thereby diluting the concentrations of incompatible elements. High water

concentrations in the Yellowstone syn-caldera melt inclusions do not approach arc values, such as those observed by Sadofsky et al. (2008) and others (up to 6 wt%). Furthermore, host olivine grains in the Central America Arc show much greater heterogeneity in their Fo content than olivine grains in our study (up to 10 wt% compared to only about ±3 wt% in any given sample from the Yellowstone-SRP volcanic province. Melt inclusions from the ESRP and Yellowstone also vary to compositions that are more evolved than the host rocks, a characteristic not observed in the Central America Arc, which indicates that crystallization effects are more important in the olivine-hosted melt inclusions from the SRP. Finally, there is little correlation between Ba/La and water in Yellowstone-ESRP rocks, which in the Central American arc setting Sadofsky et al. (2008) considered to be an even more important indicator of water fluxed melting. It does not seem that water fluxed melting is an appropriate interpretation for the major and trace element trends observed in this study, although it is expected that high water concentration in the mantle source contributed to melt production during mantle upwelling.

5. Mantle Source for Water and Other Volatiles

The results presented here suggest that water and other volatiles were present in the source region for the basalts in the Yellowstone-SRP hotspot track. Water concentrations up to 3 wt% in primitive basaltic melts of the Yellowstone hotspot are much higher than those in Hawaiian basalts (Hauri 2002). Hence, the hotspot basaltic

production is at least partially due to its hydration. In other words, Yellowstone may also be referred to as a “wet spot”.

Because the highest water values are always observed in the least differentiated melt inclusions (e.g., lowest Na_2O and/or K_2O), it is likely that water was present in the source region for these basalts in abundance – as opposed to being an artifact of differentiation processes. H_2O/Ce ratios plotted versus H_2O (Fig. 2.7) also indicate that water concentrations are highest when H_2O/Ce is highest in all cases. Cerium has a similar incompatibility to H_2O (Michael 1995), and therefore H_2O/Ce should remain constant if no other processes (e.g., degassing) remove water. The highest H_2O/Ce in post-caldera melt inclusions are comparable to values found by Michael (1995) in MORB, supporting the mantle origin of H_2O. Also, the few samples on which CO_2 was measured plot on a magmatic degassing curve (Fig. 2.9) as determined by Metrich and Wallace (2008), indicating that water is degassing during ascent as recorded by the melt inclusions. On the other hand, the values in syn-caldera melt inclusions are much higher indicating that water in syn-caldera melt inclusions must come from a source more hydrated than the MORB source. Further support is given by a diffuse positive correlation (actually stronger in post-caldera melt inclusions this time) between chondrite-normalized La/Sm (as high as 3.4) and water concentration (Fig. 2.6), suggesting that garnet is present in the residue, probably left over from melting the mantle to produce the magmas trapped in these melt inclusions (e.g., McKenzie and O’Nions 1991).

Both S and Cl, like water, have their highest abundances in the syn-caldera basalts compared to the post-caldera varieties, although the opposite is true for F. This observation supports the notion that volatiles are coming from a residual source in the mantle that can be depleted by melting. For comparison, maximum Cl values observed in basalts from the Central America Arc (Sadofsky et al., 2008) reach 2275 ppm, while in Hawaii (Hauri, 2002) values only reach 435ppm (for Loihi volcano). Chlorine concentrations in the SRP are intermediate between these two; note, however, that the minimum concentrations observed in the SRP are much lower than those reported for either of the comparison localities, indicating that the post-caldera inclusions are significantly degassed with respect to Cl, if the source is otherwise similar to those in plumes or arcs. The higher Cl concentrations favor a more arc-like source, or at least a component of such a source, rather than a Hawaii-type plume. Maximum S concentrations observed in both Hawaii and the Central America Arc are similar (~2200-3000 ppm and ~2400 ppm, respectively), and SRP melt inclusions also fall in this range.

6. Ba and Th Evidence for Subduction-Related Fluids in Melt Inclusions

Extreme Ba enrichments are observed in inclusions and host rocks from four out of the five syn-caldera lava samples. These enrichments are the most prominent feature of the trace-element patterns (Fig. 2.5) for some of the syn-caldera melt inclusions and host rocks. They are observed in both Gerrit Basalt samples, and in both cases the melt inclusions are otherwise very similar to their host rocks in composition. The fifth of the syn-caldera samples from Yellowstone also shows this Ba enrichment (AYS-4). However,

this inclusion has noticeably different major oxide and trace element compositions compared to the other inclusions in this population. Most significantly, it has anomalously high Na_2O and low SiO_2 (Table 2.2 and Figs. 2.2 and 2.3). This inclusion also shows pronounced negative Ce and Eu anomalies, suggesting fractionation of plagioclase that did not affect the other inclusions. It also has a much higher water concentration than the other inclusions from this rock. However, its host-olivine Fo value falls in the range defined by the other olivine grains from this rock, suggesting that the grain with the anomalous melt inclusion is probably not xenocrystic. Nevertheless, development of this grain in a different magmatic system (in which plagioclase fractionation was important) compared with the other olivine grains with which it is found, is a possibility that should be considered.

Thorium depletion in melt inclusions is observed in four of the five syn-caldera lavas, and is particularly pronounced in the suite of inclusions from sample IP-5 (Fig. 2.5). The melt inclusions from this rock show wider compositional scatter both in major oxides and trace elements than do inclusions from the other rocks (Figs. 2.3 and 2.5, Table 2.2), suggesting either that its source was more heterogeneous and/or that its precursor magma experienced a higher degree of differentiation. The latter possibility may be supported by the presence of flows in this field of more evolved basalts where olivine is absent and large plagioclase crystals are the only phenocrysts. Most of the melt inclusions from sample IP-5 do not show much Ba enrichment relative to the whole rock, but these inclusions do show a very pronounced depletion in Th. While no

significant Ba enrichment in the melt inclusions relative to host rocks was observed for post-caldera basalts, some of the melt inclusions do have small Th depletions.

To understand the origins of the melt-inclusion trace-element characteristics, plots of Ba/La vs. Ba/Nb and Ba/Th vs. Rb/Nb have been prepared (Fig. 2.10), and compared to similar diagrams by Weaver (1991) who defined some mantle end-members using the same trace element space. In the plot of Ba/La vs. Ba/Nb (Fig. 2.10a), the mantle end-members plot on a mixing line between average primitive mantle and average continental crust. Melt inclusions from the SRP define a parallel line slightly above that particular mixing line but with a few points much higher, representing the strongly Ba-enriched melt inclusions. Similar patterns emerge on the Ba/Th vs. Rb/Nb diagram (Fig. 2.10b), where melt inclusions define a near-vertical trend for both syn-caldera and post-caldera basalts. In the syn-caldera basalts, whole rocks also plot high, though extreme compositions occur only in a few of the melt inclusions. Comparing our results on basaltic rocks to data published by Christiansen (2001) for Yellowstone Caldera rhyolites shows contrasting trace element patterns that are not explicable by simple processes, such as extreme crystal fractionation, demonstrating that contamination by components in those rhyolites played no role in producing the observed patterns in our melt inclusions. High Ba/Th ratios and Ba concentrations typify arc basalts as a result of the strong difference in fluid mobility between the two elements. The Yellowstone-SRP samples display patterns similar to those observed in arcs (Walker et al. 2003; Churikova 2007; Sadofsky et al. 2008). The fact that similar patterns are observed in the syn-caldera basalts at Yellowstone suggests that arc or

subduction-related components may be present in the source of the Yellowstone-SRP magmas. This arc component may have been much enriched in alkalis, which may explain the anomalously alkali-rich inclusions in Yellowstone samples AYS and OS.

7. Possible Source of Water and Volatiles in the Mantle

The mantle source for Yellowstone and the SRP is significantly enriched in volatiles when compared with Hawaii, a typical hotspot. Maximum water concentrations in all but one of the sampled rocks, both syn-caldera and post-caldera samples (0.8-3.3 wt%), exceed the maximum concentrations observed in Hawaii of 0.8-0.9 wt% (Hauri 2002), by more than a factor of three if we focus on the maximum values in each case. We reiterate that syn-caldera samples have the highest measured water concentrations (up to 3.3 wt% H_2O). Noting evidence against the late addition of water and other volatiles to the melt inclusions as argued above, the studied Yellowstone-SRP source appears significantly more hydrated than the Hawaiian source. Furthermore, the Yellowstone-SRP source contains a component, recorded particularly well in a few inclusions, that appears to be similar to an arc source. This evidence suggests that the water may not have come from the hypothesized plume, but instead was left behind in the mantle source region during a previous subduction event, and was then either mixed with the rising plume or the plume simply supplied the heat that melted some subduction-fluxed components residing in the upper mantle.

Alternatively, an argument could be made that the plume source harbors subducted components as has been argued by others for a few decades in the case of

ocean islands (e.g., White and Hoffman, 1982; White, 1985; Hoffman et al.., 1986). However, this argument is unsatisfying as an explanation of the high-water abundances in the Yellowstone-SRP melt inclusions because volatiles should be mostly lost by the subducted slab long before its materials can be incorporated into a mantle plume at great depth. Direct participation of such a source cannot be completely ruled out, particularly for the observed trace elements, but seems inadequate to explain the nearly arc-like water concentrations observed.

If we accept a subduction-related origin for the water reported here, then the most likely source for it in the mantle beneath Yellowstone and the SRP is the Farallon slab, thought to be responsible for the Absaroka arc just east of Yellowstone, and other older volcanism in the Northwestern US (Feeley 2003). It is reasonable to infer that all water released by the Farallon slab was not removed from the lithospheric mantle by contemporaneous melting; some residual water was left behind, perhaps in hydrous-phase-bearing veins (cf. Foley, 1992) that were also enriched in Ba and depleted in Th. This material then melted when the hypothesized plume impinged upon the lithosphere and introduced a thermal anomaly into the upper mantle. Melts produced in the lithospheric mantle may then have been contaminated by a plume component – if reported $^{3}He/^{4}He$ values of ~16 R/R_A values in the SRP (Craig et al. 1978; Graham et al., 2009) are representative of the mixing that impacted the principal components in the magmas. In this scenario, only melt inclusions trapped early in the process preserve the signature of primary melts derived from a hydrous lithospheric mantle. The post-caldera melts are lower in water, as they sample a mantle that had undergone melting just a

few million years before during syn-caldera volcanism, and would likely have lost much of their water during that first phase of melting.

Alternatively, Leeman et al. (2009) note isotopic evidence for Archean metasomatism of the SRP lithosphere; therefore it is possible that the water in SRP melts is residual to that event. While we cannot rule out this possibility, it seems less likely, considering the high probability that water would have been removed by earlier melting events during this region's long and complex history of tectonic and volcanic activity.

Conclusions

Melt inclusions from eight basalt samples representing both syn-caldera and post-caldera phases of melting along the Yellowstone-SRP hotspot track have been analyzed for their major oxide, trace element and volatile [H_2O, S, F, and Cl] concentrations. The results have been compared with data obtained from the host rocks, as well as data from the literature for other plume related volcanic provinces to make interpretations on the development of observed trends and also on the sources of the detected volatiles.

Many melt inclusions have significant concentrations of water and other volatiles. Observed water and other volatile concentrations are higher in the syn-caldera basalts than in their post-caldera counterparts, with the exception of F. A significant fraction of the melt inclusions studied have low-volatile concentrations underlining the importance of analyzing many inclusions thereby ensuring that at least a few inclusions

with the maximum volatile concentrations are found. Overall, the concentrations we have reported here for the syn-caldera melt inclusions are higher than those observed in Hawaii (up to 3.3 wt% for Y-SRP vs. 0.9 wt% for Hawaii), but generally lower than the values observed in many arcs (6 wt% or more). Post-caldera melt inclusions have generally lower volatile concentrations, indicating that residual hydration in the upper mantle was largely consumed during the first phase of melting during the caldera-forming eruptive events, in many cases several million years before the second phase of melting along the SRP that is attributed to Basin and Range extension.

Trends observed between volatiles (with the exception of F) and certain major oxides and trace elements indicate that the highest volatile concentrations are associated with the least differentiated melt inclusions, suggesting a mantle source for the volatiles. These trends also suggest considerable degassing of the volatiles from some of the melt inclusions during and following entrapment. The observed compositional trends are explicable by olivine and plagioclase fractionation, most likely triggered by the degassing of volatiles.

Extremely high Ba concentrations, as well as Ba/La, and Ba/Th ratios observed in some melt inclusions and host rocks are consistent with the presence of an arc-related signature. This suggests that volatiles existed as residual hydration of the upper mantle resulting from the subduction of the Farralon slab or some other previous subduction event. The hydration state of the lithosphere beneath the Yellowstone-SRP magmatic province allows for significant melting even if the plume is not particularly hot. The

impingement of the hypothesized plume upon these hydrated upper mantle domains triggered the melting that produced the water-rich and incompatible-element-enriched basalts observed at Yellowstone and the Snake River Plain.

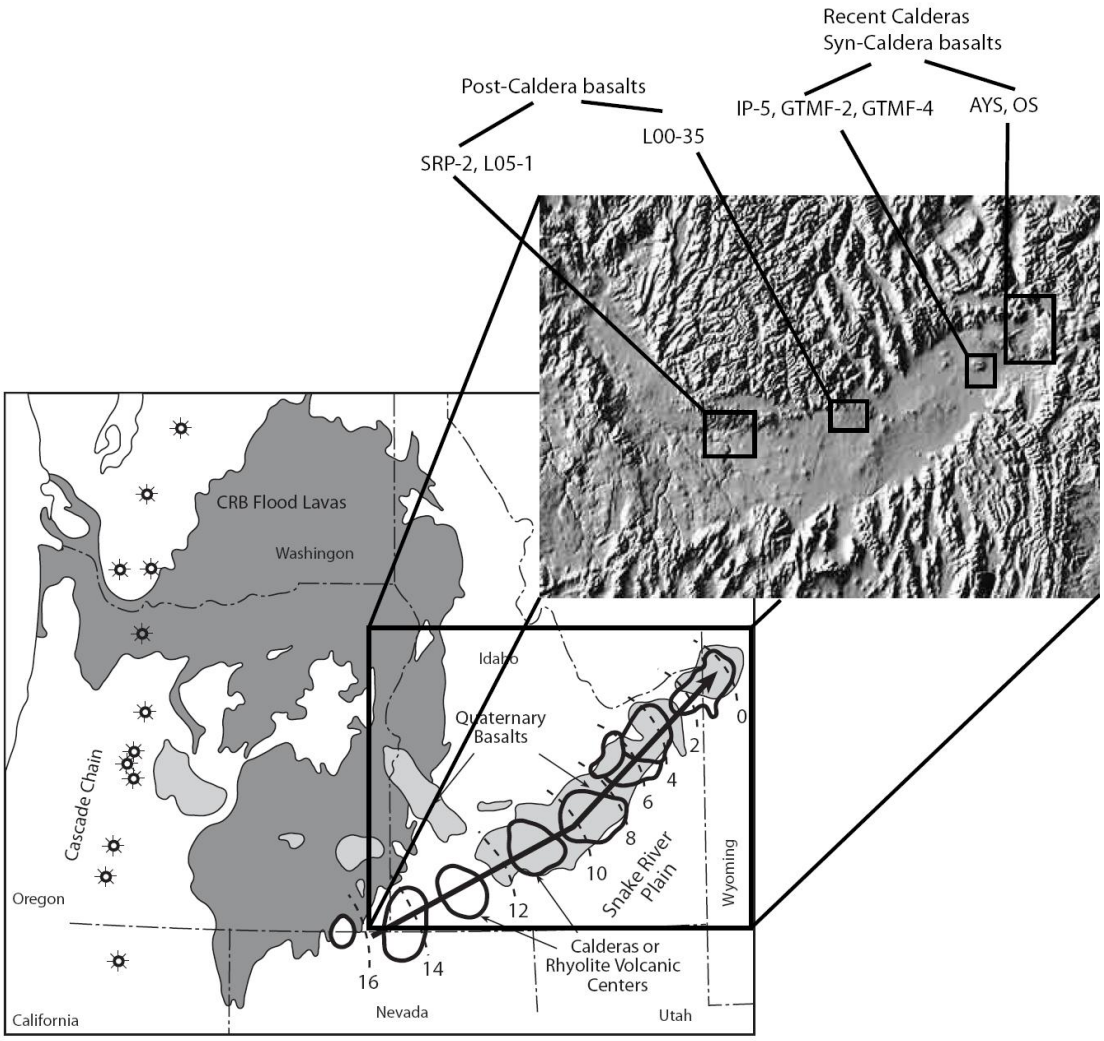

Figure 2.1. Schematic map of the Pacific Northwest region of the United States showing the locations of the Columbia River Basalts (CRB), and the Snake River Plain (SRP). Approximate caldera locations and ages (in Ma) are shown along the Snake River Plain. Also shown is the Cascade arc. The inset shows a DEM of the SRP and the general sample locations for samples used in this study. Modified from Camp and Ross (2004).

A

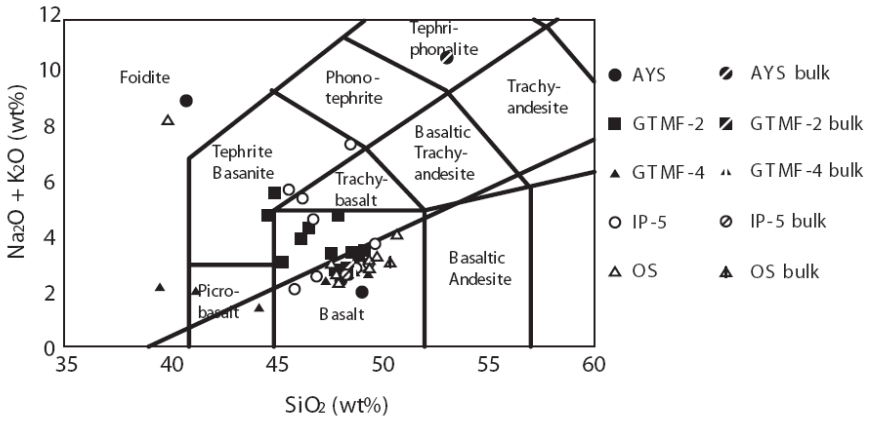

B

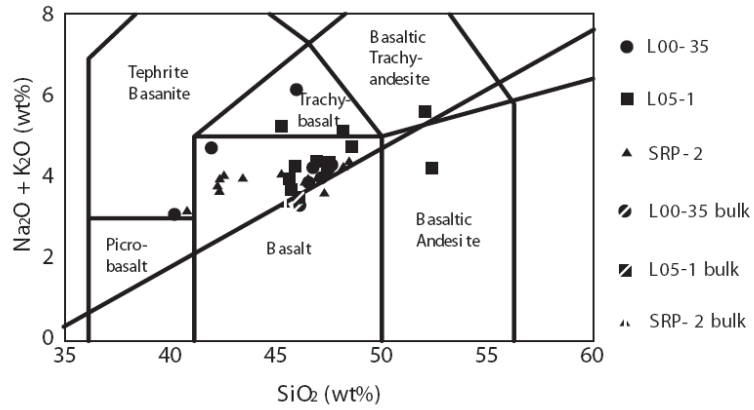

Figure 2.2. Total alkalis vs. Silica plots for syn-caldera (A) and post-caldera (B) melt inclusions and host rocks (labeled “bulk” in the legend). Syn-caldera melt inclusions show greater heterogeneity, including some with highly alkaline compositions.

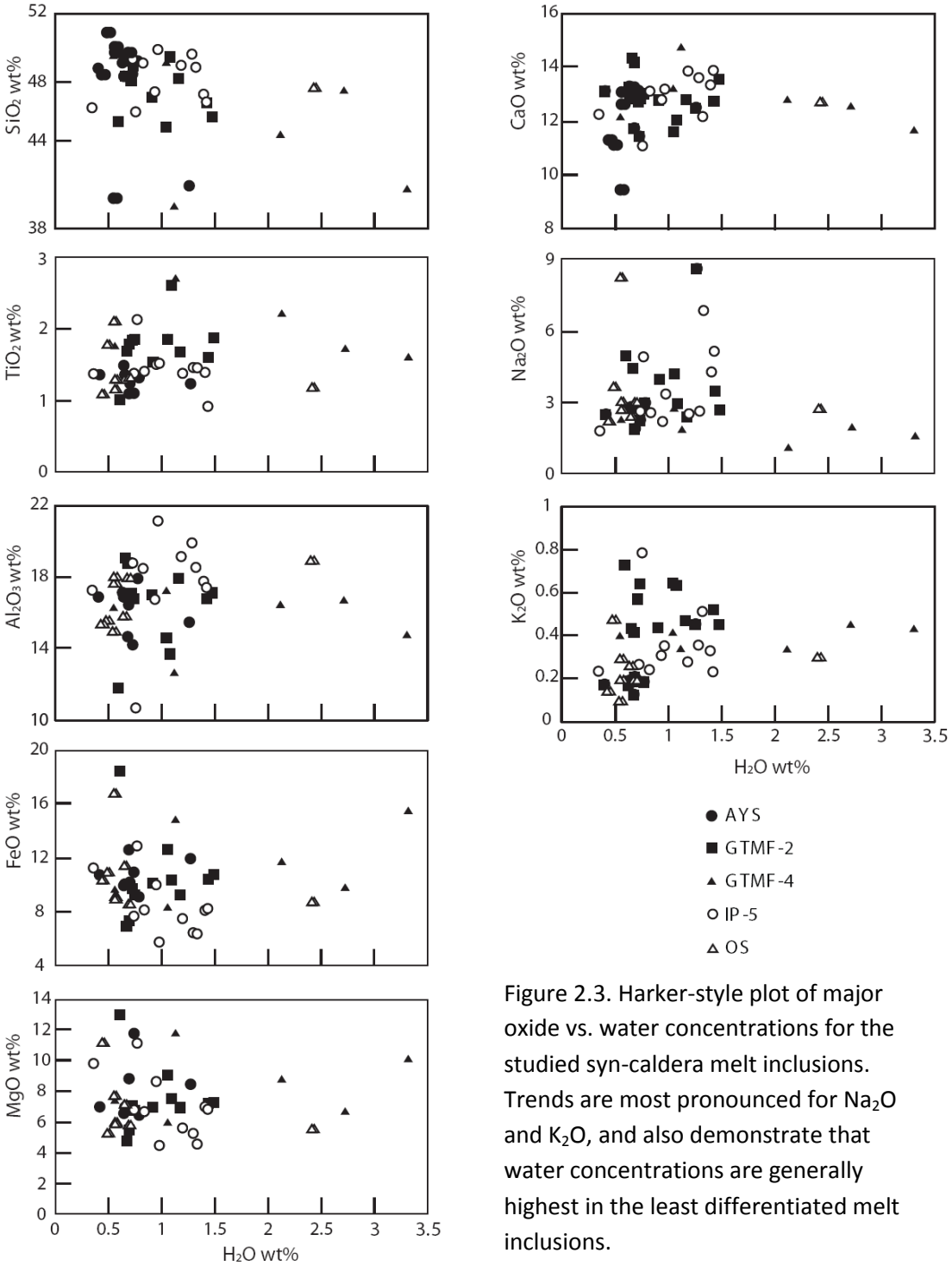

Figure 2.3. Harker-style plot of major oxide vs. water concentrations for the studied syn-caldera melt inclusions. Trends are most pronounced for Na_2O and K_2O, and also demonstrate that water concentrations are generally highest in the least differentiated melt inclusions.

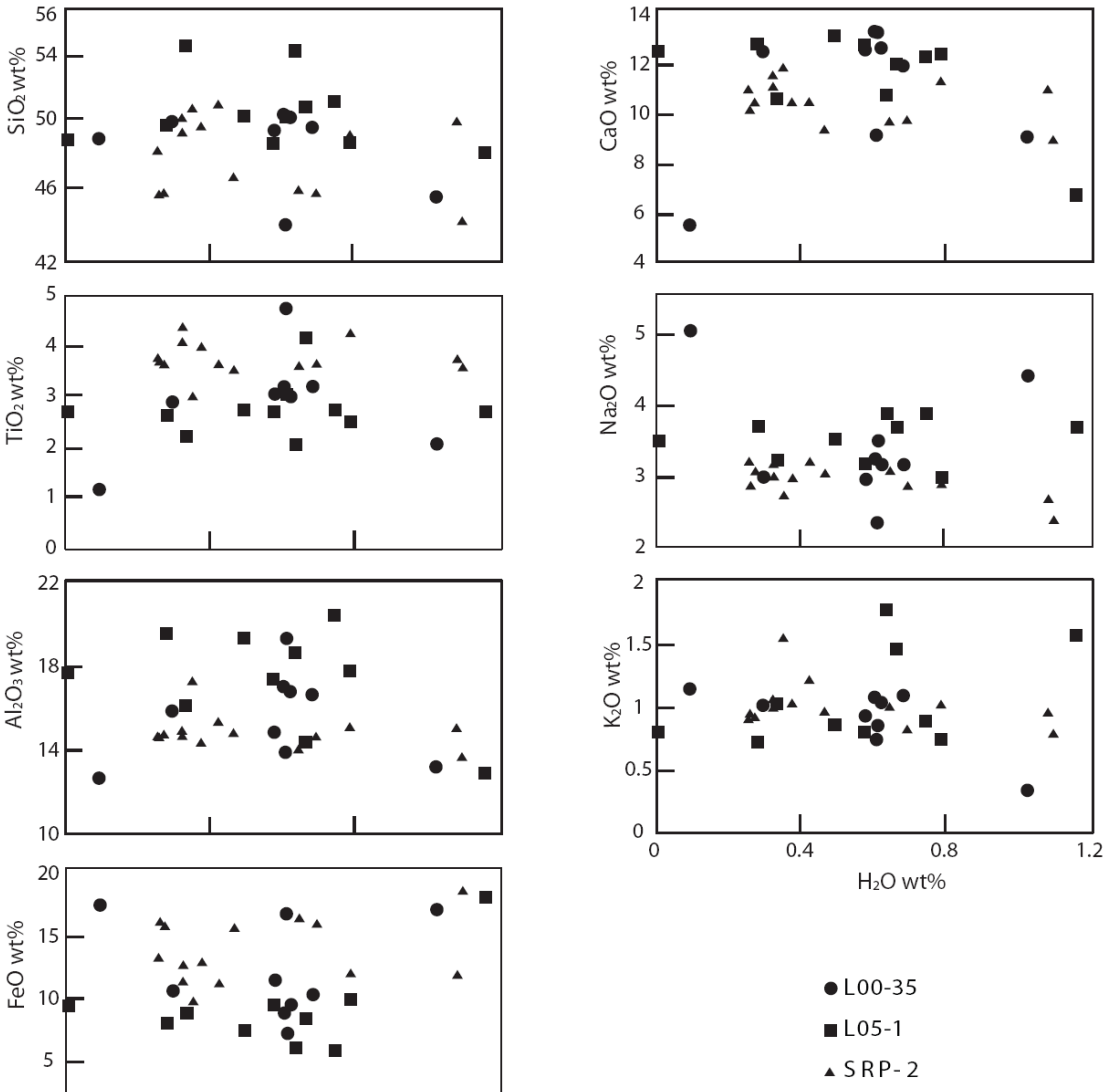

Figure 2.4. Harker-style plot of water versus major oxides for the post-caldera melt inclusions. Trends again indicate highest water concentrations in the least differentiated inclusions these samples.

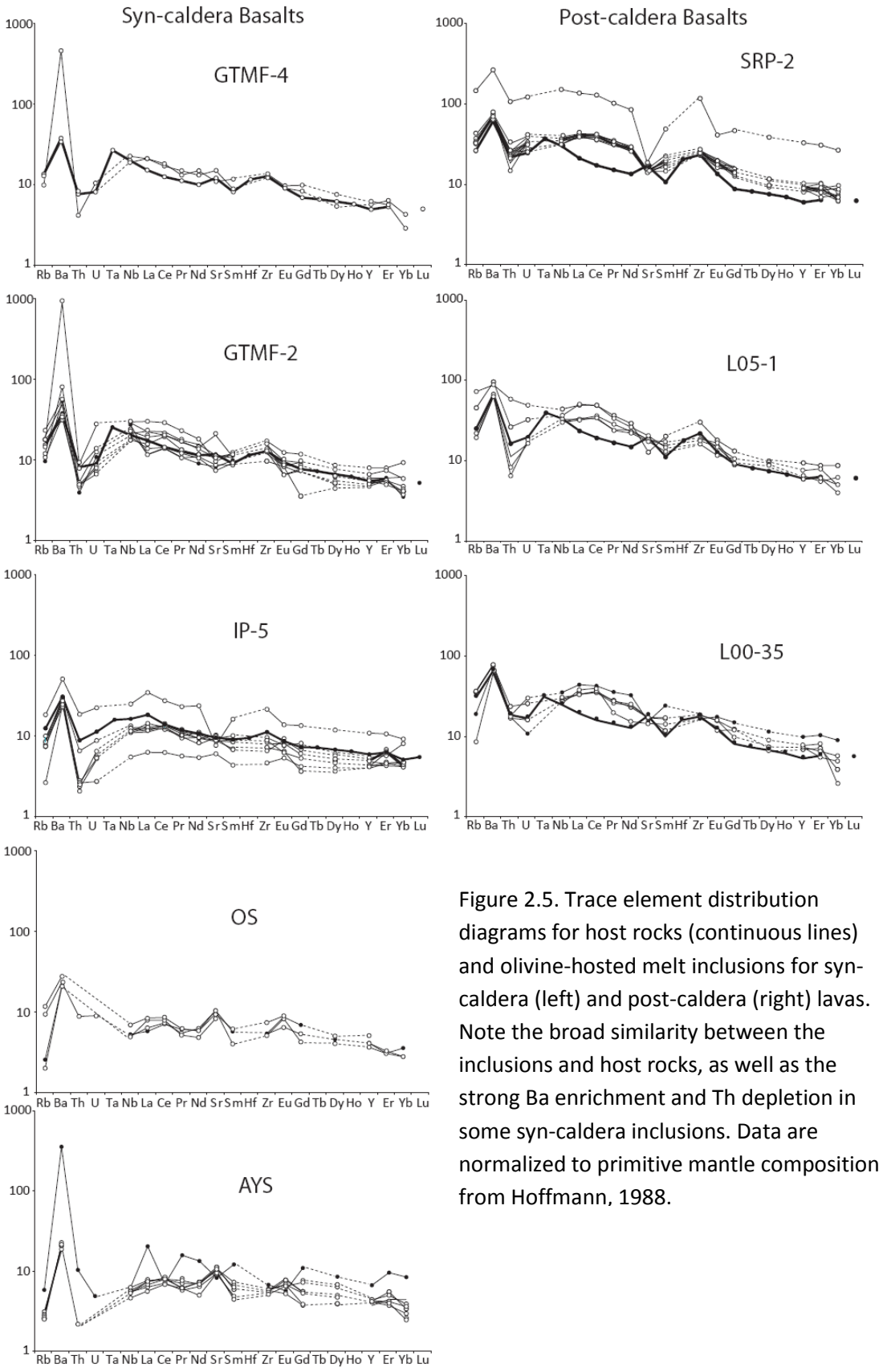

Figure 2.5. Trace element distribution diagrams for host rocks (continuous lines) and olivine-hosted melt inclusions for syn-caldera (left) and post-caldera (right) lavas. Note the broad similarity between the inclusions and host rocks, as well as the strong Ba enrichment and Th depletion in some syn-caldera inclusions. Data are normalized to primitive mantle composition from Hoffmann, 1988.

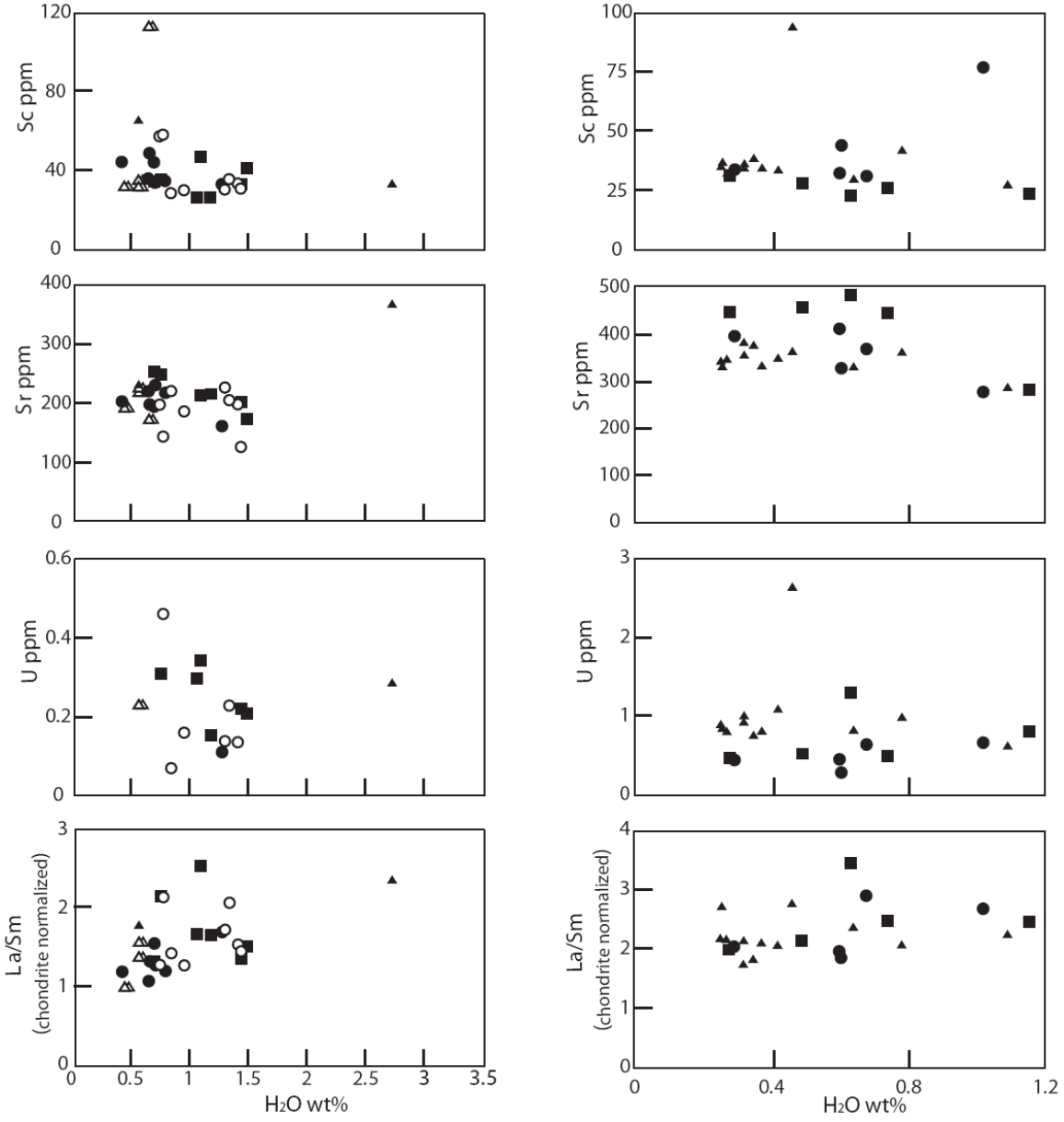

Figure 2.6. Plots of selected trace elements versus water in syn-caldera (left) and post-caldera (right) melt inclusions. Observed trends indicate degassing of water during differentiation. The high La/Sm of water-rich melt inclusions suggests that garnet was present in the residue after melting.

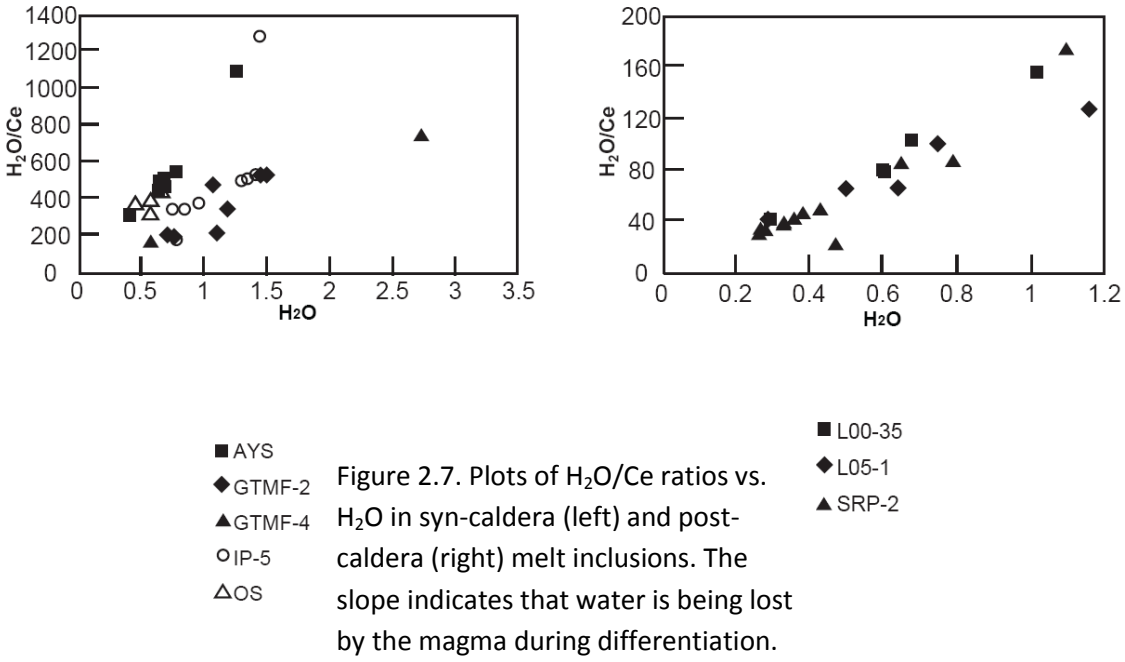

Figure 2.7. Plots of H_2O/Ce ratios vs. H_2O in syn-caldera (left) and post-caldera (right) melt inclusions. The slope indicates that water is being lost by the magma during differentiation.

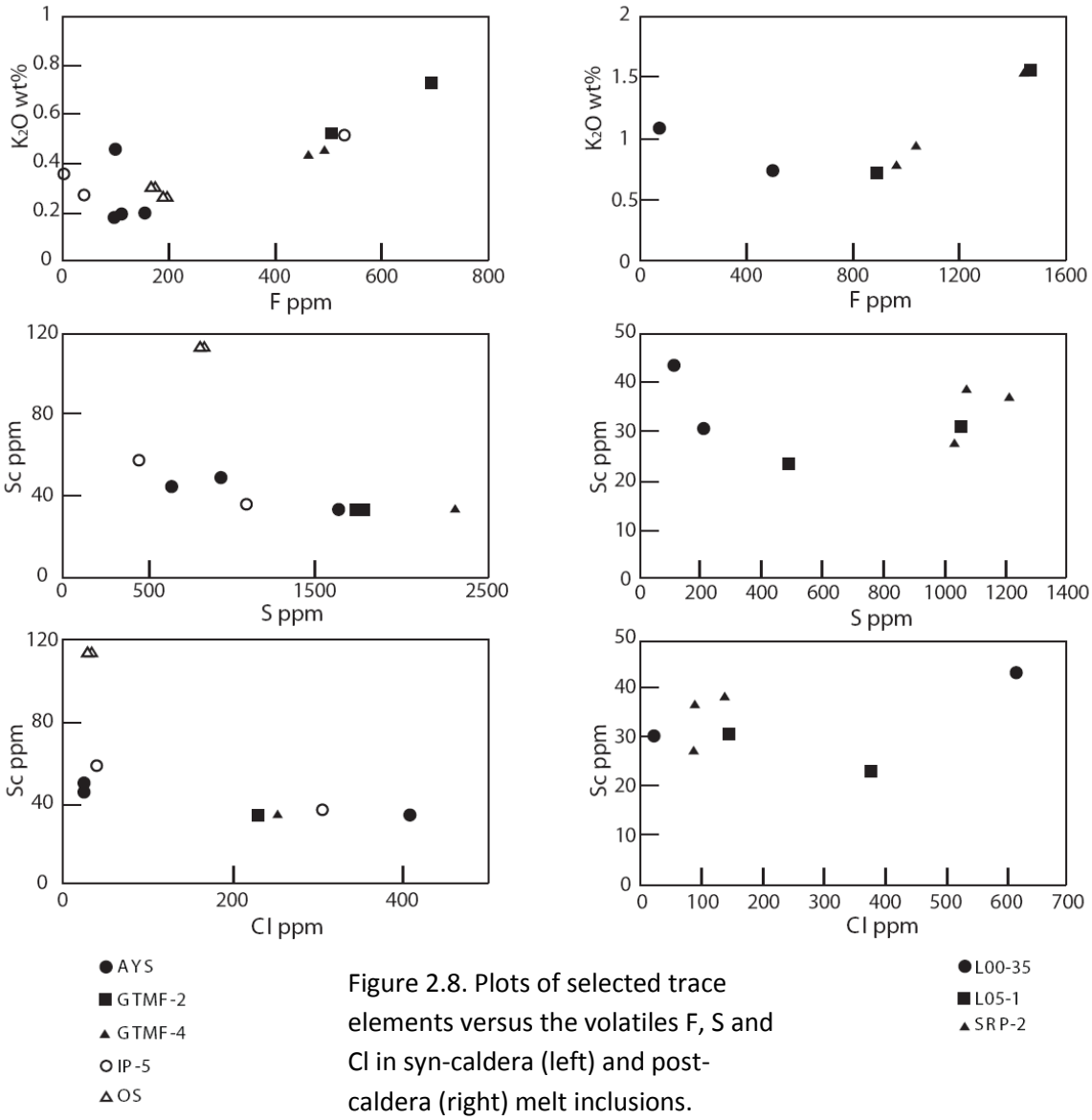

Figure 2.8. Plots of selected trace elements versus the volatiles F, S and Cl in syn-caldera (left) and post-caldera (right) melt inclusions. Observed trends indicate degassing of S and Cl, but quantitative retention of F during differentiation.

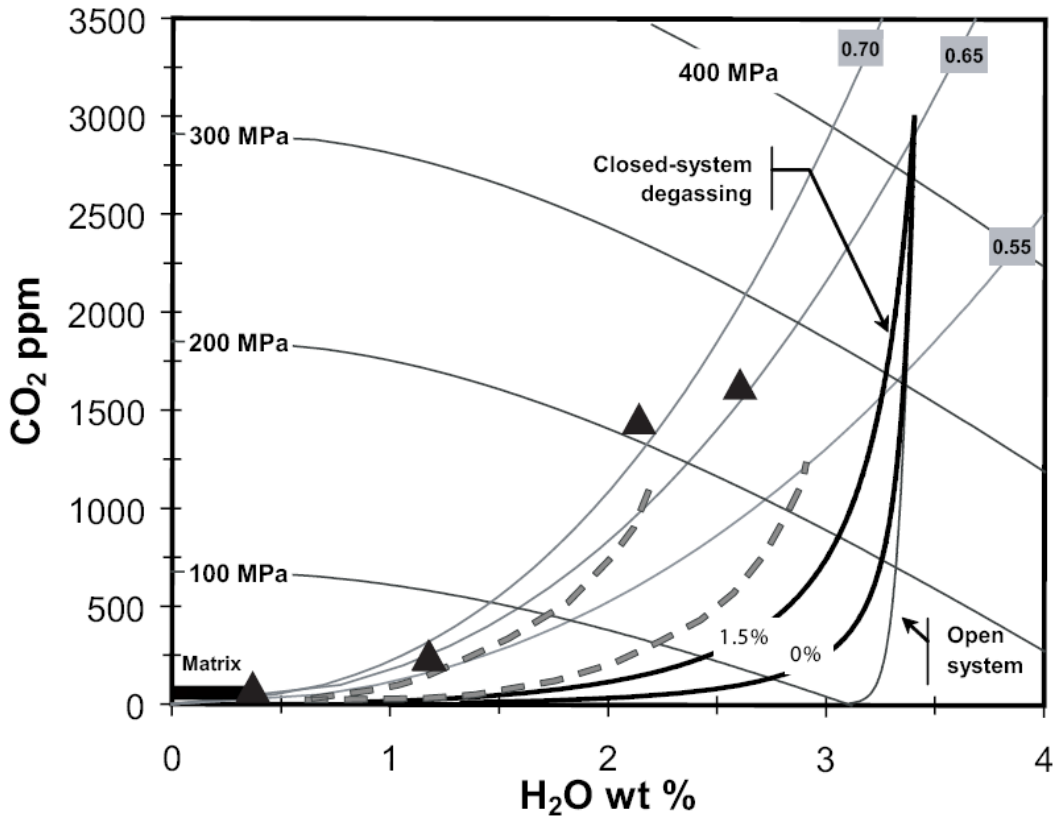

Figure 2.9. Plot of CO_2 vs H_2O concentration for the four melt inclusions from sample GTMF-4. The measured concentrations follow a magmatic degassing curve as determined by Metrich and Wallace (2008).

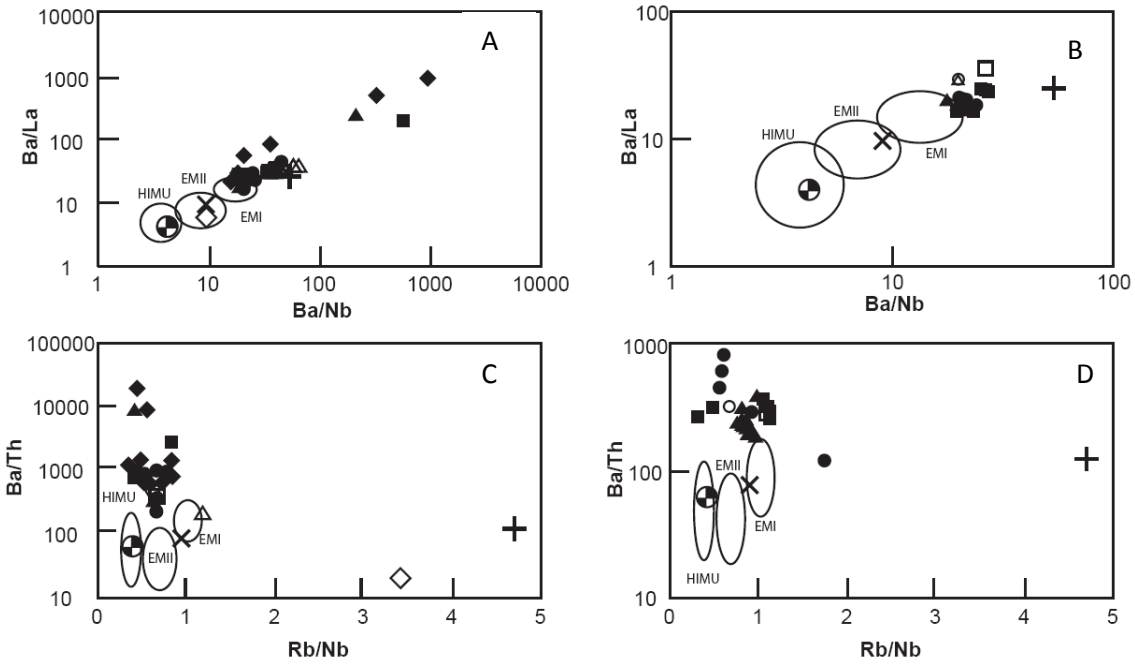

Figure 2.10. Plots of Ba/La vs. Ba/Nb and Ba/Th vs. Rb/Nb for syn-caldera melt inclusions and host rocks (left, A and C) and post-caldera melt inclusions and their host rocks (right, B and D). Also included are estimated compositions for primordial mantle, N-MORB, continental crust (from Weaver 1991) and Yellowstone rhyolites (from Christiansen 2001). The fields for the mantle end members are from Weaver (1991). Note that many inclusions plot away from the fields denoted by the mantle end members, instead exhibiting compositions normally seen in arcs.

References

Bonnichsen, B., W. P. Leeman, et al. (2008). "Miocene silicic volcanism in southwestern Idaho: geochronology, geochemistry, and evolution of the central Snake River Plain." Bulletin of Volcanology 70(3): 315-342.

Camp, V. E. (1995). "Mid-Miocene propagation of the Yellowstone mantle plume head beneath the Columbia River Basalt source region." Geology 23(5): 435-438.

Camp, V. E. and M. E. Ross (2004). "Mantle dynamics and genesis of mafic magmatism in the intermontane Pacific Northwest." Journal of Geophysical Research-Solid Earth 109(B8).

Carlson, R. W. (1984). "Isotopic Constraints on Columbia River Flood-Basalt Genesis and the Nature of the Subcontinental Mantle." Geochimica Et Cosmochimica Acta 48(11): 2357-2372.

Chen, Y. and Y. Zhang (2008). "Olivine dissolution in basaltic melt." Geochimica et Cosmochimica Acta 72(19): 4756-4777.

Christiansen, R. L. 2001, "The Quaternary and Pliocene Yellowstone Plateau volcanic field of Wyoming, Idaho, and Montana."

Christiansen, R. L., G. R. Foulger, et al. (2002). "Upper-mantle origin of the Yellowstone hotspot." Geological Society of America Bulletin 114(10): 1245-1256.

Churikova, T., G. Worner, et al. (2007). "Volatile (S, Cl and F) and fluid mobile trace element compositions in melt inclusions: implications for variable fluid sources across the Kamchatka arc." Contributions to Mineralogy and Petrology 154(2): 217-239.

Craig, H. (1993). "Yellowston hotspot; a continetal mantle plume." Eos, Transactions, American Geophysical Union 74: 602.

Craig, H., J. E. Lupton, et al. (1978). "Helium Isotope Ratios in Yellowstone Park and Lassen Park Volcanic Gases." Geophysical Research Letters 5(11): 897-900.

Danyushevsky, L. V., A. W. McNeill, et al. (2002). "Experimental and petrological studies of melt inclusions in phenocrysts from mantle-derived magmas: an overview of techniques, advantages and complications." Chemical Geology 183(1-4): 5-24.

Demouchy, S. and S. Mackwell (2003). "Water diffusion in synthetic iron-free forsterite." Physics and Chemistry of Minerals 30(8): 486-494.

Dixon, J. E., E. M. Stolper, et al. (1995). "An experimental study of water and carbon dioxide solubilities in mid ocean ridge basaltic liquids .1. Calibration and solubility models." Journal of Petrology 36(6): 1607-1631.

Dodson, A., B. M. Kennedy, et al. (1997). "Helium and neon isotopes in the Imnaha Basalt, Columbia River Basalt Group; evidence for a Yellowstone plume source." Earth and Planetary Science Letters 150(3-4): 443-451.

Feeley, T. C. (2003). "Origin and tectonic implications of across-strike geochemical variations in the Eocene Absaroka volcanic province, United States." Journal of Geology 111(3): 329-346.

Foley, S. (1992). "Vein-Plus-Wall-Rock Melting Mechanisms in the Lithosphere and the Origin of Potassic Alkaline Magmas." Lithos 28(3-6): 435-453.

Geist, D. and M. Richards (1993). "Origin of the Columbia Plateau and Snake River plain; deflection of the Yellowstone plume." Geology 21(9): 789-792.

Graham, D. W., Reid, M. R., Jordan, B. T., Grunder, A. L., Leeman, W. P., Lupton, J. E. (2009). "Mantle Source Provinces Beneath the Northwestern USA Delimited by Helium Isotopes in Young Basalts." Journal of Volcanology and Geothermal Research 188(1-3): 128-140.

Harry, D. L. and W. P. Leeman (1995). "Partial Melting of Melt Metasomatized Subcontinental Mantle and the Magma Source Potential of the Lower Lithosphere." Journal of Geophysical Research-Solid Earth 100(B6): 10255-10269.

Hart, W. K. (1985). "Chemical and Isotopic Evidence for Mixing between Depleted and Enriched Mantle, Northwestern USA." Geochimica Et Cosmochimica Acta 49(1): 131-144.

Hauri, E. (2002). "SIMS analysis of volatiles in silicate glasses, 2: isotopes and abundances in Hawaiian melt inclusions." Chemical Geology 183(1-4): 115-141.

Hofmann, A. W., K. P. Jochum, et al. (1986). "Nb and Pb in Oceanic Basalts - New Constraints on Mantle Evolution." Earth and Planetary Science Letters 79(1-2): 33-45.

Hofmann, A. W. and E. Welin (1988). "Chemical differentiation of the Earth; the relationship between mantle, continental crust, and oceanic crust." Earth and Planetary Science Letters 90(3): 297-314.

Hui, H. J., Y. X. Zhang, et al. (2008). "Pressure dependence of the speciation of dissolved water in rhyolitic melts." Geochimica Et Cosmochimica Acta 72(13): 3229-3240.

Johnson D.M., H. P. R., and Conrey, R.M. (1999). "GeoAnalytical Lab, Washington State University." Advances in X-ray Analysis vol 41: 843-867.

Johnson, E. R., P. J. Wallace, et al. (2008). "Magmatic volatile contents and degassing-induced crystallization at Volcan Jorullo, Mexico: Implications for melt evolution and the plumbing systems of monogenetic volcanoes." Earth and Planetary Science Letters 269(3-4): 477-486.

Jordan, B. T., A. L. Grunder, et al. (2004). "Geochronology of age-progressive volcanism of the Oregon High Lava Plains: Implications for the plume interpretation of Yellowstone." Journal of Geophysical Research-Solid Earth 109(B10).

Kamenetsky, V. S. and A. A. Gurenko (2007). "Cryptic crustal contamination of MORB primitive melts recorded in olivine-hosted glass and mineral inclusions." Contributions to Mineralogy and Petrology 153(4): 465-481.

Kent, A. J. R., E. M. Stolper, et al. (2004). "Mantle heterogeneity during the formation of the North Atlantic Igneous Province: Constraints from trace element and Sr-Nd-Os-O isotope systematics of Baffin Island picrites." Geochemistry Geophysics Geosystems 5.

Knaack, C., Cornelius, S., Hooper, P.R. (1994). "Trace Element Analysis of Rocks and Minerals by ICP-MS." Open File Report, Department of Geology, Washington State University.

Kovalenko, V. I., V. B. Naumov, et al. (2007). "Volatiles in basaltic magmas of ocean islands and their mantle sources: I. Melt compositions deduced from melt inclusions and glasses in the rocks." Geochemistry International 45(2): 105-122.

Kress, V. C. and M. S. Ghiorso (1995). "Multicomponent diffusion in basaltic melts." Geochimica et Cosmochimica Acta 59(2): 313-324.

Le Voyer, M. (2008). "Two contrasting volatile element compositions in primary melt inclusions from Mount Shasta." Eos 89(53, Suppl.): V31B-2132.

Leeman, W. P., Schutt, D.L., Hughes, S.S. (2009). "Thermal structure beneath the Snake River Plain: Implications for the Yellowstone hot spot." Journal of Volcanology and Geothermal Research 188(1-3): 128-140.

Leeman, W. P., C. Annen, et al. (2008). "Snake River plain-Yellowstone silicic volcanism; implications for magma genesis and magma fluxes." Geological Society Special Publications 304: 235-259.

Leeman, W. P. (1982). "Development of the Snake River plain-Yellowstone Plateau Province, Idaho and Wyoming; an overview and petrologic model." Bulletin - Idaho Bureau of Mines and Geology 26: 155-177.

Leeman, W. P. and C. J. Vitaliano (1976). "Petrology of McKinney Basalt, Snake River Plain, Idaho." Geological Society of America Bulletin 87(12): 1777-1792.

Luhr, J. F. (2001). "Glass inclusions and melt volatile contents at Paricutin Volcano, Mexico." Contributions to Mineralogy and Petrology 142(3): 261-283.

Manea, V. C., Manea M., Leeman, W.P., Schutt, D.L. (2009). "The influence of plume head-lithosphere interaction on magmatism associated with the Yellowstone

hotspot track." Journal of Volcanology and Geothermal Research 188(1-3): 68-85.

McCurry, M., Rogers, D. W. (2009). "Mass transfer along the Yellowstone hotspot track I: Petrologic constraints on the volume of mantle-derived magma." Journal of Volcanology and Geothermal Research 188(1-3): 86-98.

McKenzie, D. and R. K. Onions (1991). "Partial Melt Distributions from Inversion of Rare-Earth Element Concentrations." Journal of Petrology 32(5): 1021-1091.

Metrich, N. and P. J. Wallace (2008). Volatile Abundances in Basaltic Magmas and Their Degassing Paths Tracked by Melt Inclusions. Minerals, Inclusions and Volcanic Processes. K. D. Putirka and F. J. Tepley. 69: 363-402.

Michael, P. (1995). "Regionally Distinctive Sources of Depleted Morb - Evidence from Trace-Elements and H2o." Earth and Planetary Science Letters 131(3-4): 301-320.

Moore, G., T. Vennemann, et al. (1998). "An empirical model for the solubility of H2O in magmas to 3 kilobars." American Mineralogist 83(1-2): 36-42.

Moune, S., O. Sigmarsson, et al. (2007). "Recent volatile evolution in the magmatic system of Hekla volcano, Iceland." Earth and Planetary Science Letters 255(3-4): 373-389.

Nash, B. P., M. E. Perkins, et al. (2006). "The Yellowstone hotspot in space and time: Nd and Hf isotopes in silicic magmas." Earth and Planetary Science Letters 247(1-2): 143-156.

Pierce, K. L. and L. A. Morgan (1992). "The track of the Yellowstone hot spot; volcanism, faulting, and uplift." Memoir - Geological Society of America 179: 1-53.

Portnyagin, M., R. Almeev, et al. (2008). "Experimental evidence for rapid water exchange between melt inclusions in olivine and host magma." Earth and Planetary Science Letters 272(3-4): 541-552.

Portnyagin, M., K. Hoernle, et al. (2007). "Constraints on mantle melting and composition and nature of slab components in volcanic arcs from volatiles (H2O, S, Cl, F) and trace elements in melt inclusions from the Kamchatka Arc." Earth and Planetary Science Letters 255(1-2): 53-69.

Ross, M. E. (1983). "Chemical and Mineralogic Variations within Four Dikes of the Columbia River Basalt Group, Southeastern Columbia Plateau." Geological Society of America Bulletin 94(9): 1117-1126.

Sadofsky, S. J., M. Portnyagin, et al. (2008). "Subduction cycling of volatiles and trace elements through the Central American volcanic arc: evidence from melt inclusions." Contributions to Mineralogy and Petrology 155(4): 433-456.

Schiano, P., R. Clocchiatti, et al. (2004). "The nature of melt inclusions inside minerals in an ultramafic cumulate from Adak volcanic center, aleutian arc: implications for the origin of high-Al basalts." Chemical Geology 203(1-2): 169-179.

Severs, M. J., T. Azbej, et al. (2007). "Experimental determination of H2O loss from melt inclusions during laboratory heating: Evidence from Raman spectroscopy." Chemical Geology 237(3-4): 358-371.

Shervais, J. W., S. K. Vetter, et al. (2006). "Layered mafic sill complex beneath the eastern Snake River Plain: Evidence from cyclic geochemical variations in basalt." Geology 34(5): 365-368.

Sobolev, A. V. and L. V. Danyushevsky (1994). "Petrology and Geochemistry of Boninites from the North Termination of the Tonga Trench - Constraints on the Generation Conditions of Primary High-Ca Boninite Magmas." Journal of Petrology 35(5): 1183-1211.

Toplis, M. J. (2005). "The thermodynamics of iron and magnesium partitioning between olivine and liquid: criteria for assessing and predicting equilibrium in natural and experimental systems." Contributions to Mineralogy and Petrology 149(1): 22-39.

Vigouroux, N., P. J. Wallace, et al. (2008). "Volatiles in high-K magmas from the western Trans-Mexican volcanic belt: Evidence for fluid fluxing and extreme enrichment of the mantle wedge by subduction processes." Journal of Petrology 49(9): 1589-1618.

Walker, J. A., K. Roggensack, et al. (2003). "The water and trace element contents of melt inclusions across an active subduction zone." Contributions to Mineralogy and Petrology 146(1): 62-77.

Wallace, P., E. Johnson, et al. (2007). Ascent, degassing, crystallization and eruption of H2O-rich mafic arc magma: A melt inclusion perspective. 17th Annual V M Goldschmidt Conference, Cologne, GERMANY.

Wallace, P. J. (2005). "Volatiles in subduction zone magmas: concentrations and fluxes based on melt inclusion and volcanic gas data." Journal of Volcanology and Geothermal Research 140(1-3): 217-240.

Weaver, B. L. (1991). "The Origin of Ocean Island Basalt End-Member Compositions - Trace-Element and Isotopic Constraints." Earth and Planetary Science Letters 104(2-4): 381-397.

White, W. M. (1985). "Sources of Oceanic Basalts - Radiogenic Isotopic Evidence." Geology 13(2): 115-118.

White, W. M. and A. W. Hofmann (1982). "Sr and Nd Isotope Geochemistry of Oceanic Basalts and Mantle Evolution." Nature 296(5860): 821-825.

Yuan, H. Y. and K. Dueker (2005). "Teleseismic P-wave tomogram of the Yellowstone plume." Geophysical Research Letters 32(7).

Zhang, Y. X. and E. M. Stolper (1991). "Water Diffusion in a Basaltic Melt." Nature 351(6324): 306-309.

Zhang, Y. X., D. Walker, et al. (1989). "Diffusive Crystal Dissolution." Contributions to Mineralogy and Petrology 102(4): 492-513.

TABLE 2.1. Samples Analyzed

Sample #	Syn-Caldera GTMF-2	GTMF-4	IP-5	AYS	OS	Post-Caldera L05-1	L00-35	SRP-2
age (Ma)	0.2	0.2	<0.6	<0.6	<0.6	<1	1	<1
setting	Gerritt basalt near Mesa Falls	Gerritt basalt near Mesa Falls	Spencer-Kilgore Lava Field	Osprey Basalt AYS-29-05 in Christianson 2001	Osprey Basalt 9YC-514 in Christianson 2001	Late SRP basalt	Late SRP basalt	McKinney Basalt, late SRP basalt
SiO_2	48.26	48.41	48.12	52.88	50.35	2.21	2.39	2.96
TiO_2	1.58	1.57	1.20	1.94	1.59	16.22	15.55	14.85
Al_2O_3	15.65	16.28	14.63	14.81	15.34	11.21	11.94	13.37
FeO	10.58	10.37	11.60	11.89	11.67	0.18	0.19	0.20
MnO	0.18	0.18	0.18	0.17	0.16	7.59	7.31	7.64
MgO	9.44	8.68	10.59	5.83	8.18	9.92	10.09	9.10
CaO	11.32	11.57	10.90	2.81	10.59	2.84	2.59	2.64
Na_2O	2.34	2.36	2.13	9.69	2.55	0.66	0.80	0.72
K_2O	0.45	0.42	0.36	0.79	0.54	0.28	0.22	0.18
P_2O_5	0.20	0.15	0.28	0.24	0.19			
Rb	8.10	7.20	6.70			12.80	16.40	14.00
Sr	215.00	218.00	174.00			334.00	331.00	311.00
Y	21.63	19.27	23.40			22.25	21.01	23.48
Zr	125.00	123.00	109.00			202.00	172.00	226.00
Nb	12.61	12.28	10.10			19.42	15.33	18.63
Ba	229.00	227.00	186.00			386.00	396.00	368.00
La	10.73	9.26	11.30			13.67	11.88	12.93
Ce	23.26	19.94	22.40			29.17	25.57	27.50
Pr	3.09	2.69	2.88			3.84	3.45	3.64
Nd	13.62	11.81	12.80			16.74	15.18	15.97
Sm	3.50	3.13	3.52			4.10	3.89	4.11
Eu	1.37	1.31	1.26			1.76	1.79	1.96
Gd	3.96	3.52	3.74			4.38	4.15	4.46
Dy	4.26	3.92	4.34			4.50	4.31	4.79
Er	2.41	2.20	2.63			2.49	2.49	2.66
Yb			2.25					
Th	0.66	0.62	0.72			1.26	1.50	1.77
U	0.18	0.16	0.23			0.38	0.34	0.50

Host rock sample numbers with descriptions and major and trace element chemistry

TABLE 2.2. Melt inclusion major oxides, trace elements and volatiles.

syn-caldera	AYS-1	AYS-2	AYS-4	AYS-5	AYS-6	AYS-7	AYS-8	AYS-9	GTMF-2-2	GTMF-2-3	GTMF-2-4	GTMF-2-5
SiO_2	47.89	48.68	40.61	48.62	48.26	49.05	48.89	48.74	48.43	48.78	49.04	47.63
TiO_2	1.06	1.32	1.19	1.45	1.32	1.20	1.05	1.28	1.82	1.76	2.58	1.64
Al_2O_3	14.07	16.74	15.33	16.99	16.74	16.30	14.52	17.77	16.68	18.66	13.58	17.82
FeO	10.73	9.84	11.74	9.73	10.52	9.98	12.40	8.89	9.09	7.12	10.17	9.08
MnO	0.19	0.22	0.20	0.22	0.25	0.19	0.22	0.19	0.21	0.12	0.20	0.14
MgO	11.60	6.78	8.28	6.37	6.80	6.63	8.64	6.25	6.62	5.33	7.39	6.78
CaO	11.34	12.76	12.41	13.20	13.03	12.98	11.65	12.92	12.76	14.11	11.95	12.71
Na_2O	2.13	2.68	8.46	2.64	2.37	2.67	1.76	2.84	2.73	2.66	2.82	2.26
K_2O	0.18	0.18	0.44	0.16	0.16	0.20	0.12	0.17	0.63	0.41	0.63	0.46
P_2O_5	0.11	0.17	0.11	0.02	0.18	0.14	0.09	0.18	0.30	0.38	0.58	0.33
H_2O	0.71	0.62	1.24	0.61	0.38	0.67	0.66	0.75	0.72	0.67	1.06	1.15
olivine Fo		83.97	83.66	84.15	83.80	83.67	84.11	83.85		85.53		
CO_2												
F	106.05	149.73	94.41		92.22							
S	881.15	915.40	1606.31		625.91							
Cl	55.74	22.19	405.00		22.15							
Sc		47.63	31.91	34.78	43.20	32.75	43.03	33.59	34.50	33.87	46.03	25.31
Rb		1.87	3.22	1.70	1.80	1.50	1.53	1.48	12.30	10.49	14.89	8.46
Sr		191.93	155.48	214.53	197.13	224.71	188.31	211.72	243.24	248.34	208.48	210.98
Y		18.22	27.14	19.08	16.92	18.22	17.42	18.15	27.25	25.14	37.50	23.85
Zr		62.91	67.80	63.92	64.80	59.68	58.10	54.98	135.45	115.40	199.10	137.33
Nb		3.82	3.97	4.25	3.30	3.89	3.53	3.61	15.36	13.28	21.83	15.34
Ba		127.88	2238.16	138.88	128.27	139.52	134.05	142.93	341.39	235.15	407.69	225.51
La		4.37	12.94	5.17	4.00	5.00	4.31	5.02	16.29	11.88	22.03	12.88
Ce		12.79	11.42	13.93	12.66	14.59	13.11	14.04	41.85	36.70	55.43	35.53
Pr		1.57	3.95	1.87	1.70	1.61	1.56	2.03	4.93	4.03	6.64	4.49
Nd		8.59	16.46	9.23	6.82	9.55	8.86	8.97	21.61	17.66	25.85	17.73
Sm		2.11	4.85	3.09	2.15	2.51	1.77	2.68	4.78	5.38	5.48	4.93
Eu		0.86	0.85	1.09	1.36	1.24	1.01	1.04	1.41	1.62	2.15	1.38
Gd		2.16	5.80	2.99	3.17	3.14	2.04	4.08	4.14	3.43	7.21	4.55
Dy		4.55	5.61	2.75	3.66	2.74	4.46	3.31	4.71	5.04	6.53	3.59
Er		1.75	4.12	2.29	2.13	2.53	1.79	1.83	2.89	2.68	3.96	2.24
Yb		1.46	3.83	1.88	2.24	1.64	1.64	1.19	3.14	1.91	4.87	1.97
Th			0.87	0.19					0.50	0.20	0.76	0.44
U			0.10						0.30		0.34	0.15

Major element, trace element and volatile concentrations. Major oxides and H_2O are given in wt%, trace elements and other volatiles in ppm

TABLE 2.2 cont.

syn-caldera	GTMF-2-6	GTMF-2-7	GTMF-2-9	GTMF-2-10	GTMF-2-11	GTMF-2-12	GTMF-2-13	GTMF-4-3	GTMF-4-6	GTMF-4-7	GTMF-4-8	GTMF-4-20
SiO_2	44.47	47.79	47.48	46.06	46.43	44.81	45.16	39.42	48.79	46.98	49.24	40.55
TiO_2	1.82	1.65	1.81	1.57	1.50	0.98	1.85	2.70	1.87	1.72	1.75	1.60
Al_2O_3	14.47	18.95	16.97	16.68	16.89	11.67	17.00	12.63	17.22	16.69	16.27	14.75
FeO	12.47	6.76	9.53	10.26	9.97	18.30	10.58	14.82	8.29	9.76	9.61	15.48
MnO	0.23	0.18	0.14	0.15	0.18	0.29	0.10	0.27	0.22	0.21	0.13	0.22
MgO	8.92	4.62	6.90	7.09	6.82	12.85	7.13	11.77	5.93	6.65	7.37	10.08
CaO	11.53	14.26	12.65	12.66	12.71	4.63	13.48	14.74	13.20	12.55	12.14	11.66
Na_2O	4.09	4.31	2.75	3.34	3.84	4.84	2.56	1.82	2.71	1.92	2.24	1.55
K_2O	0.63	0.42	0.56	0.51	0.43	0.72	0.44	0.34	0.41	0.45	0.40	0.43
P_2O_5	0.34	0.40	0.50	0.25	0.33	0.33	0.25	0.38	0.32	0.37	0.31	0.37
H_2O	1.03	0.64	0.70	1.41	0.89	0.58	1.46	1.11	1.03	2.70	0.54	3.30
olivine Fo	84.67											
CO_2												
F				500.93		689.12				489.56		459.47
S				1711.50		423.40				2297.45		897.75
Cl				227.59		128.49				250.99		1099.52
Sc	25.53			31.99			40.22			33.54	65.78	
Rb	7.22			8.03			7.21			7.10	7.96	
Sr	1310.69			198.05			168.77			366.57	230.18	
Y	22.64			23.28			24.79			29.98	28.25	
Zr	128.58			158.24			152.60			177.39	136.64	
Nb	17.99			18.20			15.06			18.73	13.47	
Ba	5452.00			610.26			257.08			3756.73	238.87	
La	8.99			8.94			10.64			17.34	14.97	
Ce	22.70			27.84			28.77			36.66	33.62	
Pr	3.00			3.22			3.67			4.84	3.68	
Nd	13.00			16.28			15.70			20.99	20.48	
Sm	3.42			4.19			4.44			4.59	5.23	
Eu	1.52			1.54			1.19			1.90	1.52	
Gd	4.30			6.01			4.75			6.78	4.93	
Dy	4.13			4.04			3.54			6.47	3.97	
Er	2.42			2.89			2.92			3.55	2.71	
Yb	2.59			2.59			2.05			2.52	1.46	
Th	0.38			0.50			0.48			0.45	0.78	
U	0.29			0.21			0.20			0.28		

Major element, trace element and volatile concentrations. Major oxides and H_2O are given in wt%, trace elements and other volatiles in ppm

TABLE 2.2 cont.

syn-caldera	GTMF-4-21	GTMF4 a	GTMF4 b	GTMF4 c	GTMF4 d	IP-5-1	IP-5-3	IP-5-4	IP-5-5	IP-5-6	IP-5-7	IP-5-8
SiO_2	44.10					45.50	48.68	49.56	45.77	46.81	46.15	46.65
TiO_2	2.21					2.11	1.38	1.50	1.35	1.48	0.89	1.37
Al_2O_3	16.44					10.60	18.40	21.06	17.18	16.67	17.33	17.68
FeO	11.69					12.78	8.00	5.60	11.13	9.88	8.10	7.97
MnO	0.21					0.28	0.10	0.18	0.18	0.17	0.17	0.15
MgO	8.76					11.04	6.57	4.35	9.71	8.54	6.72	6.88
CaO	12.79					11.03	13.06	13.14	12.20	12.74	13.83	13.29
Na_2O	1.06					4.81	2.48	3.26	1.71	2.11	5.05	4.18
K_2O	0.34					0.78	0.24	0.35	0.23	0.30	0.23	0.32
P_2O_5	0.30					0.32	0.29	0.06	0.21	0.38	0.12	0.11
H_2O	2.11	0.43	2.56	2.09	1.14	0.75	0.81	0.96	0.34	0.93	1.41	1.39
olivine Fo	84.91					86.87	86.90	87.33	86.78	86.67	86.39	
CO_2		49.7	1677	1559	248							
F		383	341	357	327			0.00				
S		700	1546	1841	1886			10.40				
Cl		66.3	284.0	185.0	134.0			41.82				
Sc						57.68	28.02			29.47	30.28	32.89
Rb						9.86	4.65			5.61	1.58	4.84
Sr						139.86	217.05			182.48	122.28	194.47
Y						43.00	19.41			22.26	18.41	23.72
Zr						209.19	82.05			90.21	50.23	99.54
Nb						15.45	9.00			8.76	3.78	9.55
Ba						308.95	180.13			211.00	165.13	208.39
La						21.33	8.68			8.23	4.30	9.73
Ce						44.03	24.85			25.64	11.15	26.45
Pr						5.61	3.01			3.16	1.52	3.37
Nd						28.30	13.02			13.03	7.17	15.17
Sm						6.28	3.84			4.08	1.87	3.99
Eu						2.01	1.10			1.37	0.87	1.35
Gd						6.93	2.18			3.53	2.39	4.44
Dy						7.60	3.63			3.74	2.87	4.45
Er						4.44	2.26			2.20	2.88	3.30
Yb						4.05	2.43			2.41	2.01	2.33
Th						1.52	0.25			0.23	0.19	0.26
U						0.46	0.06			0.15		0.13

Major element, trace element and volatile concentrations. Major oxides and H_2O are given in wt%, trace elements and other volatiles in ppm

TABLE 2.2 cont.

syn-caldera	IP-5-9	IP-5-10	IP-5-12	IP-5-13	OS-1	OS-2	OS-3	OS-5	OS-10	OS-11	OS-12	OS-13
SiO_2	49.26	48.54	48.94	48.41	50.59	47.74	39.80	49.66	49.29	47.25	49.30	47.85
TiO_2	1.44	1.35	1.35	1.43	1.78	1.29	2.10	1.15	1.31	1.17	1.29	1.08
Al_2O_3	19.83	19.06	18.70	18.46	15.56	15.79	14.95	17.63	17.94	18.91	18.00	15.35
FeO	6.30	7.35	7.54	6.22	10.90	11.38	16.78	9.06	8.51	8.68	8.88	10.31
MnO	0.12	0.16	0.14	0.17	0.10	0.21	0.28	0.17	0.10	0.16	0.16	0.21
MgO	5.14	5.50	6.69	4.44	5.23	7.11	7.68	5.94	5.77	5.50	5.84	11.15
CaO	13.56	13.81	13.05	12.11	11.01	13.17	9.35	12.53	13.04	12.75	12.98	11.20
Na_2O	2.54	2.43	2.54	6.75	3.61	2.36	8.19	2.99	2.96	2.69	2.65	2.17
K_2O	0.35	0.27	0.26	0.51	0.47	0.26	0.09	0.29	0.19	0.30	0.19	0.14
P_2O_5	0.19	0.36	0.08	0.19	0.28	0.06	0.25	0.05	0.22	0.19	0.17	0.13
H_2O	1.27	1.17	0.72	1.31	0.47	0.63	0.53	0.54	0.66	2.39	0.54	0.42
olivine Fo	87.43	86.19	87.06	86.25	79.17	83.39	83.78	83.84	84.29		84.03	
CO_2												
F			37.97	527.31		186.39				163.90		
S			441.22	1073.20		799.55				792.89		
Cl			38.50	303.72		27.72				84.80		
Sc	29.85		56.85	35.11		113.30		35.33			31.98	32.19
Rb	6.59		5.21	5.66		7.13		6.17			1.28	1.37
Sr	223.05		193.87	201.64		171.27		216.91			224.84	190.63
Y	20.18		24.24	21.63		22.81		20.28			17.21	16.28
Zr	80.81		106.05	107.58		81.58		65.01			59.01	52.25
Nb	8.74		7.76	8.77		3.45		5.36			3.70	3.26
Ba	202.85		158.18	221.56		190.01		177.07			149.88	128.19
La	8.84		8.99	11.04		5.53		6.49			4.65	3.54
Ce	26.21		21.99	25.75		14.40		17.14			13.94	11.29
Pr	3.05		2.75	2.86		1.42		1.89			1.58	1.48
Nd	12.09		15.10	14.29		6.53		8.66			8.85	7.04
Sm	3.23		4.44	3.36				2.94			1.85	2.21
Eu	1.66		1.27	1.14		1.48		1.19			1.43	1.26
Gd	4.31		4.75	3.40				3.41			2.60	3.53
Dy	4.07		2.66	3.71		3.65		3.66			3.08	2.93
Er	2.44		2.71	2.24				1.72			1.52	1.29
Yb	2.41		4.04	2.31				1.55			1.47	1.57
Th	0.24			0.67				0.90				
U	0.13			0.22				0.23				

Major element, trace element and volatile concentrations. Major oxides and H_2O are given in wt%, trace elements and other volatiles in ppm

TABLE 2.2 cont.

post-caldera	L00-35-3	L00-35-4	L00-35-6	L00-35-8	L00-35-9	L00-35-10	L00-35-11	L00-35-11b	L00-35-13	l05-1-2	L05-1-3	L05-1-4
SiO_2	49.58	43.87	48.63	45.41	49.26	49.97	49.87	49.81	49.09	48.60	49.42	48.39
TiO_2	2.84	4.68	1.11	2.01	3.15	3.14	2.99	2.95	3.00	2.66	2.59	2.66
Al_2O_3	15.67	13.72	12.50	13.03	16.45	16.83	19.11	16.59	14.67	17.52	19.37	17.22
FeO	10.05	16.11	16.80	16.45	9.75	8.31	6.70	8.96	10.89	8.94	7.55	8.97
MnO	0.26	0.28	0.42	0.29	0.20	0.14	0.16	0.25	0.23	0.17	0.18	0.11
MgO	4.52	7.97	8.23	7.89	4.15	3.18	2.78	3.74	4.91	4.96	3.18	4.86
CaO	12.19	8.88	5.33	8.81	11.62	12.98	12.95	12.33	12.26	12.21	12.51	12.49
Na_2O	2.92	2.29	4.95	4.33	3.10	3.18	3.43	3.10	2.89	3.43	3.63	3.12
K_2O	0.98	0.71	1.11	0.31	1.06	1.04	0.82	1.00	0.90	0.78	0.69	0.77
P_2O_5	0.71	0.89	0.84	0.47	0.59	0.63	0.59	0.66	0.59	0.73	0.60	0.84
H_2O	0.29	0.60	0.08	1.01	0.67	0.59	0.60	0.61	0.57	0.00	0.27	0.57
olivine Fo	78.03	79.27			78.04	78.01	78.60				79.77	
CO_2												
F		489.39			63.98						884.31	
S		103.48	2.55		201.08		1.35				1048.34	
Cl		614.26	7.06		18.75		3.87				143.48	
Sc	32.70	42.90		75.80	29.92	31.17					30.38	
Rb	24.39	11.59		4.72	22.19	25.06					13.44	
Sr	386.82	319.17		269.21	359.77	402.31					438.57	
Y	36.19	44.40		31.09	31.68	37.34					40.00	
Zr	221.03	183.29		166.53	209.35	229.37					259.16	
Nb	22.54	24.79		16.21	20.00	24.29					25.23	
Ba	590.24	480.29		374.69	539.20	607.48					515.92	
La	25.65	30.75		23.79	24.21	26.05					28.09	
Ce	70.71	77.53		65.37	65.76	75.46					71.28	
Pr	7.86	9.81		4.82	7.87	8.54					7.91	
Nd	36.17	44.05		18.58	31.97	38.38					38.68	
Sm	8.01	10.61		5.63	5.29	8.47					8.96	
Eu	2.16	2.90		1.96	2.68	2.98					2.93	
Gd	7.71	8.74		4.21	7.32	6.42					7.37	
Dy	7.16	8.35		5.75	5.47	5.44					5.71	
Er	2.87	4.91		3.43	3.44	3.49					4.44	
Yb	2.71	4.50		1.15	1.99	3.23					2.92	
Th	1.95	1.61		1.49	2.23	1.76					1.23	
U	0.41	0.25		0.63	0.60	0.42					0.44	

Major element, trace element and volatile concentrations. Major oxides and H_2O are given in wt%, trace elements and other volatiles in ppm

TABLE 2.2 cont.

post-caldera	L05-1-5	L05-1-6	L05-1-7	l05-1-8	l05-1-10	L05-1-12	L05-1-13	SRP-2-1	SRP-2-3	SRP-2-4	SRP-2-5	SRP-2-6
SiO_2	48.47	49.90	47.89	53.80	50.42	50.75	53.53	45.70	45.78	50.67	49.93	49.12
TiO_2	2.47	2.70	2.65	2.17	4.12	2.69	2.01	3.69	3.64	3.64	4.08	4.37
Al_2O_3	17.59	19.17	12.78	15.94	14.25	20.25	18.48	14.57	14.70	15.29	14.87	14.62
FeO	9.45	6.96	17.43	8.37	7.95	5.41	5.60	15.69	15.35	10.84	10.99	12.29
MnO	0.15	0.12	0.29	0.15	0.17	0.10	0.12	0.25	0.17	0.13	0.22	0.17
MgO	4.83	2.86	5.02	4.12	4.32	2.54	3.09	5.36	5.35	3.38	3.29	3.75
CaO	12.12	12.85	6.54	10.34	11.74	11.99	10.51	9.98	10.29	10.30	11.36	10.91
Na_2O	2.93	3.47	3.62	3.17	3.63	3.82	3.81	2.84	3.04	3.18	3.14	2.97
K_2O	0.71	0.83	1.54	1.00	1.43	0.86	1.74	0.94	0.91	1.20	1.05	0.98
P_2O_5	0.51	0.65	1.07	0.62	1.32	0.85	0.50	0.73	0.52	0.93	0.75	0.50
H_2O	0.78	0.48	1.15	0.33	0.65	0.74	0.63	0.25	0.27	0.42	0.32	0.32
olivine Fo		77.74	69.34	81.11	81.61		82.16	73.23				
CO_2												
F			1459.74					1032.33				
S			482.11					1209.87				
Cl			375.75					87.92				
Sc		27.09	22.78			25.24	21.79	36.94	32.31	33.67	34.54	36.30
Rb		15.84	28.84			14.36	49.57	21.29	22.91	29.87	24.13	22.83
Sr		449.70	275.09			436.17	475.79	328.67	343.80	346.20	379.23	352.64
Y		34.52	43.80			32.22	29.63	39.18	46.05	45.50	49.29	51.81
Zr		242.98	347.41			238.03	199.72	285.00	291.29	341.15	337.22	330.77
Nb		27.28	32.15			25.70	28.88	27.61	27.91	32.31	31.29	28.89
Ba		538.02	684.26			526.55	681.85	546.33	552.79	620.55	598.16	566.58
La		27.15	35.87			27.22	39.52	30.67	31.07	35.15	33.71	32.68
Ce		78.01	92.63			75.83	100.15	76.86	83.29	86.59	87.18	84.14
Pr		9.26	10.46			7.96	10.38	9.42	10.21	10.63	11.39	10.87
Nd		36.85	41.02			36.31	39.68	42.03	39.50	44.90	47.65	43.18
Sm		8.04	9.20			6.94	7.20	7.03	8.94	10.61	12.05	9.51
Eu		3.27	3.10			2.98	2.16	2.92	3.50	3.68	4.09	3.70
Gd		6.11	8.00			6.59	6.90	9.28	8.40	9.20	11.08	10.20
Dy		8.21	7.47			7.72	7.30	7.76	7.38	9.59	9.02	9.38
Er		3.09	4.30			3.49	3.23	4.47	4.17	4.88	5.03	5.49
Yb		3.67	4.54			2.42	2.82	3.93	3.88	3.92	5.72	3.45
Th		0.71	2.53			0.93	6.05	2.25	2.70	3.53	2.02	2.66
U		0.50	0.78			0.46	1.27	0.84	0.80	1.09	0.92	1.00

Major element, trace element and volatile concentrations. Major oxides and H_2O are given in wt%, trace elements and other volatiles in ppm

TABLE 2.2 cont.

post-caldera	SRP-2-7	SRP-2-8	SRP-2-9	SRP-2-10	SRP-2-11	SRP-2-13	SRP-2-14	srp-2-16	SRP-2-17
SiO_2	49.46	50.45	48.11	45.77	44.22	45.94	46.65	49.74	49.00
TiO_2	3.98	3.00	3.76	3.65	3.58	3.61	3.53	3.74	4.25
Al_2O_3	14.31	17.21	14.61	14.60	13.63	13.99	14.76	15.00	15.05
FeO	12.51	9.43	12.87	15.53	18.13	15.97	15.21	11.52	11.63
MnO	0.25	0.23	0.21	0.17	0.22	0.20	0.30	0.16	0.29
MgO	4.31	2.46	4.40	5.73	6.61	5.30	5.40	3.64	3.23
CaO	10.29	11.66	10.80	9.59	8.80	9.53	9.21	10.79	11.12
Na_2O	2.95	2.71	3.18	2.84	2.37	3.05	3.01	2.66	2.87
K_2O	1.02	1.53	0.89	0.81	0.78	0.99	0.95	0.95	1.01
P_2O_5	0.55	0.96	0.93	0.63	0.58	0.78	0.51	0.73	0.78
H_2O	0.37	0.34	0.25	0.69	1.09	0.64	0.46	1.07	0.78
olivine Fo									
CO_2									
F		1437.06			958.82				
S		1069.19			1029.42				
Cl		137.05			86.01				
Sc	34.51	38.57	35.07		27.47	29.86	94.05		42.00
Rb	22.50	25.53	22.89		15.52	24.29	83.24		24.28
Sr	329.97	373.31	339.88		284.60	327.99	360.42		358.75
Y	46.58	50.94	45.50		38.60	41.47	137.75		52.74
Zr	310.63	349.05	331.77		277.26	270.45	1209.37		353.65
Nb	27.52	28.45	27.60		21.63	25.82	99.55		31.46
Ba	540.68	602.35	569.11		431.52	536.60	1708.15		612.88
La	32.68	35.02	33.48		27.12	29.31	89.13		33.84
Ce	81.79	84.51	86.13		62.99	75.78	219.78		90.87
Pr	9.95	11.11	9.77		8.02	9.16	26.25		11.32
Nd	40.73	44.74	44.74		36.69	37.72	107.31		48.56
Sm	9.68	11.94	9.57		7.52	7.71	20.06		10.19
Eu	3.51	3.74	2.97		2.91	3.20	6.36		3.77
Gd	9.42	10.50	10.65		7.12	8.57	25.42		12.68
Dy	7.94	10.72	9.72		8.26	7.48	26.06		8.90
Er	5.41	4.82	4.52		4.20	3.51	13.60		5.26
Yb	4.53	4.03	5.04		3.09	3.91	12.42		5.66
Th	2.25	3.16	2.53		1.91	1.46	9.25		2.81
U	0.81	0.75	0.89		0.62	0.82	2.63		0.98

Major element, trace element and volatile concentrations. Major oxides and H_2O are given in wt%, trace elements and other volatiles in ppm

Chapter 3

Water and Other Volatile Systematics of Olivine-Hosted Melt Inclusions in the Columbia River Flood Basalts and Associated Lavas of the Oregon Plateau

Abstract

Information regarding the volatile budget of magmas and their sources can be obtained through study of olivine-hosted melt inclusions in volcanic rocks. Such inclusions, found in seven basalt samples from the Columbia River Basalt group (CRB) and Oregon Plateau Basalts (OPB) in eastern Oregon and Washington, were analyzed for major element, trace element and volatile (H_2O, S, F, and Cl) compositions. A wide range in H_2O concentrations was discovered, with the highest amount of 4.2 wt% found in olivine grains from a lava flow in the Malheur Gorge area that erupted several million years after the hypothesized initial impingement of the mantle plume against the lithosphere. This H_2O concentration and others in the sample suite are significantly higher than those observed in hotspots such as Hawaii (~0.8-0.9 wt%) or Mid-Ocean Ridge Basalts (MORBs) (~0.2 wt%), and are comparable to those measured for the lavas in the Snake River Plain-Yellowstone volcanic corridor.

Lavas considered to be of plume origin from the Picture Gorge basalts in the main-eruptive-stage-CRB have a maximum water concentration of 2.4 wt %, also

significantly higher than values published previously for any plume-related volcanism. The highest H_2O concentrations were most often found in the least differentiated melt inclusions, indicating that such concentrations are characteristic of the mantle source rather than resulting from the process of differentiation. Low H_2O concentrations in some inclusions that displayed primitive melt compositions indicate post-entrapment degassing in some of the melt inclusions studied. Compositional heterogeneities exhibited both within and between samples suggest either major compositional differences in the mantle source or the development of "edge effects" due to rapid crystallization before melt inclusion entrapment. The enrichment of Ba relative to Th in many of the melt inclusions may indicate that volatiles in the CRB-OPB have a subduction zone origin.

Introduction

The study of olivine-hosted melt inclusions trapped at depth by growing olivine crystals, before a rising magma has the opportunity to degas completely, presents an exceptional opportunity to directly measure pre-eruptive volatile concentrations of basaltic rocks, thereby allowing characterization of the source and melting processes as well (Danyshevsky et al. 2002; Hauri 2002; Wallace 2005). When the trapped melt is isolated from the bulk magma, the compositional features of the magma at that time are preserved, while the residual magma hosting the crystal continues to evolve. However, the inclusion may be modified to some extent due to its interaction with the host olivine. Homogeneous inclusions are quite rare; most often inclusions have

separated into glass ± gas bubbles ± daughter minerals. The obvious exceptions to this are tuffaceous eruptions, where melt inclusions remain glassy due to rapid quenching, thus making direct measurements possible without the need for re-homogenization (e.g., Luhr 2001; Sadofsky et al. 2008). Frequently, however, melt inclusions have undergone some crystallization, thus necessitating re-homogenization at elevated temperature and pressure in a piston cylinder apparatus, prior to making any analyses (Danyushevsky et al. 2002).

H_2O concentrations upwards of 8 wt% have been reported in inclusions within arc magmas (Wallace 2005; Sadofsky et al. 2008; Vigouroux et al. 2008) with correspondingly high saturation pressures, providing considerable evidence that silicate melt inclusions may retain their original volatile content. Measuring H_2O content within the inclusion glass allows estimation of the pre-eruptive volatile concentration of the magma. Olivine is an ideal mineral for volatile studies due to its tendency to crystallize early in most basaltic magmas and can therefore trap melt inclusions before much evolution occurs in the magma. Previous studies have addressed the volatile budgets for arcs (Wallace 2007; Portnyagin et al. 2007; Sadofsky et al. 2008; Vigouroux et al. 2008), oceanic hotspots (Hauri et al. 2002; Moune et al. 2007), and MORBs (Kamenetsky and Gurenko, 2007). Not surprisingly, all indicate that arc lavas are a factor of 5-8 more hydrous than ocean island basalts, and up to 20 times more hydrous than MORBs. However, little data is available for volatiles in continental hotspots.

When interpreting H_2O data from silicate melt inclusions, great care must be taken because of the possibility that a significant amount of diffusion may have occurred either during magma ascent through the crust or during the homogenization process in the laboratory. It is therefore important to interpret melt inclusion volatile data in reference to major oxide and trace element geochemistry so that the effects of these processes can be assessed.

The Columbia River Basalt group and associated Oregon Plateau Basalt group (CRB-OPB) were chosen for examination because they and the associated Snake River Plain (SRP) represent perhaps the best studied continental hotspot track in the world. The Yellowstone hotspot track (consisting of the CRB-OPB and SRP) is currently active at Yellowstone National Park in northwestern Wyoming (Fig. 3.1). The proximity of the CRB-OPB to the plate margin and modification by Basin and Range faulting further complicates its history.

Volcanism began in the CRB-OPB region at ~17 Ma with the eruption of the oldest flows within the Steens Basalts in southeastern Oregon (Brueseke et al. 2007). Volcanism peaked with the eruption of the volumetrically dominant Grande Ronde basalts around the tri-state region of Washington, Oregon and Idaho in the northwestern United States at ~17-16 Ma. It then continued at progressively smaller volumes to the present, totaling ~200,000 km^3 of lavas (Reidel 1983; Mangan et al. 1986; Hooper 2002). The earliest basalts, erupting over a ~1.5 My period, make up the bulk of that volume, and tend to be more evolved than the younger lavas (Hooper et al.

1993). The dominant unit of the CRB volumetrically, Grande Ronde basalt, is basaltic andesite in composition. It is largely aphyric with few phenocrysts. A younger phase of volcanism in the CRB-OPB (~14 Ma to present), termed late-eruptive-stage, has been attributed to decompression melting due to Basin and Range extension (Camp et al. 2003). Basalts of this type from this region are generally more primitive, with higher abundances of olivine and plagioclase phenocrysts. However, late-eruptive-stage volcanism may still sample the same mantle source region that produced the main-stage lavas of the CRB-OPB because of their proximity to the plume basalts.

It is widely accepted that the CRB-OPB lavas represent the initial impingement and sub-crustal flow of the head of the plume whose tail currently resides under the Yellowstone super-volcano (Camp and Ross, 2004). Dodson et al. (1997) found $^{3}He/^{4}He$ ratios up to 11.4 times atmospheric levels in the Imnaha basalt, in southeastern Washington, implicating a plume source for the CRB-OPB. Other isotopic systems, such as Sr, Nd, and Pb, are complicated by lithospheric contamination (Carlson, 1984; Leeman et al., 1992; Ramos et al., 2005) which varies from accreted oceanic lithosphere to the West and cratonic lithosphere to the East (Lund and Snee, 1988; Strayer et al., 1989). Yuan & Dueker (2005) imaged a low velocity anomaly beneath Yellowstone to a depth of 660 km, which has been interpreted as a rising plume elevated in temperature relative to the ambient mantle, further supporting the plume origin of the province.

Interpreting the CRB-OPB volcanism as outpourings from the initial impingement of the Yellowstone plume head onto the lithosphere is complicated by the rather

obvious offset between the main exposures of CRB flood basalt and the initiation point of the Yellowstone hotspot track in the McDermitt Caldera area of southeastern Oregon and north-central Nevada (Geist and Richards, 1993; Camp, 1995). Geist and Richards (1993) suggested that the subduction of the Farallon slab may have caused deflection of the plume head. Alternatively Camp (1995) suggested that flow along the deep keel of the North American craton could explain the offset. Camp and Ross (2004) reconcile the timing and positions of the eruptive centers of the CRB-OPB to the Camp (1995) model. Hales et al. (2005) suggest that the focus of the greatest volumes of lavas in southeastern Washington was controlled by lithospheric de-lamination under the Wallowa Mountains.

Little data on the volatile budget of the CRB-OPB region currently exists. Lange (2002) calculated possible water concentrations of greater than 2 wt% for the main-eruptive-stage-CRB (and up to 4 wt% in late-eruptive-stage basalts), which may have been attained by the plume if it interacted with the Farallon slab. Lange (2002) also notes that the uniform phenocryst development in CRB lava flows can be explained more easily assuming that crystallization is driven by volatile degassing and is not a result of cooling. Ramos et al. (2005) demonstrated Sr isotope disequilibrium in the CRB and used this to argue for short storage times and rapid crystallization, also consistent with shallow-level crystal fractionation. High-H_2O concentrations, therefore, may be expected in the lavas of the CRB-OPB.

Preparation and Homogenization of Olivine-hosted Melt Inclusions

6. Sample Selection and Homogenization

Fifty eight olivine grains (425 μm to 1mm) were separated from seven basalt samples collected from throughout the CRB-OPB and individually inspected under reflected light to identify melt inclusions. From this sample set, all but one resulted in usable olivine grains. Sample GR-1A, a dike from the Chief Joseph Dike Swarm in southeastern Washington and northeastern Oregon (Fig. 3.1), produced few usable olivine grains; therefore melt inclusions in plagioclase were also used. JD-4 was collected from the Monument Dike Swarm (Fig. 3.1), recognized to be the source of the Picture Gorge Basalts. JD-4 and GR-1A represent main-eruptive-stage (~17-15.5 Ma) CRB volcanism. Samples MG-1, MG-4 and MG-6 are basalt flows of variably younger age (12 Ma to recent) from the Malheur Gorge in eastern Oregon and represent late-eruptive-stage volcanism of the OPB. Samples JV-2 and JV-7 were collected from very young (<1 Ma) lava flows in the Jordan Valley in southeastern Oregon, and represent some of the most recent OPB volcanism. The emphasis on late-eruptive-stage basalts was dictated by the availability of unaltered olivine phenocrysts.

Invariably, the melt inclusions were crystallized, thus needing to be re-homogenized in a piston cylinder apparatus at the University of Michigan (see Hui et al. 2008 for calibration). Between 10 and 15 olivine grains were homogenized at once in a single graphite capsule using a barium carbonate pressure medium. The charge was heated to 1300° C at a pressure of approximately 6 kbars in less than 1 minute. Temperature in the charge was maintained for 18-20 minutes, and then, within 20 seconds, quenched to below 200° C. A temperature of 1300° C was used in the re-

homogenization because it is just above the basalt liquidus, which is usually in the range of 1100-1200° C. Rapid melting and quenching minimizes volatile diffusion . Homogenized olivine grains were individually mounted in epoxy under vacuum before polishing with SiC grit sandpaper until inclusions were exposed on both sides. Final thicknesses ranged approximately from 20 to 70 microns.

7. Bulk Rock Analysis

Major oxides, Rb, Sr, and Zr were analyzed by x-ray fluorescence (XRF), and trace elements for bulk host-rocks were measured by LA-ICP-MS at the XRF and ICP-HEX-MS Laboratories of the Washington State University Geo-analytical Laboratory following the methods of Knaack et al. (1994) and Johnson et al. (1999).

8. FT-IR Water Analysis

Following some polishing, the melt inclusions were then analyzed for H_2O on a Perkin Elmer Spectrum GX FT-IR spectrometer microscope attachment in an environment purged with N_2 at the University of Michigan. The calibration of Dixon et al (1995) was used to calculate the H_2O concentrations from the ~3500 cm^{-1} absorbance peak.

4. Major Element Analysis and Correction

A Cameca SX100 Electron Microprobe at the University of Michigan was used to analyze for the major element concentrations in melt inclusions and the host olivine. Measurements were made with an accelerating voltage of 15keV, a beam current of 4nA and a 5µm defocused beam. Counting times were typically 20s, with a sub-counting

routine on Na to monitor for potential beam damage to the glasses. The sub-counting routine broke counting for Na into 5s increments, allowing the user to monitor for time-related changes in counts that would result from Na migration during beam damage to the melt inclusion glass. No evidence for beam damage was detected. This routine also allowed for correcting back to t = 0 if beam damage were detected, allowing for good quality analysis even if beam damage occurs. Elemental standardization was achieved with known natural silicate mineral samples.

Most inclusions required a correction for host-olivine dissolution resulting from the homogenization procedure. This was done by incrementally subtracting the composition of the host olivine until the distribution coefficient (K_D) for Fe-Mg exchange between the olivine and glass reached ~0.3, assuming a Fe_2O_3/FeO of 0.18, based on a review of published Fe_2O_3/FeO (Leeman, 1976; Ross, 1983) for the region. Many of the inclusions required corrections of less than 10 wt% olivine removal; a few inclusions, however, required larger corrections as high as 25 wt% olivine removal. No correction was performed on plagioclase-hosted inclusions, despite similar evidence for plagioclase dissolution, because the greater variability of K_D values (e.g., Lange et al., 2009) for any exchanges in plagioclase would contribute large errors to any attempted correction.

Uncertainty with respect to the actual K_D for Fe/Mg exchange between olivine and liquid introduces error to the correction procedure (see Toplis, 2005 for details). The uncertainty with respect to the actual Fe_2O_3/FeO of the melt inclusions, which must be assumed to perform the correction, is an even more important source of error in the

correction. Further uncertainty is added because some of the melt inclusions may have lost iron to sulfide globules, which do not readily homogenize during heating in the piston cylinder (Danyushevksy et al 2002). Sulfide formation is observed in some inclusions as small black spheres of less than 10% of the volume of the host inclusion. MgO concentrations are particularly problematic, showing significant scatter.

The correction procedure generates more realistic data for other elements which are much less sensitive (no more than a 7% variation between extreme assumptions in Fe_2O_3/FeO) to assumptions made in the correction due to their absence in olivine. For these reasons FeO, and even more so, MgO, in this data set are not particularly useful for interpretation, though they are shown for the sake of completeness. The other major and trace elements exhibit much more scatter than can be explained by the correction procedure; therefore they must reflect actual heterogeneities in the melt inclusions. Despite the resulting scatter, meaningful trends can be observed which provide valuable information regarding the source of the observed volatiles.

5. Volatile and Trace Element Analysis

Selected melt inclusions from each basalt sample were analyzed for H_2O, F, Cl and S with the Cameca 1280 SIMS using a 10 µm Cs^+ ion beam at Woods Hole Oceanographic Institution following the method used in Le Voyer et al. (2008). A set of volatile-rich basalt glass samples was used for calibration. No systematic discrepancies were found between water analyzed via FT-IR and SIMS for low water concentrations, but at higher concentrations (over ~2 wt%) SIMS systematically found more water. This discrepancy is attributed to the fact that the Dixon et al. (1995) calibration does not use

any glasses over 2.5 wt% water. Glasses used for SIMS calibration had as much as 6.5 wt % H_2O.

A large subset of inclusions was analyzed for selected trace elements using a laser ablation inductively coupled plasma mass spectrometer (LA-ICP-MS) at Oregon State University. The laser spot size was 50µm, and the pulse rate was set to 4Hz. Analyses were calibrated using the ^{43}Ca peak in the sample, while regularly monitoring the BCR-2G and BHVO-2G glass standards. Kent et al (2004) gives a general outline of the analytical procedures employed in this study.

Results

Tables 3.1 and 3.2 present corrected major-oxide, trace element and volatile concentrations for olivine-hosted melt inclusions, one set of plagioclase-hosted melt inclusions, and the host whole rocks from seven basalt samples collected from the CRB-OPB region.

1. Olivine and plagioclase compositions

Main-eruptive-stage-CRB olivine samples JD-4 and GR-1A have compositions of Fo_{76-81} and Fo_{85}, respectively. Because only two olivine grains of similar composition were recovered from GR-1A, analyses were also attempted on plagioclase-hosted melt inclusions from this rock. Plagioclase compositions had a range of An_{78-89}; only three samples out of ten were under An_{85}. Late-eruptive-stage olivine samples (MG and JV prefixes) ranged from ~Fo_{77} to Fo_{87} with no more than ~2% Fo variation in a given

sample, indicating limited evolution of these magmas. In both cases no correlation was observed between H_2O and Fo (or An) content.

2. Major oxide compositions of melt inclusions

Major oxide compositions for melt inclusions from both the main-eruptive-stage-CRB and late-eruptive-stage basalts formed coherent trends complicated by scatter resulting primarily from interaction of the liquid with its olivine host both before and after homogenization (Fig. 3.6). Data for MgO show wide scatter as a result of the high uncertainty in the correction procedure for MgO, and therefore are not useful for interpretation. The other oxides are less sensitive to the correction procedure and show much less scatter.

Bulk-host-rock compositions generally plot towards the more evolved end of the range of compositions defined by the melt inclusions, but compositions for the most evolved melt inclusions are always more enriched than the host rock. However, plagioclase-hosted melt inclusions from sample GR-1A show strong evidence for interaction with their host plagioclase in the form of strongly elevated aluminum concentrations relative to the host rock (Table 3.1 and Table 3.2).

Classification diagrams of total alkalis (Na_2O+K_2O) vs. silica for the main-eruptive-stage-CRB melt inclusions (Fig. 3.2A) show that most inclusions are of sub-alkaline to mildly alkaline composition. The host rock for GR-1A plots in the field of basaltic andesite whereas its melt inclusions define a trend of generally more alkaline compositions. Alkaline compositions are probably enhanced by plagioclase dissolution during homogenization. Melt inclusions for JD-4 form a coherent evolutionary trend

toward the composition of their host rock. Conversely, the total alkalis vs. silica diagram for the late-eruptive-stage melt inclusions (Fig. 3.2B) shows primarily mildly alkalic compositions for melt inclusions and host rocks, with a few inclusions trending toward strongly alkalic compositions. The host rocks are generally less alkalic, but more siliceous than their melt inclusions.

The plots between water and major oxides for main-eruptive-stage-CRB lavas (Fig. 3.6) show primarily flat trends for sample JD-4. This demonstrates limited variability in chemistry during the degassing of water. Sample GR-1A shows trends that are consistent with variable amounts of plagioclase dissolution into the melt inclusions. In opposition to previously noted trends, melt inclusions from several of the late-eruptive-stage lavas show steep trends in plots of water vs. incompatible major oxides (Fig 3.7) – particularly in TiO_2, Na_2O, and K_2O. All of these oxides experience strong enrichments as water concentration drops; indicating that the melt is degassing during the evolution and/or crystallization of the rising magmas.

3. Trace element compositions of melt inclusions

Melt inclusions from both main-eruptive-stage-CRB samples show trace element patterns that are broadly similar to those of their host rocks (Fig. 3.3). However, in the GR-1A melt inclusions there is a noticeable depletion in Th, U and Rb that modifies the shape of the trace element patterns and clearly sets them apart from the patterns for the host rock.

Overall, the melt inclusions from late-eruptive-stage samples are even more similar and less variable than the melt inclusions in the main-eruptive-stage-CRB lavas

(Figs. 3.4 and 3.5). There are, however, a few exceptions. Sample MG-6 shows two melt inclusions with large enrichments in U relative to what is observed in the host rock and other melt inclusions (Fig. 3.4, Table 3.2). In sample JV-7, several of the melt inclusions fail to show the rather large enrichment in Sr shown by the host rock. Samples MG-1 and MG-4 both show a strong enrichment in Ba in the host rock, mirrored in the melt inclusions.

4. Water in melt inclusions

The maximum water concentrations observed in the main-eruptive-stage CRB melt inclusions occur in sample JD-4 (Picture Gorge Basalt) and reach as high as 2.4 wt% H_2O. The maximum water concentration observed in GR-1A (Grande Ronde Basalt) was 1.1 wt% in one of the olivine-hosted melt inclusions. The plagioclase-hosted melt inclusions did not show any water concentrations above 0.8 wt%.

Maximum water concentrations for late-eruptive-stage melt inclusions were 3.4 and 4.2 wt% observed in sample MG-1, an unclassified basalt from the Malheur Gorge. No other melt inclusions had more than 2 wt% H_2O. Maximum water concentrations in the two Jordan Valley (JV)melt inclusions were only 1 wt%, while all three MG samples had water concentrations over 1 wt% and two out of the three had water concentrations over 1.5 wt%.

In all cases the highest observed water concentrations are interpreted as magmatic minima. This interpretation is supported by the observation that maximum

water concentrations are generally noted to occur in less differentiated melt inclusion compositions, as will be discussed in greater detail below.

5. Other volatiles in melt inclusions

The highest S concentrations observed in melt inclusions are 2715 ppm and 2854 ppm in sample MG-1, in the same two melt inclusions that yielded the highest water concentrations. The maximum S in main-eruptive-stage-CRB melt inclusions is 1631 ppm in sample JD-4. Most of the other melt inclusions showed less than 1000 ppm S. A plot of S (ppm) vs incompatible major element concentrations (Fig. 3.8) for late-eruptive-stage melt inclusions exhibits a small negative correlation, indicating that S is degassing during differentiation in the same way as water.

Maximum F and Cl concentrations for main-eruptive-stage-CRB melt inclusions are 2606 ppm and 663 ppm, respectively. As expected, the highest F concentration is observed in sample JD-4. However the maximum Cl concentration is found in sample GR-1A. Late-eruptive-stage melt inclusions are lower in halogens, with maximum F and Cl concentrations of 721 ppm and 379 ppm, respectively. Again the maximum F concentrations are observed in sample MG-1, which is also the most water and sulfur rich of the samples. Surprisingly sample JV-7 hosts the highest late-eruptive-stage Cl concentration, despite otherwise being the least volatile-rich sample observed. Plots between the halogens and the incompatible major oxides (Fig. 3.8) also yield a negative correlation for late-eruptive-stage melt inclusions, indicating that both halogens are degassing during evolution, similar to S and H_2O.

Discussion

8. Chemical Variability in Melt Inclusions

Major oxide, trace element and volatile compositions for the olivine-hosted melt inclusions display a great deal of heterogeneity both in the main-stage and the late-eruptive-stage basalts scattered throughout the CRB and OPB. Observed heterogeneity may be partially explained by a number of processes as follows. Magmatic degassing will cause crystal growth, creating trends of declining volatile concentrations with increasing concentrations of incompatible elements (Johnson et al. 2008). Fractionation leads to co-variation of major oxides (e.g., rising Na_2O as MgO decreases), and may also lead to enrichment of volatiles in the residual melt. "Edge effects" are produced by rapid crystal growth exceeding the diffusion rates of some elements. Edge effects create a boundary layer of liquid that is significantly different from that of the bulk liquid. Melt inclusions will tend to trap this boundary layer, which will not be relevant to the bulk liquid composition due to the removal of certain elements by local crystal growth and enrichment of others too slow to diffuse out of the residual magma. Data on elemental diffusion rates in basaltic liquids which have bearing on this process are presented in Kress and Ghiorso (1995) and Chen and Zhang (2008).

A sulfide phase may grow in some melt inclusions, removing Fe and S, which could cause an inclusion to show anomalously low Fe and S concentrations. These sulfide phases will not dissolve back into the melt inclusion during homogenization (Danyushevsky et al. 2002). Interaction of the melt inclusion with olivine either soon after entrapment or during homogenization in the piston cylinder is manifested

primarily as anomalously low or high MgO concentrations, and anomalous apparent k_D values between olivine and the melt inclusion (Danyushevsky et al. 2002; Schiano et al. 2004; Churikova et al. 2007). As noted previously, a correction was undertaken to minimize this effect in the data presented.

9. Post-entrapment degassing of melt inclusions

There is limited evidence for degassing of olivine-hosted melt inclusions in either main-stage or late-eruptive-stage basalts of the CRB-OPB region. However, the samples that do show some evidence of post-entrapment degassing are those that preserve the highest observed water concentrations (MG-1, MG-6). This supports the conception that observed water concentrations are minimum values. In the event of post-entrapment degassing of inclusions a trend between a volatile and some major oxide or trace element will be readily apparent, in which case degassed inclusions will plot off the defined trend. Given the possibility of small degrees of degassing even in cases where trends are still apparent, the measured water concentrations for all melt inclusions have to be minima compared to the actual concentration of the original magma.

The two main-stage samples (GR-1A and JD-4) were collected from dikes; they therefore would have remained hot for somewhat longer periods of time than basalts that had actually erupted at the surface, which should have encouraged post-entrapment degassing. However GR-1A and JD-4 plots of major oxides vs. water concentrations (Fig. 3.6) show near-vertical and near-horizontal trends, respectively. In the case of GR-1A, the near-vertical trends may indicate that the dike remained hot long

enough to allow diffusion and/or degassing to evenly distribute water among the melt inclusions. Post-entrapment degassing may have occurred in JD-4; however, the flat trend makes demonstrating this virtually impossible.

In the late-eruptive-stage melt inclusions only samples MG-1 and MG-6 show significant evidence for post-entrapment degassing of water. Both samples show fairly well developed trends between incompatible major elements, particularly Na_2O and K_2O, (Fig. 3.7) with a few points falling below those defined trends, as a result of water loss after entrapment of the inclusion. The other late-eruptive-stage melt inclusions either show too much scatter or do not have points that fall off their defined trends, and therefore post-entrapment degassing is not detected in these cases.

Detected post-entrapment degassing most likely occurred during transport to the surface or immediately after eruption, before the lavas cooled. Because inclusions with obvious ruptures or cracks were avoided, degassing must have occurred either through micro-fractures or by diffusion directly through the olivine crystal lattice. The higher solubility of water at the homogenization pressure (Moore et al., 1998), combined with the short time at high temperature should have prevented any significant water degassing by the same processes during homogenization in the piston cylinder apparatus.

10. Equilibrium crystallization or edge effects?

Observed trends between water and major oxides (Figs. 3.6 and 3.7) are broadly consistent with equilibrium crystallization of olivine and plagioclase. These are the two main phenocryst phases in the host rocks of the studied olivine-hosted melt inclusions.

Late-eruptive-stage melt inclusions show water concentrations dropping as incompatible major oxides, especially TiO_2, Na_2O and K_2O and trace element Sc, Nb, U and Rb, concentrations increase (Fig. 3.7 and Fig. 3.10), indicating that water is degassing during crystal growth. In fact, water degassing may be the process driving this crystallization by rapidly increasing the liquidus temperature for the melt. Main–stage CRB melt inclusion plots of major oxides vs. water (Fig. 3.6) show little slope, thus making an interpretation of water's role in their evolution difficult. These samples were taken from slowly cooled dikes, with the redistribution of water through diffusion a distinct possibility, therefore providing an explanation for this inconsistency. This would tend to blur or obliterate trends. In contrast, plots of Sc, Y and to a lesser extent Rb, vs. water (Fig. 3.9) actually show a weak positive correlation for sample JD-4, suggesting that water may not be degassing as much, and to the contrary, may actually be increasing in concentration slightly during crystallization of this melt. This possibility is not borne out, however, when H_2O/Ce vs. water is considered (Fig. 3.12); this plot shows a positive slope, whereas if water were becoming enriched during differentiation, the H_2O/Ce ratio would stay more or less constant.

The other volatiles (Cl, F and S) all seem to follow the same trends as water. Some plots of the other volatiles vs. the major oxides SiO_2 and K_2O (Fig. 3.8) also yield negative correlations, albeit a fairly weak one for Cl in the late-eruptive-stage melt inclusions. It seems that there are actually two sample populations with respect to F: low-F and high-F populations; the negative correlation is most evident in the high-F population. This observation contrasts slightly with the observations of Sadofsky et al

(2008), who found similar behavior for Cl and S in the Central America Arc; but recognized a positive correlation between F and major elements, indicating that F was not degassing with the other volatiles, presumably because it has a higher solubility in the magma. A similar observation is made for F in olivine-hosted melt inclusions in both syn-caldera and post-caldera basalts of the Snake River Plain (Stefano et al., 2010). Late-eruptive-stage basalts of the OPB must either have a lower-than-normal solubility limit for F or are losing F through some other process.

Elemental diffusion in magmas occurs at a finite pace; thus it is possible for the composition of an olivine-hosted melt inclusion to be modified by an "edge effect" if the crystallization rate of an olivine grain significantly exceeds the diffusion rate of a specific element. In the case of olivine, this would cause the boundary layer, and thus the melt inclusion, to become enriched in all elements incompatible with the growing olivine (e.g., Johnson et al. 2008). This effect is of concern for melt inclusion volatile studies because it may cause volatiles to be enriched in the melt inclusion beyond the actual levels in the bulk magma. However, this effect does not appear to have significantly affected the studied melt inclusions.

While most major oxide abundances increase as water concentration decreases (Fig. 3.7), CaO does not, and Al_2O_3 has a less steep slope than the alkalis, indicating that they are being affected by the crystallization of plagioclase. This demonstrates that normal crystallization processes, rather than edge effects dominate the chemistry of the melt inclusions. This is not to imply that the observed elemental abundance patterns

were not impacted by the "edge effect" at all. In fact, alkalis and some other incompatible elements are enriched in some melt inclusions significantly beyond the bulk rock composition, indicating that they are not representative of a real liquid, and giving credence to the possibility that edge effects are important locally. It is clear that the effect was simply overwhelmed by normal crystallization processes. However, even though the edge effect might influence some of the element abundance patterns, it would not necessarily affect water because this volatile diffuses approximately an order of magnitude faster than major oxides (~10^{-10} m^2/s, compared to ~10^{-11} m^2/s, respectively) (Zhang and Stolper 1991; Chen and Zhang 2008). In fact, the observation that the highest water concentrations are generally found in the least differentiated melt inclusions demonstrates that enrichment of water and other volatiles due to crystallization and/or the edge effect is overwhelmed by degassing that occurs as these processes are ongoing, further supporting the notion that the observed water concentrations are minima.

11. Implications for shallow crustal storage

The high water concentrations preserved in some of the melt inclusions rule out the possibility of long storage times in the crust for the host magmas. Demouchy and Mackwell (2003) report diffusion rates for water through olivine to be ~10^{-13} m^2/s, indicating that water could diffuse through a 1-mm wall of olivine to escape an inclusion in only a few days. The observed concentrations support the conclusion that these basalts were not stored for very long, at least not after water was degassed. Severs et al.

(2007) found that melt inclusions in quartz from the Bishop Tuff lost most of their water after only seven days of heating at 800° C and one kbar of pressure. Portnyagin et al. (2008) found that "dry" olivine-hosted melt inclusions placed in a water bearing melt could gain up to 2.5 wt% water after only two days at 1140° C. Although the conditions in the Portnyagin et al. (2008) experiment are not likely to occur in nature, it illustrates how quickly water can pass through the olivine barrier encapsulating a melt inclusion. Johnson et al. (2008) examined melt inclusions from various stages of an eruption at Volcán Jorullo, Mexico, and found that early erupted inclusions preserved high water concentrations and had short estimated olivine storage times(<200 days). Any amount of storage would cause melt inclusions to lose water. As soon as the magmas hosting melt-inclusion-bearing olivine grains degas, melt inclusions will begin to re-equilibrate with the dryer magma and will do so in only a few days. The only way that the high water concentrations observed in some of the olivine-hosted melt inclusions from the CRB-OPB could be preserved, is for eruption to occur within a few days after degassing, thus making long storage impossible.

12. Water-fluxed melting in the CRB-OPB?

Sadofsky et al. (2008) suggested that the association of highest water concentration with the least differentiated melt inclusions in arc basalts from Central America is due to water fluxed melting. The argument was based on the idea that the addition of water would increase the melt fraction by depressing the peridotite solidus temperature (Taylor and Green, 1988), thereby diluting the concentrations of incompatible elements. Although observed water concentrations in the late-eruptive-

stage rocks of the CRB-OPB exceeded 4 wt%, they are still lower than water concentrations in the Central America Arc, at ~6 wt% (Sadofsky et al. 2008). Furthermore, basalts from the CRB-OPB are both more evolved and more crystallized than the lavas examined by Sadofsky et al. (2008), and so the melt inclusions' variations in chemistry should be controlled more strongly by crystallization effects than they appear to have been in the Central America Arc. Sadofsky et al. (2008) support their argument further by noting a positive correlation between Ba/La and water concentration, indicating the addition of subduction-derived fluids to the source.

Conversely, weak correlations were observed between Ba/La and water concentration (Fig. 3.11) for CRB-OPB melt inclusions that are negative, if anything in late-eruptive-stage inclusions; meaning that the melt inclusions are not recording the instantaneous addition of subduction fluids. These observations favor the interpretation that the addition of the water found in CRB-OPB melt inclusions is not the main driving force behind the melting that produced the eruptions in this province and instead represents residual hydration remobilized by melting triggered by other processes.

13. Mantle source for volatiles

Water must have been present in abundance in the mantle/lower crust source region for CRB-OPB basalts. This study shows that all volatiles tend to have higher concentrations in less differentiated melt inclusions; therefore volatiles are clearly being lost during the subsequent crystallization of the melts. Furthermore, H_2O/Ce ratios plotted vs. H_2O (Fig. 3.12) also indicate that water concentrations are highest when

H_2O/Ce is highest in all cases. It is important to recognize that the inclusions are only recording melt parameters at the fairly shallow levels of entrapment, certainly within the crust, as olivine gets on the liquidus. As such, it is not readily apparent whether the water originated in the mantle or lower crust.

14. The role of subduction-related fluids in CRB-OPB melts

Data collected in this study point to a subduction fluid as the source for water in olivine-hosted melt inclusions of the CRB-OPB region. Plots of Ba/La vs. Ba/Nb and Ba/Th vs. Rb/Nb, used to differentiate mantle source end members in trace element space by Weaver (1991), show that main-stage-CRB, and even more so, late-eruptive-stage melt inclusions, are variably affected by input of subduction fluids (Fig. 3.13). In Ba/La vs. Ba/Nb space, the mantle end members plot along a mixing line between primitive mantle compositions and average continental crust. CRB-OPB melt inclusions plot much closer to continental crust compositions than do any of the mantle end members, indicating that some continental material may have been added. However, in Ba/Th vs. Rb/Nb, melt inclusions from the main-eruptive-stage-CRB and even more so, from late-eruptive-stage samples MG-1 and MG-4 plot in a nearly vertical trend, indicating strong enrichment of Ba over Th. High Ba/Th ratios and overall Ba concentrations typify arc basalts, which can show patterns similar to those observed in the CRB-OPB samples, with just a few melt inclusions preserving extreme concentrations (Walker et al. 2003; Churikova 2007; Sadofsky et al. 2008). These High Ba/Th ratios are evident both in melt inclusions and the whole rocks, indicating that these are a robust characteristic, although some of the highest ratios may have been over enhanced by the

edge effect during entrapment. Although some of the other trace element characteristics of subduction fluids are absent, the high Ba/Th ratios remain difficult to understand without considering a subduction component. The drier late-eruptive-stage melt inclusions plot either closer to mantle compositions or, in the case of MG-6, toward average continental crust, indicating that MG-6 is probably the only sample strongly affected by crustal input.

The idea of a subducted component in the CRB-OPB is not new. Carlson et al. (1981), Carlson (1984) and Brandon et al. (1993) found arc-like isotopic signatures in the Picture Gorge Basalts (sample JD-4 in this study is one of these) and other CRB lavas. Takahahshi et al. (1998) also favor the presence of a subducted component in the source for the CRB basalts.

Water concentrations observed in both main-stage-CRB and late-eruptive-stage melt inclusions from the CRB-OPB exceed values obtained for Hawaii (0.8-0.9 wt%), a typical hotspot (Hauri, 2002). Furthermore, the trace element data discussed above indicates a subduction source for water in these melt inclusions. Taking these observations into account, it seems unlikely that water was introduced by the plume hypothesized for the CRB and SRP magmatic provinces, but rather was already present in the upper mantle when conditions to permit melting (e.g., plume impingement, basin and range extension, etc.) developed.

If we accept a subduction origin for water in the upper mantle/lower crust beneath the studied region, then the most likely source of that water is the Farallon Plate. Its subduction is believed to be the cause of the Eocene-age Absaroka Arc (Feely,

2003).Following the development of Basin and Range extension in much of the Northwest, its continued subduction as the remnant Juan de Fuca Plate produced the modern Cascades Arc. It is reasonable to deduce that not all water introduced to the mantle by the down-going plate was extracted by water fluxed melting during the generation of these arcs. Some residual hydration was left to contribute to melting when heated by the hypothesized impinging plume, or decompressed by Basin and Range extension that created the CRB-OPB and eventually the Yellowstone hotspot track.

One issue with this interpretation is that higher water concentrations are observed in some late-eruptive-stage melt inclusions than in the main-stage-CRB samples. Late-eruptive-stage inclusions are expected to be drier, assuming subduction is no longer contributing additional fluids, because they sample a mantle that has already been dehydrated by melting which produced the older basalts. In fact, MG-1, the sample with the highest water concentration, is not the oldest among the late-eruptive-stage flows. Because both the GR-1A and JD-4 samples were collected from dikes rather than from flows, it is possible that the slightly slower cooling rate of the dikes could have allowed melt inclusions to lose water by diffusion (see discussion above).

Further support for the possibility of water loss in the main–eruptive-stage-CRB melt inclusions is given by the observation of higher halogen (F and Cl) concentrations in main–eruptive-stage-CRB melt inclusions than in the late-eruptive-stage inclusions. Halogens are less prone to degassing than water (e.g., Sadofsky et al. 2008), and tend to remain in inclusions even after water has been lost. However, the possibility of late

enrichment of the CRB-OPB mantle with water cannot be ruled out, and may even be supported by the observation that maximum observed water concentration measured in younger sample MG-1 is higher than that in older sample MG-4. The youngest late-eruptive-stage melt inclusions do have the lowest water concentrations observed, showing a time-related depletion of water in the source region.

Conclusions

Major oxide, trace element and volatile (H_2O, S, F and Cl) data obtained from olivine- and plagioclase-hosted melt inclusions from seven samples of both main-eruptive-stage and late-eruptive-stage basaltic volcanism of the CRB-OPB region provide a valuable insight into processes leading to formation of this large igneous province, and influencing the volcanism across the region's ~17 million year magmatic history.

Significant concentrations of volatiles, especially water observed in amounts up to 4.2 wt %, were found in both main-eruptive-stage and late-eruptive-stage melt inclusions. Most of the observed melt inclusions had low volatile concentrations, attributable either to pre-eruptive or to post-entrapment degassing. A few, however, managed to maintain high water concentrations. This observation underlines the importance of analyzing a large number of melt inclusions in order to maximize the probability of finding high volatile concentrations if they are present. Halogen (F and Cl) concentrations were highest in main-eruptive-stage melt inclusions, but H_2O and S were significantly higher in two melt inclusions of late-eruptive-stage origin.

Although there is some sampling bias towards late-eruptive-stage melt inclusions, this finding appears to indicate at least the possibility that the hydration state of the mantle/lower crust source region beneath the CRB-OPB has increased since the initial (main-eruptive-stage) CRB-OPB volcanism. The youngest late-eruptive-stage melt inclusions systematically record the lowest volatile concentrations, indicating that continued volcanism in the region depleted volatiles in the mantle/lower crust source region.

The observation that the most volatile rich melt inclusions tend to have the least differentiated major oxide and trace element compositions demonstrates that high volatile concentrations are characteristic of the mantle/lower crust source region for basalts of the CRB-OPB and not a feature added later by crystallization effects. These trends also document the degassing history of the magma, which most likely occurred during transport toward the surface and crystallization. Crystallization itself may have even been triggered by degassing of melts. Furthermore, the correlation of high Ba/La and Ba/Th ratios with high water concentrations indicates that the observed volatiles likely originated in a subduction zone. If this is the case, then the dewatering of subducted Farallon Plate slabs is proposed as the most likely candidate for the source of volatiles in the CRB-OPB magma source. It is possible that subsequent impingement of the plume head that is presumed to have formed the Yellowstone hotspot track remobilized this residual hydration to create the basalts of the CRB and OPB.

Continued subduction after that time replenished the volatile content of the mantle source, which was then sampled by subsequent late-eruptive-stage melting. This was driven in part by decompression melting due to Basin and Range extension. As late-eruptive-stage volcanism continued throughout the region, it eventually depleted the volatile content of the source region, leading to relatively volatile-poor eruptive products in more recent times.

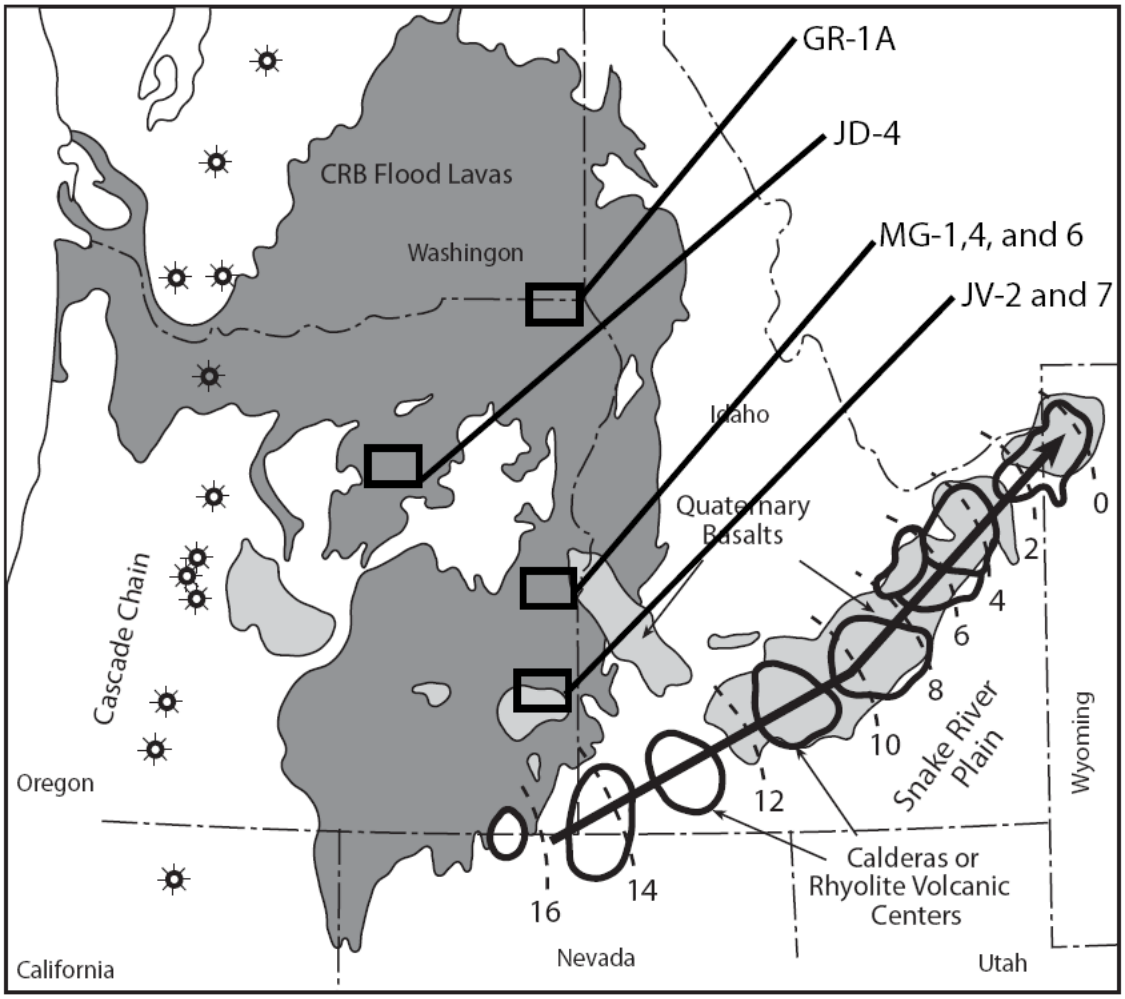

Figure 3.1. Schematic map of the Pacific Northwest region of the United states showing the locations of the Columbia River Basalts in relation to the rest of the Yellowstone hotspot. Also shown are Oregon Plateau Basalts (OPB)[shown as a southern extent of the CRB on this map], and the Snake River Plain (SRP). Approximate caldera locations and ages (in Ma) are shown along the Snake River Plain. Also shown is the Cascade arc. Black boxes show approximate sample locations in the CRB and OPB. Modified from Camp and Ross (2004).

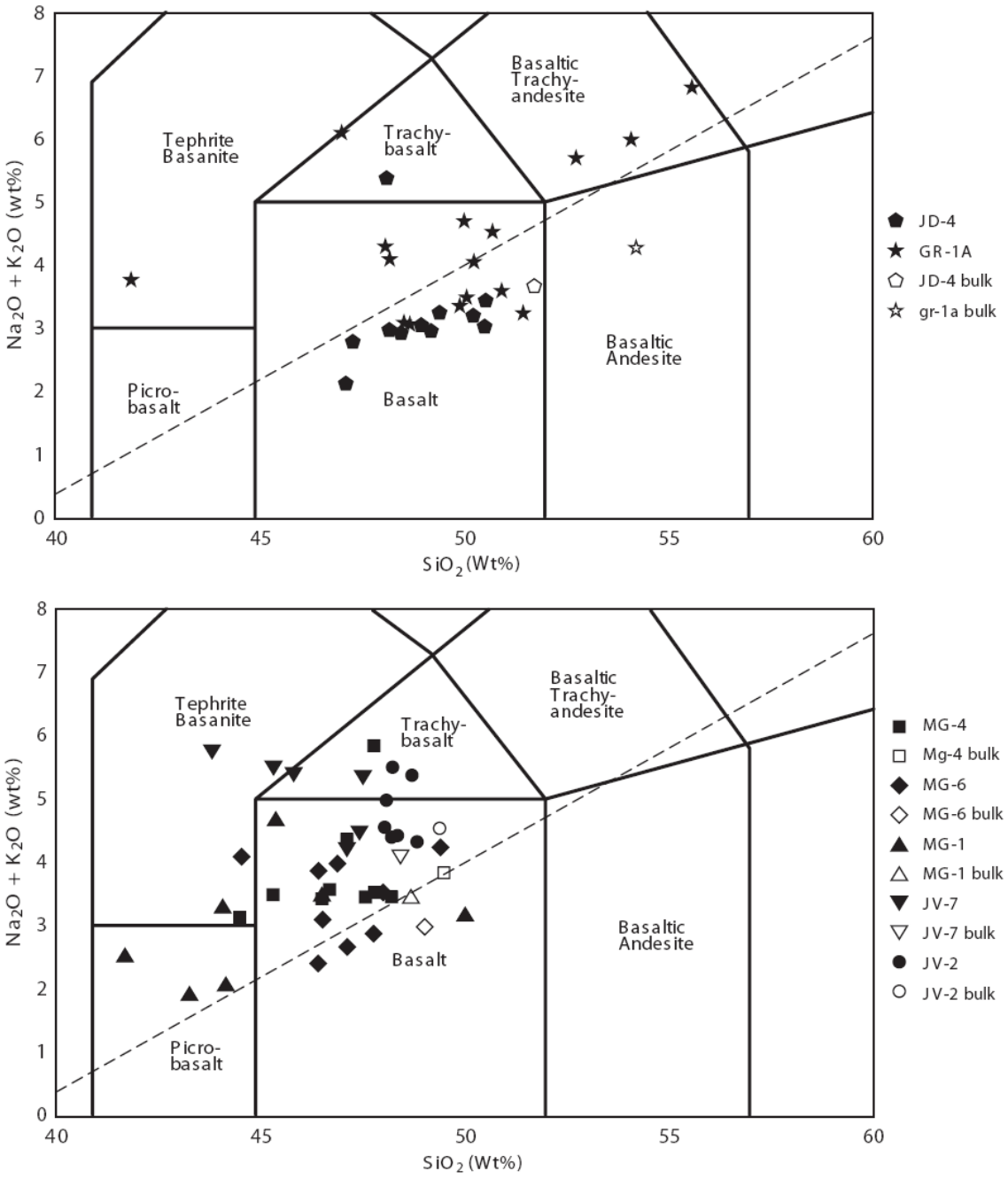

Figure 3.2. Total alkalis vs. Silica plots for main-eruptive-stage (top) and late-eruptive-stage (bottom) host lavas and olivine-hosted melt inclusions. Most inclusions are less differentiated and more alkalic than their host rocks.

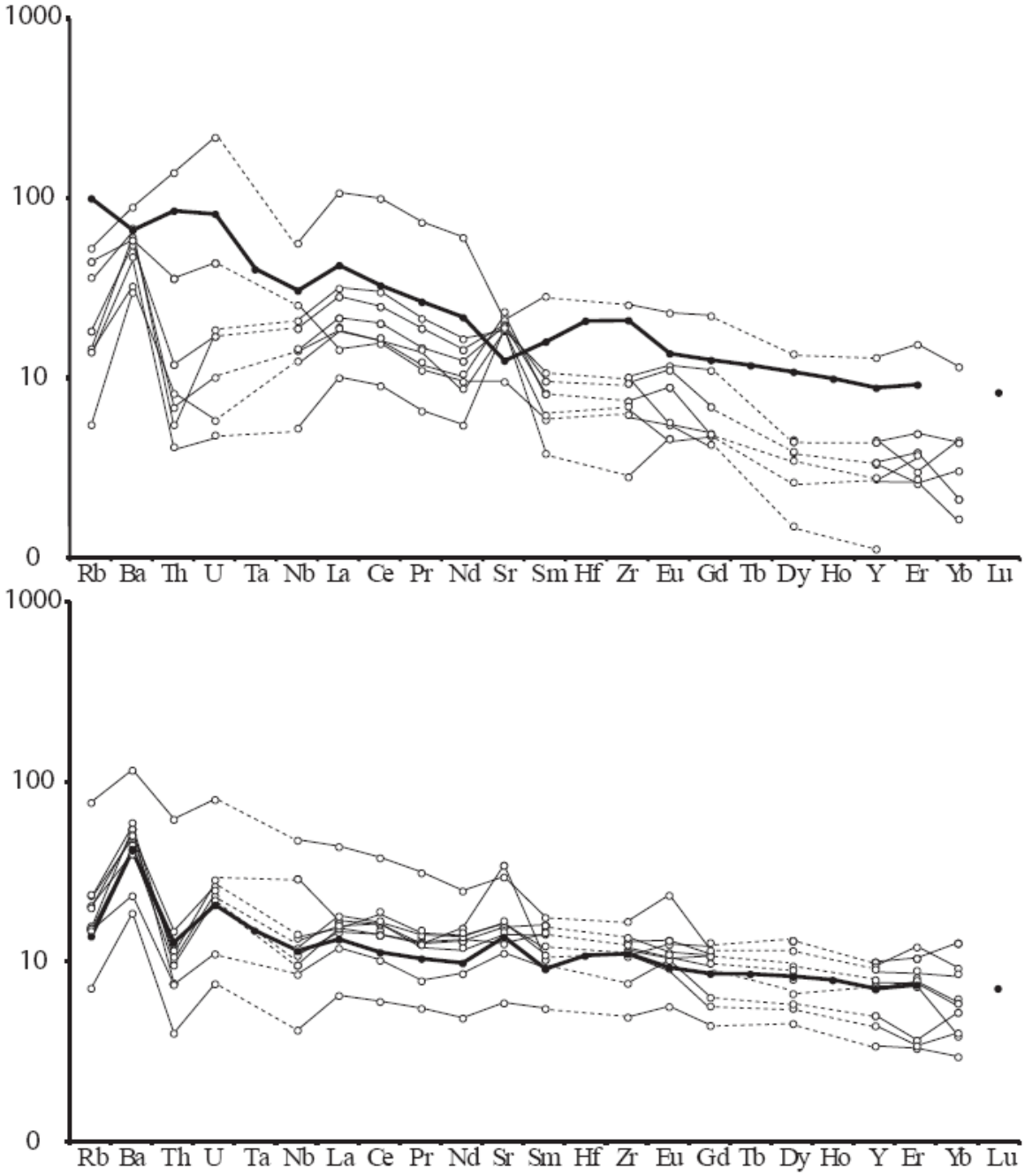

Figure 3.3. Trace element distribution diagrams for the main-eruptive-stage samples GR-1A (top) and JD-4 (bottom). The heavy, continuous lines represent the host rock composition; the other lines represent the melt inclusions. Melt inclusions are broadly similar to the host rocks, but some show noticeable depletion of Th compared to Ba.

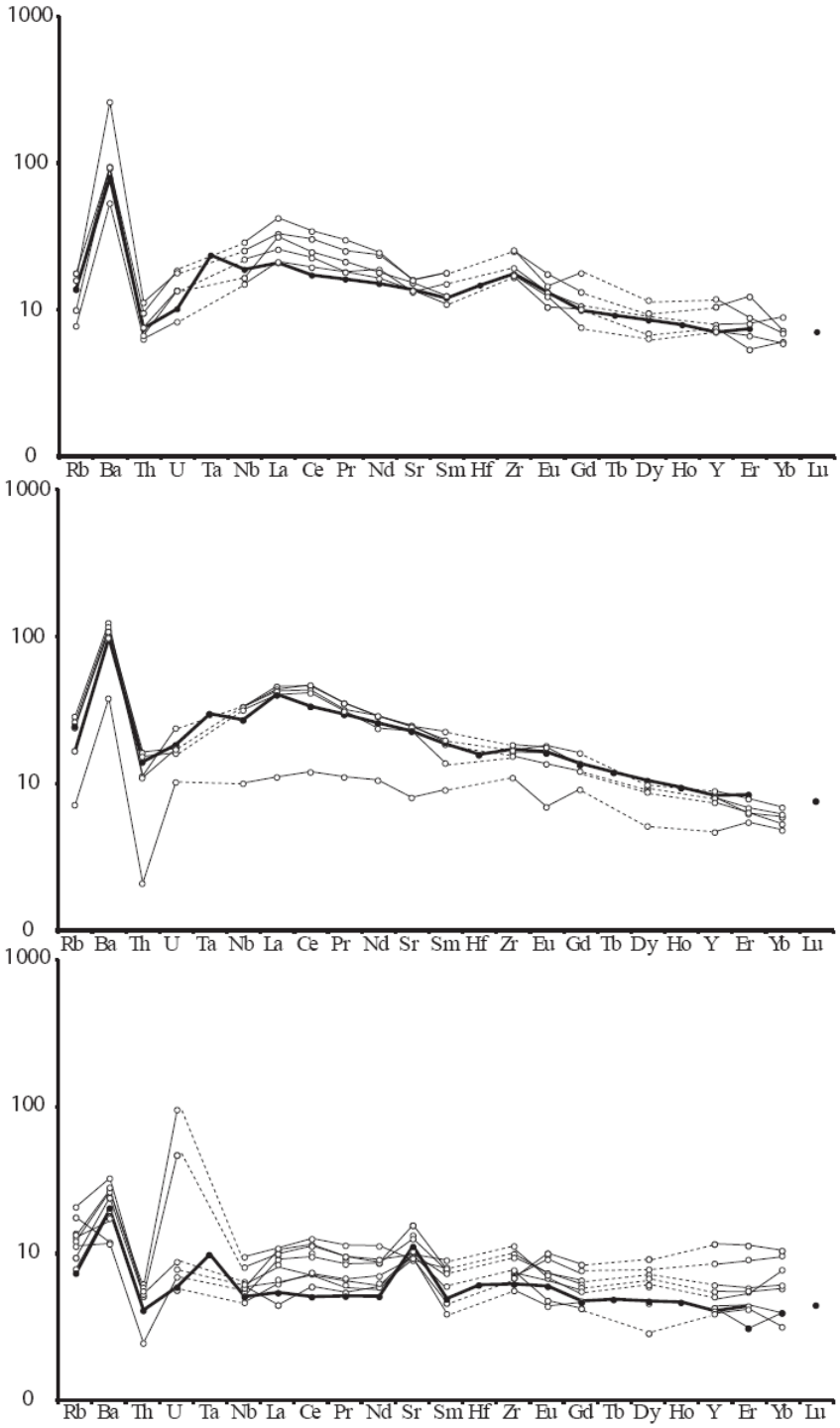

Figure 3.4. Trace element distribution diagrams for late-eruptive-stage samples MG-1 (top), MG-4 (middle) and MG-6 (bottom). The heavy, continuous lines represent the host rock composition; the other lines represent the melt inclusions. Melt inclusions are broadly similar to the host rocks, but some show noticeable depletion of Th compared to Ba. Two inclusions from MG-6 also show some very prominent U enrichment.

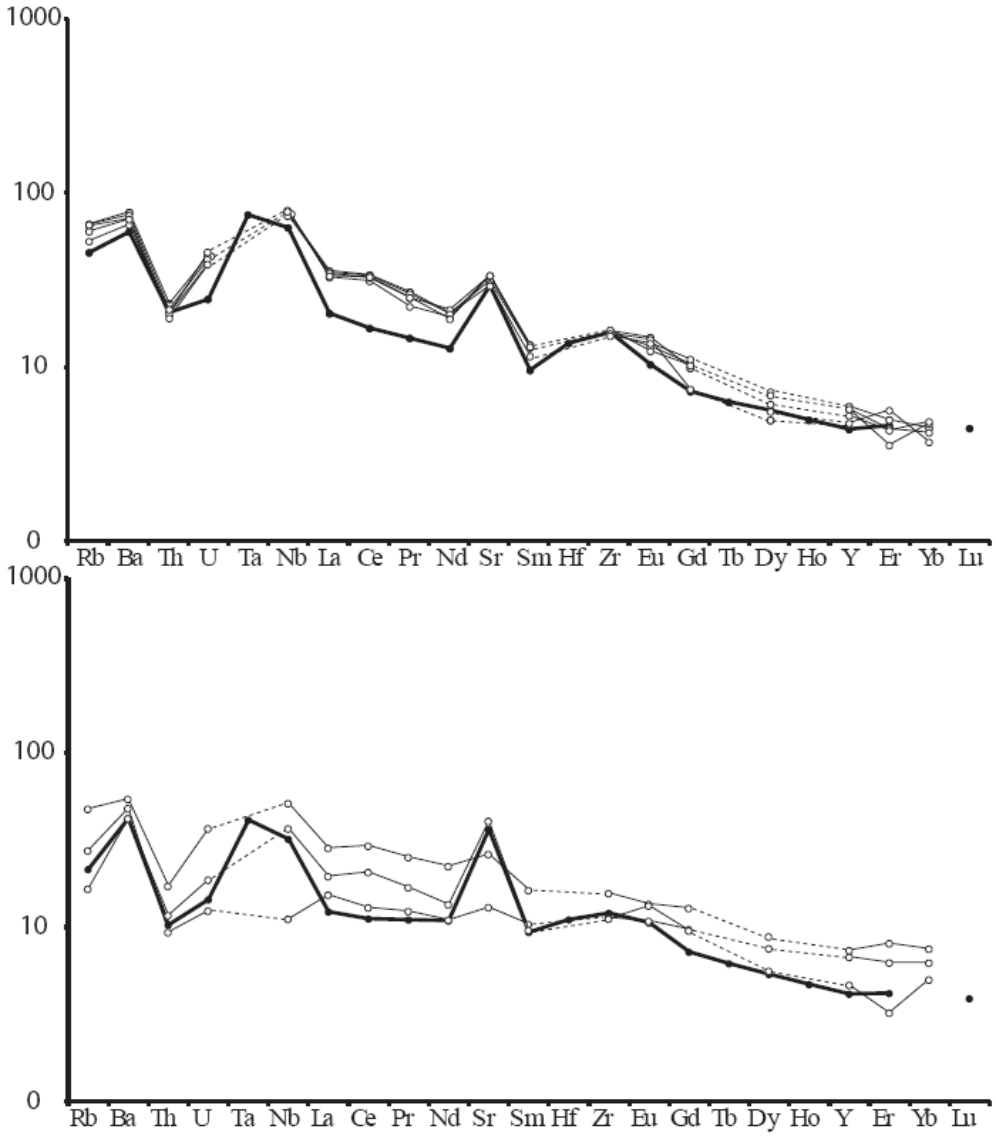

Figure 3.5. Trace element distribution diagrams for late-eruptive-stage samples JV-2 (top) and JV-7 (bottom). The heavy, continuous lines represent the host rock composition; the other lines represent the melt inclusions. Melt inclusions are broadly similar to the host rocks, with very few excursions, demonstrating that these lavas have had simpler histories than older lavas in the region.

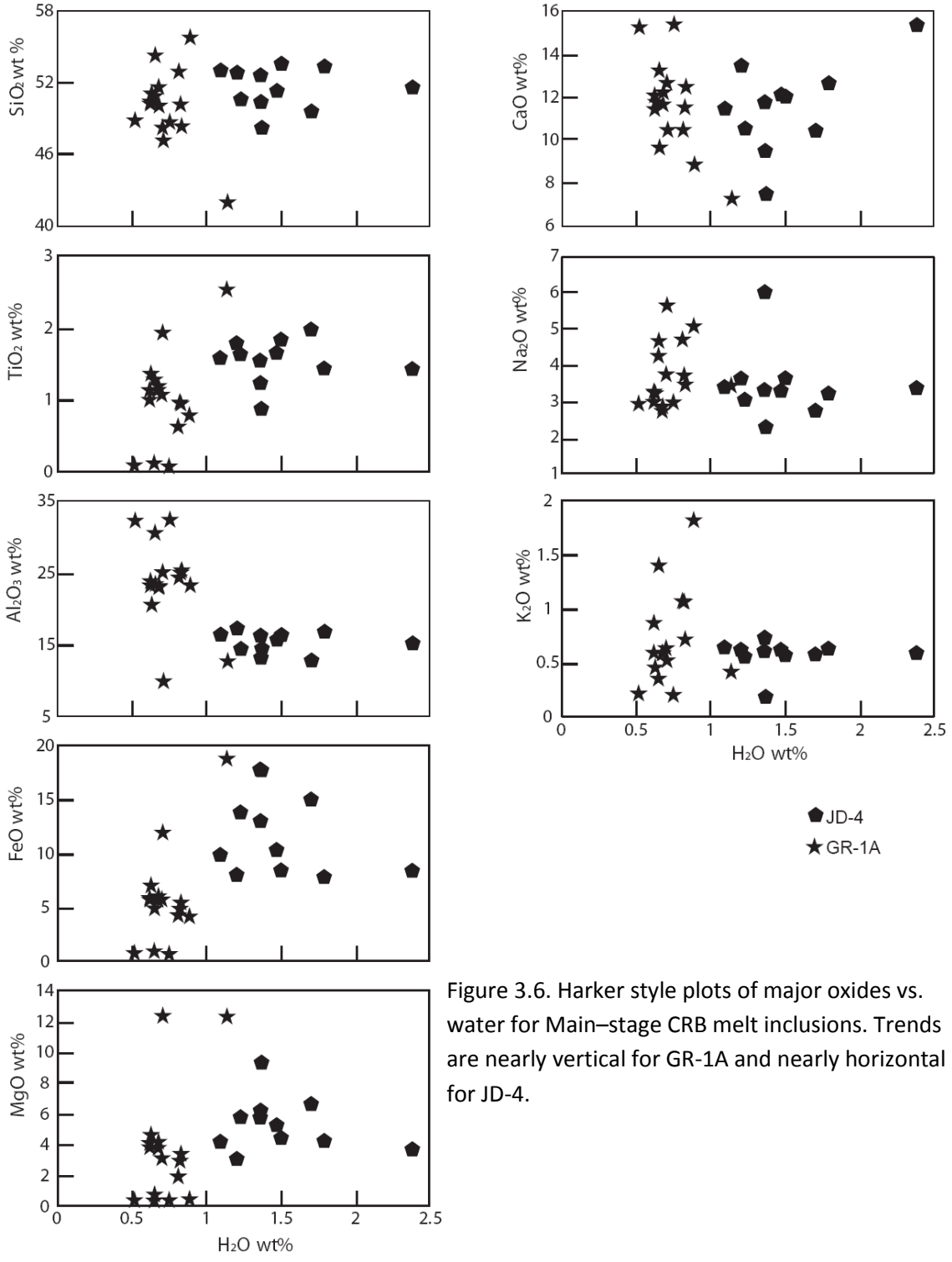

Figure 3.6. Harker style plots of major oxides vs. water for Main–stage CRB melt inclusions. Trends are nearly vertical for GR-1A and nearly horizontal for JD-4.

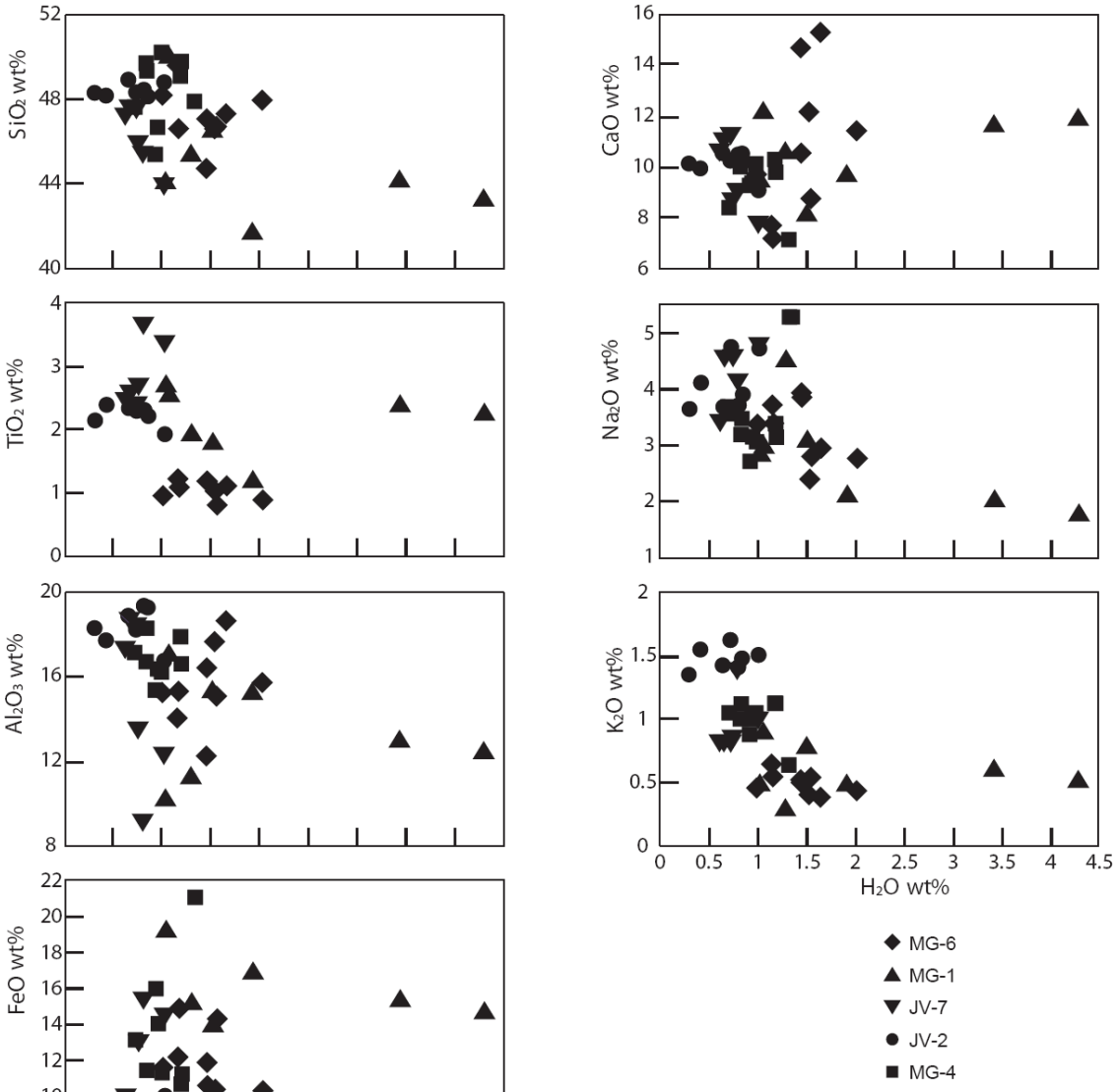

Figure 3.7. Harker style plots of major oxides vs. water for late-eruptive-stage melt inclusions. Trends show strong enrichments of incompatible elements as water concentrations fall. The highest water concentrations are found in the least differentiated inclusions, demonstrating that the water measurements are magmatic minima. Data for MgO are highly scattered because of interaction with the host olivine and are included for completeness only.

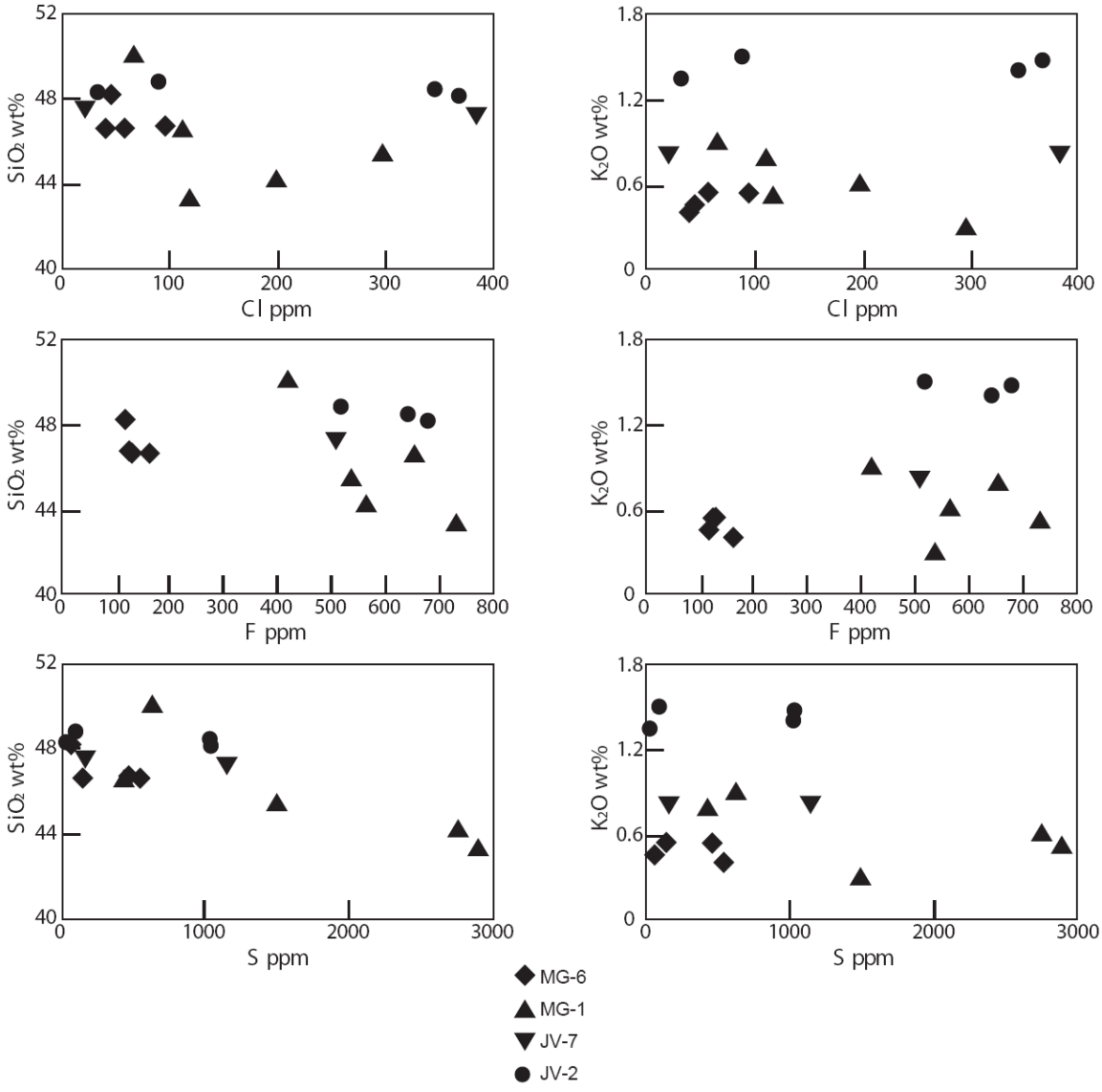

Figure 3.8. Plots of SiO_2 and K_2O vs. volatiles Cl, F and S for late-eruptive-stage melt inclusions. All volatiles show negative correlations indicating degassing during evolution as is seen with water.

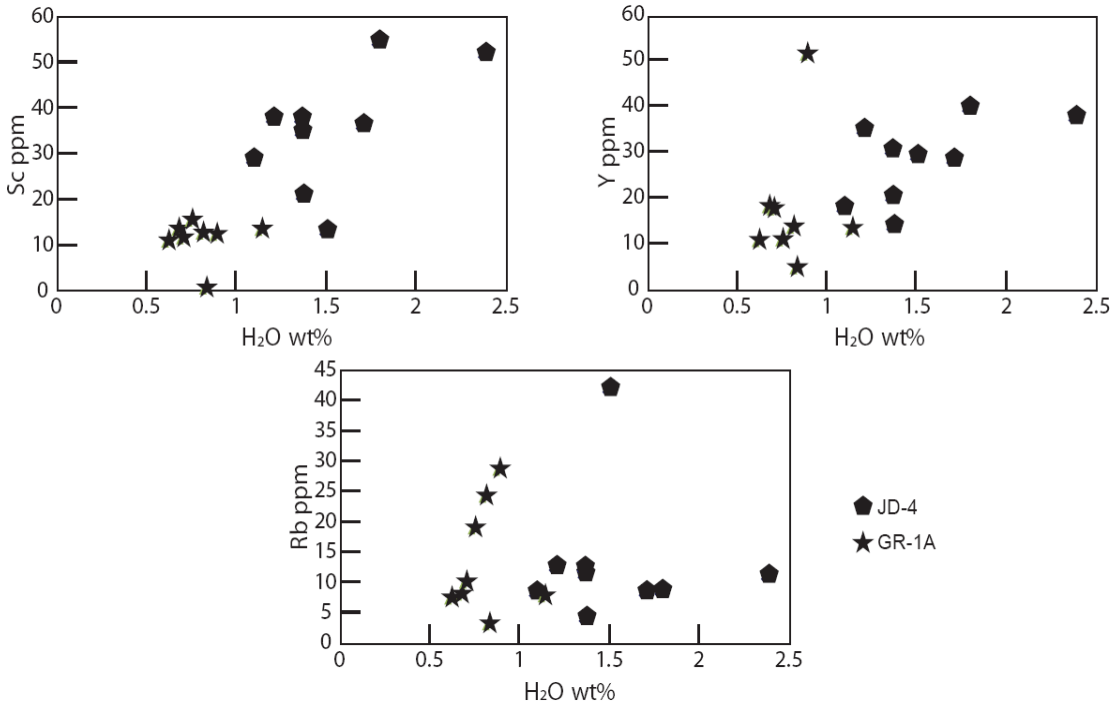

Figure 3.9. Plots of selected trace elements vs. water for the main-eruptive-stage melt inclusions. Note that Sc and Y suggest that JD-4 may actually be affected by some volatile enrichment during magma evolution, though Rb fails to confirm this.

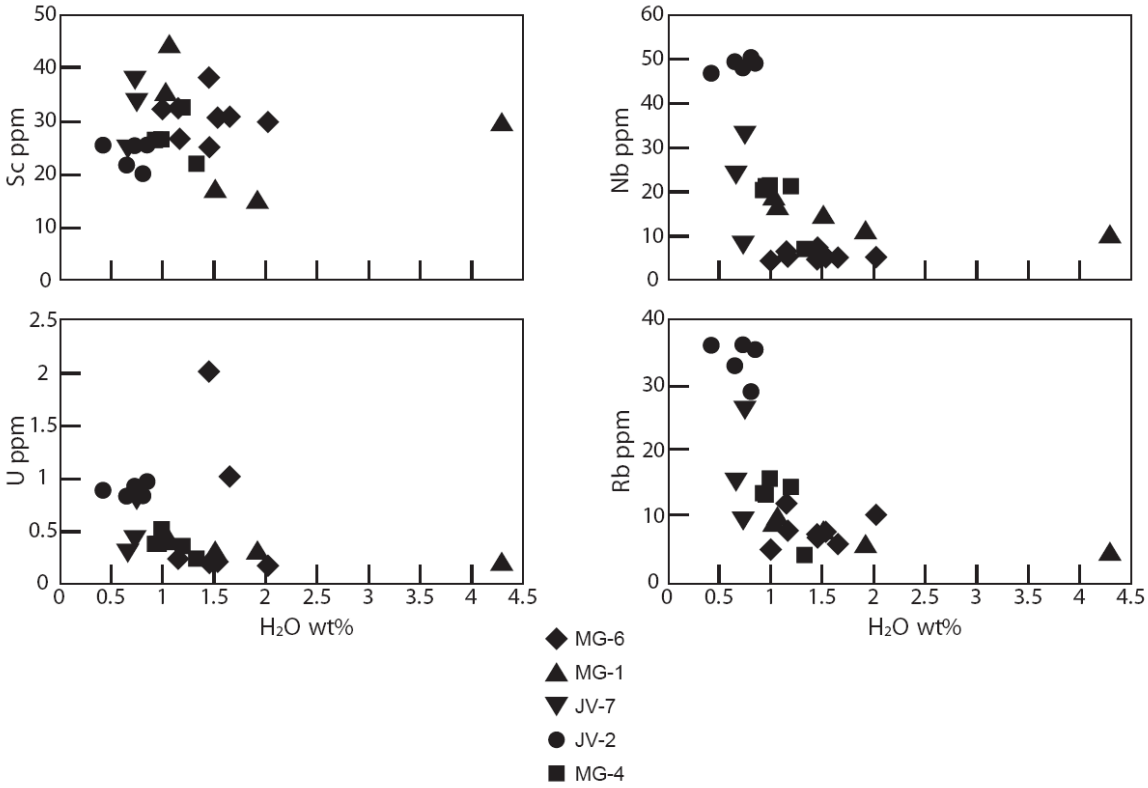

Figure 3.10. Plots of selected trace elements vs. water for late-eruptive-stage melt inclusions. Nb, U, and Rb all show trends similar to those observed for incompatible major oxides, supporting the interpretation of the maximum water concentrations reported to be magmatic minima.

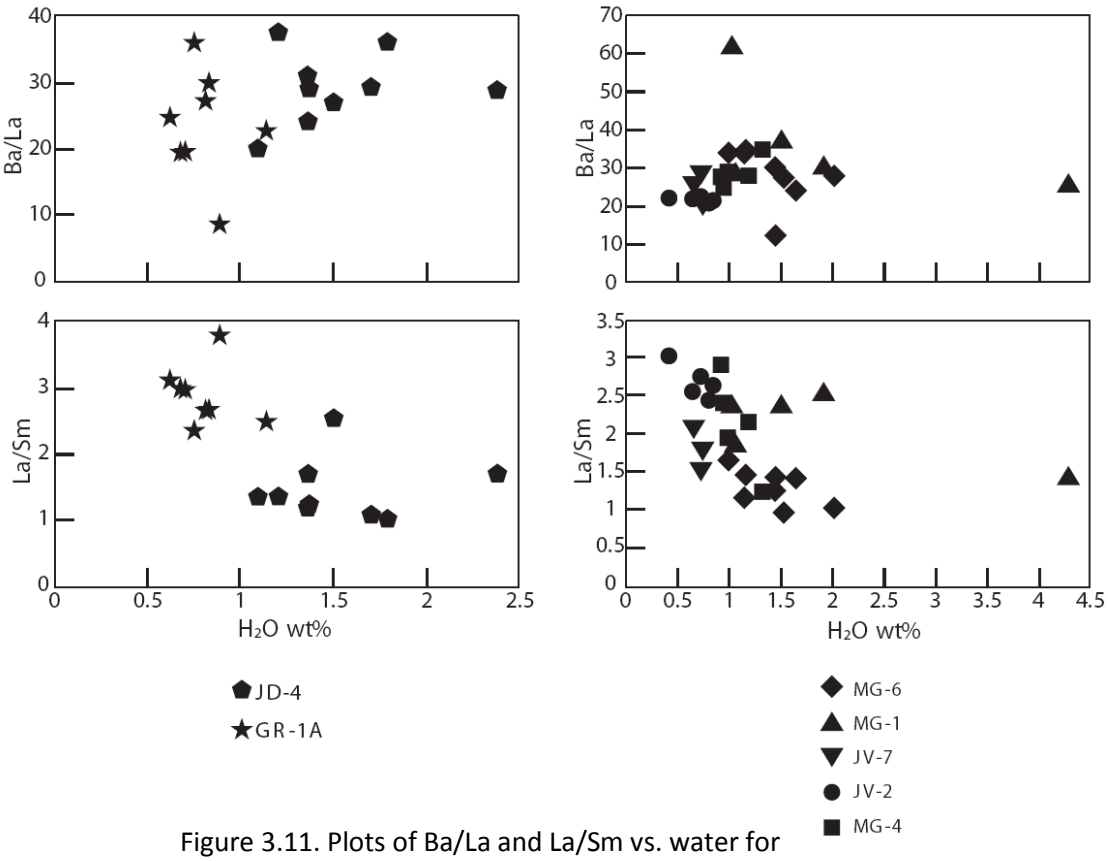

Figure 3.11. Plots of Ba/La and La/Sm vs. water for main-eruptive-stage (left) and late-eruptive-stage (right) melt inclusions. Weak correlation between Ba/La and water suggests that water-fluxed melting due to input of subduction fluids is unlikely.

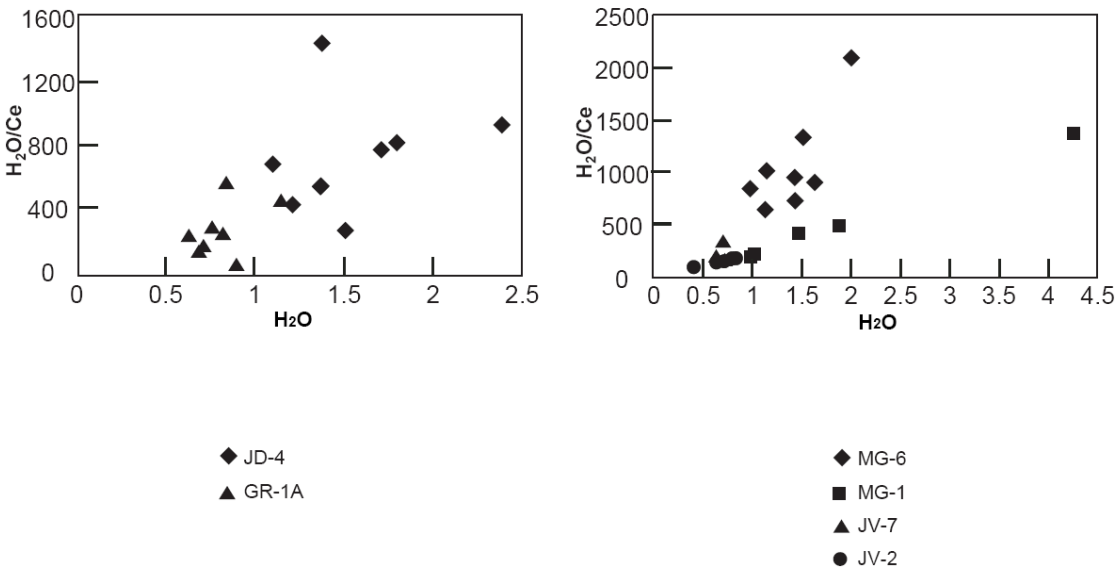

Figure 3.12. Plots of H_20/Ce vs. water for main-eruptive-stage (left) and late-eruptive-stage melt inclusions. The slope shown provides further evidence that degassing and not enrichment is the most important process occurring during the magmatic evolution.

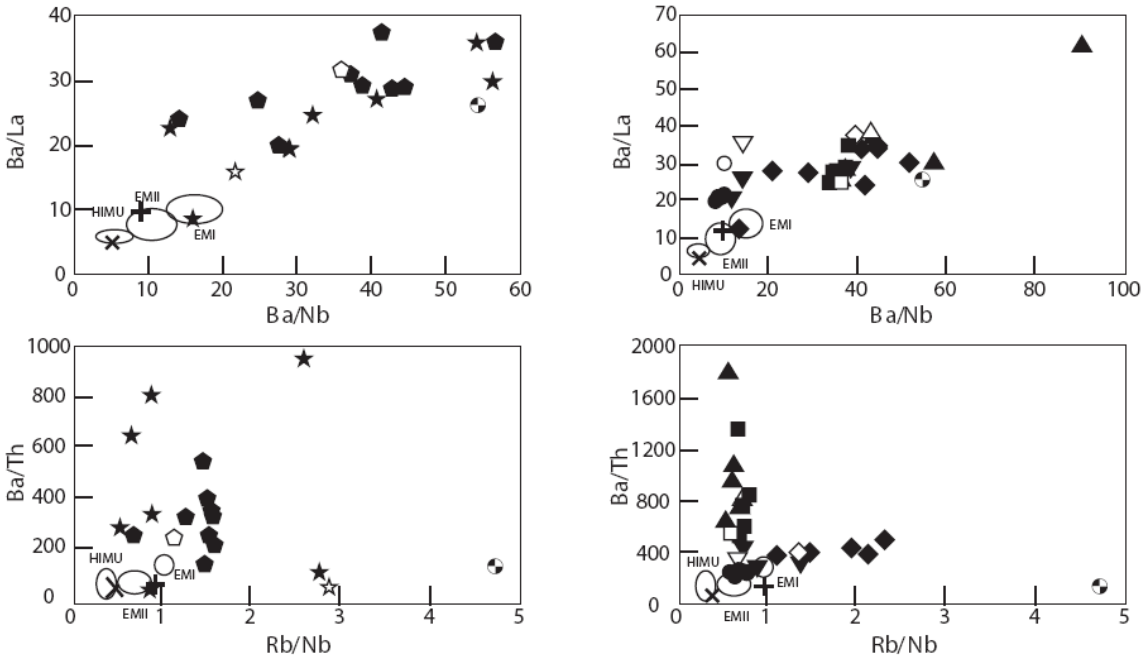

Figure 3.13. Plots of Ba/La versus Ba/Nb and Ba/Th versus Rb/Nb for main-eruptive-stage melt inclusions and host rocks (left) and late-eruptive-stage melt inclusions and their host rocks (right). Also included are estimated compositions for primordial mantle, N-MORB, continental crust (from Weaver 1991). The fields for the mantle end members are from Weaver (1991). Note that many inclusions plot away from the fields denoted by the mantle end members, instead exhibiting compositions normally seen in arcs.

References

Brandon, A. D., P. R. Hooper, et al. (1993). "Evaluating Crustal Contamination in Continental Basalts - the Isotopic Composition of the Picture Gorge Basalt of the Columbia River Basalt Group." Contributions to Mineralogy and Petrology 114(4): 452-464.

Brueseke, M. E., M. T. Heizler, et al. (2007). "Distribution and geochronology of Oregon Plateau (USA) flood basalt volcanism: The Steens Basalt revisited." Journal of Volcanology and Geothermal Research 161(3): 187-214.

Camp, V. E. (1995). "Mid-Miocene propagation of the Yellowstone mantle plume head beneath the Columbia River Basalt source region." Geology 23(5): 435-438.

Camp, V. E. and M. E. Ross (2004). "Mantle dynamics and genesis of mafic magmatism in the intermontane Pacific Northwest." Journal of Geophysical Research-Solid Earth 109(B8).

Camp, V. E., M. E. Ross, et al. (2003). "Genesis of flood basalts and Basin and Range volcanic rocks from Steens Mountain to the Malheur River gorge, Oregon." Geological Society of America Bulletin 115(1): 105-128.

Carlson, R. W. (1984). "Isotopic Constraints on Columbia River Flood-Basalt Genesis and the Nature of the Subcontinental Mantle." Geochimica Et Cosmochimica Acta 48(11): 2357-2372.

Chen, Y. and Y. Zhang (2008). "Olivine dissolution in basaltic melt." Geochimica et Cosmochimica Acta 72(19): 4756-4777.

Churikova, T., G. Worner, et al. (2007). "Volatile (S, Cl and F) and fluid mobile trace element compositions in melt inclusions: implications for variable fluid sources across the Kamchatka arc." Contributions to Mineralogy and Petrology 154(2): 217-239.

Danyushevsky, L. V., A. W. McNeill, et al. (2002). "Experimental and petrological studies of melt inclusions in phenocrysts from mantle-derived magmas: an overview of techniques, advantages and complications." Chemical Geology 183(1-4): 5-24.

Demouchy, S. and S. Mackwell (2003). "Water diffusion in synthetic iron-free forsterite." Physics and Chemistry of Minerals 30(8): 486-494.

Dixon, J. E., E. M. Stolper, et al. (1995). "An experimental study of water and carbon dioxide solubilities in mid ocean ridge basaltic liquids .1. Calibration and solubility models." Journal of Petrology 36(6): 1607-1631.

Dodson, A., B. M. Kennedy, et al. (1997). "Helium and neon isotopes in the Imnaha Basalt, Columbia River Basalt Group; evidence for a Yellowstone plume source." Earth and Planetary Science Letters 150(3-4): 443-451.

Feeley, T. C. (2003). "Origin and tectonic implications of across-strike geochemical variations in the Eocene Absaroka volcanic province, United States." Journal of Geology 111(3): 329-346.

Geist, D. and M. Richards (1993). "Origin of the Columbia Plateau and Snake River plain; deflection of the Yellowstone plume." Geology 21(9): 789-792.

Hales, T. C., D. L. Abt, et al. (2005). "A lithospheric instability origin for Columbia River flood basalts and Wallowa Mountains uplift in northeast Oregon." Nature 438(7069): 842-845.

Hauri, E. (2002). "SIMS analysis of volatiles in silicate glasses, 2: isotopes and abundances in Hawaiian melt inclusions." Chemical Geology 183(1-4): 115-141.

Hooper, P. R., G. B. Binger, et al. (2002). "Ages of the Steens and Columbia River flood basalts and their relationship to extension-related calc-alkalic volcanism in eastern Oregon." Geological Society of America Bulletin 114(1): 43-50.

Hooper, P. R. and C. J. Hawkesworth (1993). "Isotopic and Geochemical Constraints on the Origin and Evolution of the Columbia River Basalt." Journal of Petrology 34(6): 1203-1246.

Johnson D.M., H. P. R., and Conrey, R.M. (1999). "GeoAnalytical Lab, Washington State University." Advances in X-ray Analysis vol 41: 843-867.

Johnson, E. R., P. J. Wallace, et al. (2008). "Magmatic volatile contents and degassing-induced crystallization at Volcan Jorullo, Mexico: Implications for melt evolution and the plumbing systems of monogenetic volcanoes." Earth and Planetary Science Letters 269(3-4): 477-486.

Jordan, M., R. B. Smith, et al. "The Yellowstone Hotspot and related plume; volcano-tectonics, tomography, kinematics, dynamics and mantle flow."

Kamenetsky, V. S. and A. A. Gurenko (2007). "Cryptic crustal contamination of MORB primitive melts recorded in olivine-hosted glass and mineral inclusions." Contributions to Mineralogy and Petrology 153(4): 465-481.

Kent, A. J. R., E. M. Stolper, et al. (2004). "Mantle heterogeneity during the formation of the North Atlantic Igneous Province: Constraints from trace element and Sr-Nd-Os-O isotope systematics of Baffin Island picrites." Geochemistry Geophysics Geosystems 5.

Knaack, C., Cornelius, S., Hooper, P.R. (1994). "TRACE ELEMENT ANALYSIS OF ROCKS AND MINERALS BY ICP-MS." Open File Report, Department of Geology, Washington State University.

Kress, V. C. and M. S. Ghiorso (1995). "Multicomponent diffusion in basaltic melts." Geochimica et Cosmochimica Acta 59(2): 313-324.

Lange, R. A. (2002). "Constraints on the preeruptive volatile concentrations in the Columbia River flood basalts." Geology 30(2): 179-182.

Leeman, W. P. and C. J. Vitaliano (1976). "Petrology of McKinney Basalt, Snake River Plain, Idaho." Geological Society of America Bulletin 87(12): 1777-1792.

Leeman, W. P., J. S. Oldow, et al. (1992). "Lithosphere-Scale Thrusting in the Western United-States Cordillera as Constrained by Sr and Nd Isotopic Transitions in Neogene Volcanic-Rocks." Geology 20(1): 63-66.

Luhr, J. F. (2001). "Glass inclusions and melt volatile contents at Paricutin Volcano, Mexico." Contributions to Mineralogy and Petrology 142(3): 261-283.

Mangan, M. T., T. L. Wright, et al. (1986). "Regional Correlation of Grande-Ronde Basalt Flows, Columbia River Basalt Group, Washington, Oregon, and Idaho." Geological Society of America Bulletin 97(11): 1300-1318.

Moore, G., T. Vennemann, et al. (1998). "An empirical model for the solubility of H2O in magmas to 3 kilobars." American Mineralogist 83(1-2): 36-42.

Moune, S., O. Sigmarsson, et al. (2007). "Recent volatile evolution in the magmatic system of Hekla volcano, Iceland." Earth and Planetary Science Letters 255(3-4): 373-389.

Portnyagin, M., R. Almeev, et al. (2008). "Experimental evidence for rapid water exchange between melt inclusions in olivine and host magma." Earth and Planetary Science Letters 272(3-4): 541-552.

Portnyagin, M., K. Hoernle, et al. (2007). "Constraints on mantle melting and composition and nature of slab components in volcanic arcs from volatiles (H2O, S, Cl, F) and trace elements in melt inclusions from the Kamchatka Arc." Earth and Planetary Science Letters 255(1-2): 53-69.

Ramos, F. C., J. A. Wolff, et al. (2005). "Sr isotope disequilibrium in Columbia River flood basalts; evidence for rapid shallow-level open-system processes." Geology 33(6): 457-460.

Reidel, S. P. (1983). "Stratigraphy and Petrogenesis of the Grande-Ronde-Basalt from the Deep Canyon Country of Washington, Oregon, and Idaho." Geological Society of America Bulletin 94(4): 519-542.

Sadofsky, S. J., M. Portnyagin, et al. (2008). "Subduction cycling of volatiles and trace elements through the Central American volcanic arc: evidence from melt inclusions." Contributions to Mineralogy and Petrology 155(4): 433-456.

Schiano, P., R. Clocchiatti, et al. (2004). "The nature of melt inclusions inside minerals in an ultramafic cumulate from Adak volcanic center, aleutian arc: implications for the origin of high-Al basalts." Chemical Geology 203(1-2): 169-179.

Severs, M. J., T. Azbej, et al. (2007). "Experimental determination of H2O loss from melt inclusions during laboratory heating: Evidence from Raman spectroscopy." Chemical Geology 237(3-4): 358-371.

Sobolev, A. V. and L. V. Danyushevsky (1994). "Petrology and Geochemistry of Boninites from the North Termination of the Tonga Trench - Constraints on the Generation Conditions of Primary High-Ca Boninite Magmas." Journal of Petrology 35(5): 1183-1211.

Takahashi, E., K. Nakajima, et al. (1998). "Origin of the Columbia River basalts; melting model of a heterogeneous plume head." Earth and Planetary Science Letters 162(1-4): 63-80.

Toplis, M. J. (2005). "The thermodynamics of iron and magnesium partitioning between olivine and liquid: criteria for assessing and predicting equilibrium in natural and experimental systems." Contributions to Mineralogy and Petrology 149(1): 22-39.

Vigouroux, N., P. J. Wallace, et al. (2008). "Volatiles in high-K magmas from the western Trans-Mexican volcanic belt: Evidence for fluid fluxing and extreme enrichment of the mantle wedge by subduction processes." Journal of Petrology 49(9): 1589-1618.

Walker, J. A., K. Roggensack, et al. (2003). "The water and trace element contents of melt inclusions across an active subduction zone." Contributions to Mineralogy and Petrology 146(1): 62-77.

Wallace, P., E. Johnson, et al. (2007). Ascent, degassing, crystallization and eruption of H2O-rich mafic arc magma: A melt inclusion perspective. 17th Annual V M Goldschmidt Conference, Cologne, GERMANY.

Wallace, P. J. (2005). "Volatiles in subduction zone magmas: concentrations and fluxes based on melt inclusion and volcanic gas data." Journal of Volcanology and Geothermal Research 140(1-3): 217-240.

Weaver, B. L. (1991). "The Origin of Ocean Island Basalt End-Member Compositions - Trace-Element and Isotopic Constraints." Earth and Planetary Science Letters 104(2-4): 381-397.

Yuan, H. Y. and K. Dueker (2005). "Teleseismic P-wave tomogram of the Yellowstone plume." Geophysical Research Letters 32(7).

Zhang, Y. X. and E. M. Stolper (1991). "Water Diffusion in a Basaltic Melt." Nature 351(6324): 306-309.

TABLE 3.1. Samples Analyzed

	Main stage		Late				
Sample #	JD-4	GR-1A	MG-1	MG-4	MG-6	JV-2	JV-7
age (Ma)	16	~15	8	12	0.1	<0.1	0.2
setting	Monument dike swarm along John Day River, OR	Chief Joseph Dike Swarm along Grande Ronde River,	Lava flow Malheur Gorge, OR	Lava flow Bottom of Malheur Gorge, OR	Lava flow Top of Malheur Gorge, OR	Lava flow from Jordan Craters, OR	Lava flow in Jordan Valley, OR
SiO_2	51.62	54.18	48.58	49.48	48.92	49.34	48.33
TiO_2	1.45	2.098	2.061	2.210	0.908	2.090	2.341
Al_2O_3	16.48	14.08	16.11	16.07	16.84	16.86	16.65
FeO	10.42	11.62	11.36	11.83	9.46	9.96	10.27
MnO	0.18	0.185	0.194	0.195	0.170	0.162	0.159
MgO	5.06	4.83	7.57	6.52	9.53	7.40	8.25
CaO	11.02	8.52	10.42	9.31	11.18	9.41	9.80
Na_2O	2.98	2.66	2.67	3.01	2.62	3.26	3.26
K_2O	0.63	1.60	0.74	0.81	0.28	1.24	0.73
P_2O_5	0.17	0.226	0.296	0.558	0.079	0.274	0.215
Rb	7.5	53.4	7.4	9	4	24.3	11.5
Sr	251	227	249	415	205	535	662
Y	27.93	34.73	27.66	32.67	16.08	17.36	16.29
Zr	107	203	171	167	60	154	117
Nb	7.16	18.93	11.62	16.75	3.15	39.03	19.74
Ba	251	402	483	595	120	362	254
La	8.16	25.99	12.82	24.87	3.34	12.5	7.52
Ce	17.95	52.34	27.55	53.8	8.18	26.81	17.87
Pr	2.49	6.42	3.91	7.19	1.25	3.55	2.66
Nd	11.58	25.86	17.91	30.77	6.1	15.26	12.94
Sm	3.49	6.15	4.64	7.2	1.91	3.71	3.61
Eu	1.37	1.99	1.91	2.39	0.87	1.51	1.54
Gd	4.33	6.44	5.07	7.03	2.44	3.72	3.69
Dy	5.23	6.89	5.42	6.69	3.04	3.61	3.42
Er	3.07	3.83	3.09	3.5	1.84	1.92	1.74
Yb	2.8	3.34	2.74	3.03	1.78	1.76	1.54
Th	1.06	6.94	0.61	1.14	0.34	1.68	0.84
U	0.43	1.66	0.21	0.37	0.12	0.5	0.29

Host rock sample numbers with descriptions and major and trace element chemistry

TABLE 3.2. Major oxide, trace element and volatile compositions of Olivine and Plagioclase hosted melt inclusions

Main Stage	GR-1a-2	GR-1a-5a	GR-1a-5b	GR-1a-5c	GR-1a-6	GR-1a-6a	GR-1a-7	GR-1a-8	GR-1a-8a	GR-1a-9	GR-1a-10	GR-1a-10a
SiO_2	46.97	50.89	49.87	51.42	48.15	49.97	48.04	52.72	54.07	55.56	50.03	50.21
TiO_2	1.89	1.32	1.15	1.10	0.90	0.92	1.03	0.59	1.24	0.74	1.09	0.96
Al_2O_3	9.51	20.15	22.75	22.59	24.95	24.62	24.68	23.94	23.03	22.87	22.85	23.43
FeO	11.68	6.78	5.78	5.43	5.19	4.62	5.48	4.03	4.65	3.91	5.61	5.46
MnO	0.27	0.09	0.07	0.10	0.14	0.09	0.09	0.06	0.08	0.04	0.09	0.10
MgO	12.17	4.44	3.99	3.59	3.21	2.76	2.92	1.74	0.57	0.26	3.91	3.64
CaO	10.36	11.65	12.10	11.54	12.35	11.40	12.54	10.36	9.54	8.75	11.96	11.32
Na_2O	5.59	3.15	2.78	2.66	3.39	3.64	3.67	4.64	4.60	5.01	2.91	3.19
K_2O	0.50	0.43	0.56	0.57	0.69	1.04	0.61	1.04	1.37	1.79	0.57	0.84
P_2O_5	0.39	0.49	0.29	0.35	0.22	0.13	0.25	0.10	0.21	0.20	0.39	0.25
H_2O	0.69	0.61	0.66	0.65	0.81	0.80	0.68	0.79	0.63	0.87	0.60	0.60
plag AN		89.08	89.08	89.08	88.64	88.64	85.56	80.71	80.71	78.20	87.06	87.06
F					113.22			383.10		569.05		
S					75.01			493.17		235.70		
Cl					662.64			94.87		102.14		
Sc				12.87			10.98	12.02		11.76	10.30	
Rb				7.83	2.96		9.81	23.91		28.33	7.18	
Sr				334.43	341.56		360.62	356.24		383.19	332.99	
Y				17.85	4.43		17.35	13.34		51.25	10.40	
Zr				98.86	27.49		91.25	72.20		249.08	58.53	
Nb				12.95	3.26		11.72	8.82		34.93	8.67	
Ba				369.95	182.23		333.41	354.92		542.15	274.19	
La				19.49	6.19		17.46	13.28		66.12	11.31	
Ce				48.32	14.55		40.15	32.33		160.24	25.76	
Pr				5.20	1.59		4.58	3.57		17.89	3.35	
Nd				19.70	6.53		17.14	14.82		72.21	9.99	
Sm				4.15	1.48		3.74	3.18		11.05	2.31	
Eu				1.71	0.67		1.62	1.30		3.36	0.79	
Gd				5.68			3.56	2.46		11.42	2.10	
Dy				2.50	0.96		2.90	2.83		8.73	1.61	
Er				1.26			2.05	1.60		6.41	1.10	
Yb				1.99			1.93	0.93		5.08	0.69	
Th				0.56			0.97	2.93		11.37	0.32	
U				0.21			0.35	0.89		4.46	0.09	

Major element, trace element and volatile concentrations. Major oxides and H_2O are given in wt%, trace elements and other volatiles in ppm

TABLE 3.2 cont.

Main Stage	GR-1a-11	GR-1a-12	GR-1a-12a Main Stage	GR-1a-1	JD-4-1a	JD-4-1b	JD-4-2	JD-4-3	JD-4-4	JD-4-5	JD-4-6
SiO_2	50.67	48.50	48.64 SiO_2	41.81	51.28	53.26	47.91	50.07	50.99	53.03	52.70
TiO_2	0.08	0.03	0.05 TiO_2	2.49	1.37	1.78	0.82	1.17	1.59	1.38	1.52
Al_2O_3	30.14	31.97	31.85 Al_2O_3	12.31	14.61	15.77	13.89	12.61	15.13	16.23	15.83
FeO	0.68	0.42	0.51 FeO	18.53	8.02	8.05	17.33	12.63	9.95	7.44	9.49
MnO	0.01	0.02	0.00 MnO	0.36	0.30	0.21	0.38	0.23	0.19	0.05	0.16
MgO	0.17	0.20	0.20 MgO	12.12	3.42	4.16	9.05	5.94	4.99	3.96	3.91
CaO	13.12	15.25	15.12 CaO	7.17	15.15	11.84	7.33	9.33	11.93	12.46	11.29
Na_2O	4.19	2.90	2.86 Na_2O	3.36	3.26	3.53	2.17	5.92	3.18	3.11	3.28
K_2O	0.33	0.18	0.19 K_2O	0.39	0.55	0.53	0.15	0.69	0.58	0.59	0.60
P_2O_5	0.00	0.04	0.09 P_2O_5	0.34	0.07	0.31	0.01	0.09	0.03	0.00	0.16
H_2O	0.63	0.73	0.50 H_2O	1.12	2.35	1.47	1.34	1.33	1.44	1.76	1.06
plag AN	78.91	88.51	88.51 olivine Fo	84.56	80.68	80.68	79.61			81.47	77.35
F		984.98	F	404.46	310.16	330.89	327.45	2605.70			669.09
S		420.47	S	209.05	717.31	509.70	510.94	1631.61			650.44
Cl		159.04	Cl	204.45	76.76	125.36	71.09	54.41			203.13
Sc		14.87	Sc	12.87	51.13	12.32	20.10	34.05		53.84	28.01
Rb		18.69	Rb	7.54	10.72	41.38	3.82	10.97		8.24	7.99
Sr		409.05	Sr	174.42	299.06	541.39	107.75	628.33		283.69	203.57
Y		10.56	Y	13.06	37.30	28.77	13.42	19.81		39.33	17.40
Zr		64.87	Zr	97.31	133.08	163.58	47.87	112.54		125.75	73.95
Nb		7.36	Nb	15.80	7.37	29.43	2.58	17.97		5.94	5.27
Ba		395.39	Ba	197.01	310.22	707.34	112.93	242.04		332.67	141.40
La		11.15	La	8.86	11.05	26.97	3.99	10.36		9.43	7.33
Ce		25.74	Ce	25.00	26.48	60.92	9.64	25.93		22.60	16.39
Pr		2.85	Pr	2.68	3.40	7.60	1.33	3.03		3.04	1.90
Nd		12.04	Nd	11.41	16.43	29.55	5.79	18.34		15.51	10.26
Sm		3.02	Sm	2.27	4.23	6.84	2.13	3.98		6.19	3.57
Eu		0.64	Eu	0.80	1.64	3.43	0.82	1.52		1.92	1.49
Gd		2.41	Gd	2.53	5.54	5.96	2.27	5.51		5.64	3.25
Dy		2.13	Dy	2.46	7.38	4.26	2.90	3.53		8.37	3.73
Er		1.49	Er	1.08	5.06	3.04	1.37	1.53		4.37	1.42
Yb			Yb	1.34	4.06	1.70	1.31	2.30		5.60	1.77
Th		0.43	Th	0.67	1.21	5.07	0.33	0.97		0.62	0.61
U		0.36	U	0.12	0.54	1.63	0.15				0.23

Major element, trace element and volatile concentrations. Major oxides and H_2O are given in wt%, trace elements and other volatiles in ppm

TABLE 3.2 cont.

Main Stage	JD-4-7	JD-4-8	JD-4-10	JD-4-11	Late	Mg-6-1	MG-6-3	Mg-6-4	mg-6-5	Mg-6-6	Mg-6-7	MG-6-8
SiO_2	50.28	49.27	52.29	52.51		49.34	47.06	46.82	47.70	47.93	44.47	46.35
TiO_2	1.57	1.92	1.49	1.73		1.13	1.02	1.09	0.80	0.87	1.09	1.00
Al_2O_3	13.84	12.23	15.69	16.69		13.78	18.38	16.16	15.46	14.98	11.98	15.04
FeO	13.43	14.63	17.40	7.65		11.91	7.68	10.33	10.05	11.33	11.60	14.59
MnO	0.24	0.28	0.16	0.10		0.18	0.17	0.12	0.12	0.27	0.23	0.29
MgO	5.50	6.36	5.48	2.80		10.86	5.81	9.47	9.52	10.45	10.39	10.97
CaO	10.36	10.26	11.58	13.27		7.48	15.08	10.32	11.20	9.49	14.47	6.96
Na_2O	2.93	2.63	3.20	3.52		3.61	2.85	3.75	2.67	3.27	3.83	3.29
K_2O	0.52	0.54	0.57	0.58		0.60	0.34	0.45	0.39	0.41	0.47	0.50
P_2O_5	0.13	0.21	0.07	0.00		0.03	0.02	0.10	0.14	0.06	0.07	0.04
H_2O	1.20	1.67	1.33	1.17		1.09	1.59	1.39	1.96	0.93	1.39	1.10
olivine Fo	76.33		79.03			86.50	84.71	86.51	87.02	86.51	86.25	84.73
F			0.00	74.72						107.06		119.51
S			2.58	170.81						23.35		104.44
Cl			6.75	33.74						40.32		52.85
Sc		35.50	36.97	36.97		31.22	29.64	23.88	28.65	31.08	37.04	25.47
Rb		8.03	12.03	12.16		11.20	5.06	6.04	9.49	4.23	6.54	7.08
Sr		230.54	256.85	296.53		180.31	286.06	164.80	167.49	170.42	230.68	178.58
Y		27.98	30.01	34.49		21.82	46.07	24.14	16.91	15.43	33.26	17.34
Zr		104.34	105.63	116.11		97.25	66.72	91.70	73.93	54.78	68.03	72.11
Nb		6.72	8.03	8.47		5.01	3.63	5.90	3.71	2.89	3.19	3.81
Ba		256.14	293.10	344.85		197.88	146.05	70.81	72.39	124.33	160.27	164.07
La		8.98	9.69	9.39		6.15	6.53	6.71	2.76	3.85	5.63	4.97
Ce		22.71	26.04	29.33		18.11	18.48	20.31	9.60	11.68	15.31	11.37
Pr		3.10	2.89	3.49		2.32	2.31	2.77	1.32	1.62	2.06	1.42
Nd		15.79	13.71	16.66		10.89	10.39	13.47	7.10	8.42	10.28	6.74
Sm		5.53	5.40	4.55		3.50	3.02	3.07	1.79	1.51	2.96	2.23
Eu		1.83	1.29	1.54		1.07	1.47	1.08	0.70	0.64	1.34	0.95
Gd		6.23	2.79	4.84		3.39	4.34	3.18	2.18	2.39	3.74	2.89
Dy		5.11	5.80	5.52		3.81	5.88	5.01	1.84	3.96	4.36	2.81
Er		3.23	3.15	3.59		2.29	4.76	2.44	1.30	1.75	3.73	1.87
Yb		2.60	2.48	3.63		2.55	4.64	2.69	1.75	1.40	4.19	1.74
Th		0.78	0.90	0.83		0.43	0.42	0.20			0.48	0.43
U		0.45	0.56	0.49		0.18	0.96	0.14	0.12		1.95	

Major element, trace element and volatile concentrations. Major oxides and H_2O are given in wt%, trace elements and other volatiles in ppm

TABLE 3.2 cont.

Late	MG-6-9	MG-6-10	MG-1-2	MG-1-3	MG-1-5	MG-1-6	MG-1-7	MG-1-8	MG-1-9	MG-4-1	MG-4-2	MG-4-3
SiO_2	46.45	46.34	44.05	43.16	46.40	41.58	49.91	45.27	43.97	49.58	50.09	49.22
TiO_2	0.72	0.94	2.34	2.21	1.75	1.15	2.50	1.89	2.66	2.20	2.09	2.36
Al_2O_3	14.82	17.39	12.86	12.32	15.20	15.11	16.94	11.14	10.09	16.57	16.08	18.16
FeO	14.02	10.12	15.22	14.55	13.84	16.74	8.33	15.06	19.05	11.32	11.19	9.66
MnO	0.25	0.16	0.23	0.22	0.25	0.28	0.10	0.22	0.33	0.27	0.22	0.32
MgO	10.49	8.86	7.62	9.33	8.90	10.91	4.99	10.14	9.48	5.11	5.25	4.17
CaO	8.53	11.95	11.55	11.80	8.03	9.59	12.07	10.48	9.37	9.89	10.01	10.14
Na_2O	2.70	2.30	1.98	1.73	3.04	2.07	2.93	4.46	2.79	3.14	3.01	3.42
K_2O	0.49	0.36	0.58	0.49	0.76	0.46	0.87	0.27	0.46	0.98	1.02	1.09
P_2O_5	0.04	0.10	0.20	0.30	0.43	0.26	0.35	0.22	0.84	0.16	0.08	0.65
H_2O	1.49	1.47	3.37	4.24	1.45	1.86	1.00	1.23	0.97	0.80	0.95	0.80
olivine Fo	83.91	86.41	79.17		82.06			82.12	81.39			
F	114.39	152.23	553.94	720.94	643.26		408.47	526.09				
S	423.54	503.80	2715.03	2854.41	390.41		587.78	1454.32				
Cl	90.49	35.17	193.57	113.09	106.53		61.33	292.00				
Sc		29.47		28.96	16.36	14.31	43.66		34.64		25.93	
Rb		6.91		4.17	7.39	5.33	9.54		8.55		15.38	
Sr		181.83		241.65	247.11	278.56	292.64		290.39		446.69	
Y		19.25		31.30	28.09	29.55	41.38		46.80		31.50	
Zr		105.07		188.24	167.18	162.90	245.23		248.68		163.92	
Nb		3.67		9.29	13.70	10.22	15.70		17.87		20.65	
Ba		101.11		323.60	576.02	569.20	562.77		1588.14		754.26	
La		3.93		13.08	15.89	19.34	20.31		26.01		26.95	
Ce		11.43		31.37	36.44	39.80	48.86		55.34		75.25	
Pr		1.58		4.40	4.39	5.16	6.12		7.27		8.54	
Nd		7.20		22.48	19.54	21.48	28.20		29.38		34.19	
Sm		2.73		5.83	4.23	4.82	6.92		6.92		8.76	
Eu		1.00		1.92	1.80	1.52	2.56		2.12		2.64	
Gd		2.72		5.47	3.91	5.18	6.80		9.17		8.30	
Dy		3.74		5.86	4.08	4.41	6.07		7.43		6.28	
Er		2.24		3.36	2.77	2.24	5.15		3.69		2.85	
Yb		3.38		3.94	2.60	2.66	3.17		3.04		2.72	
Th				0.52	0.55	0.62	0.78		0.92		0.92	
U		0.15		0.17	0.27	0.28	0.38		0.36		0.49	

Major element, trace element and volatile concentrations. Major oxides and H_2O are given in wt%, trace elements and other volatiles in ppm

TABLE 3.2 cont.

Late	MG-4-4	MG-4-5	MG-4-8	MG-4-9	MG-4-11	MG-4-12	JV-7-1	JV-7-2	JV-7-4	JV-7-5	JV-7-6	JV-7-7
SiO_2	49.67	48.97	45.26	46.55	47.50	47.77	43.71	45.71	47.02	47.32	47.41	45.22
TiO_2	2.13	2.15	2.04	2.13	2.07	1.25	3.29	2.62	2.39	2.32	2.51	3.58
Al_2O_3	16.47	17.75	15.23	16.23	17.01	7.03	12.08	13.29	17.10	18.21	18.48	8.92
FeO	11.11	10.56	15.82	13.90	13.00	20.86	14.24	12.77	9.78	8.65	8.03	15.13
MnO	0.22	0.21	0.21	0.18	0.22	0.35	0.31	0.25	0.18	0.12	0.17	0.24
MgO	5.39	4.36	7.45	6.23	6.19	7.98	11.44	10.48	8.08	6.86	6.19	11.28
CaO	9.67	10.18	9.16	9.25	8.28	7.02	7.58	8.50	10.43	11.07	10.87	8.87
Na_2O	3.09	3.33	2.66	3.10	3.50	5.22	4.69	4.48	3.33	3.59	4.47	4.05
K_2O	1.10	1.10	0.85	0.98	1.02	0.61	0.96	0.82	0.78	0.78	0.78	1.35
P_2O_5	0.00	0.25	0.43	0.54	0.52	0.62	0.76	0.40	0.37	0.39	0.51	0.64
H_2O	1.16	1.15	0.89	0.91	0.68	1.29	0.95	0.68	0.55	0.67	0.60	0.73
olivine Fo								85.56		84.88	85.19	
F									497.81			
S									1106.89	121.71		
Cl									379.06	16.16		
Sc	31.93		25.80	25.89		21.31		32.71		36.91	23.90	
Rb	14.12		13.18	12.96		3.84		25.60		8.88	14.75	
Sr	443.24		416.03	452.39		146.45		479.01		237.37	741.40	
Y	35.10		29.35	31.75		18.48		26.67		29.07	18.39	
Zr	178.59		149.72	159.05		106.67		152.52		110.25	108.77	
Nb	20.46		19.60	20.44		6.22		31.81		6.89	22.76	
Ba	705.96		658.69	671.93		230.85		329.82		255.18	291.53	
La	26.12		24.64	28.15		6.81		17.52		9.44	12.05	
Ce	69.30		66.48	73.70		19.28		47.03		20.76	33.17	
Pr	7.72		7.55	8.55		2.69		6.12		2.99	4.10	
Nd	34.45		28.31	34.21		12.56		26.67		13.10	16.08	
Sm	7.67		5.35	7.40		3.51		6.32		4.03	3.72	
Eu	2.58		1.99	2.36		1.01		1.98		1.58	1.94	
Gd	6.89		6.24	6.94		4.69		6.61		4.99	4.91	
Dy	5.70		5.60	5.96		3.28		4.83		5.64	3.58	
Er	3.29		2.65	2.61		2.28		2.62		3.37	1.35	
Yb	3.04		2.34	2.61		2.13		2.76		3.32	2.20	
Th	1.24		0.89	1.33		0.17		1.40		0.95	0.76	
U	0.33		0.35	0.35		0.21		0.75		0.38	0.25	

Major element, trace element and volatile concentrations. Major oxides and H_2O are given in wt%, trace elements and other volatiles in ppm

Chapter 4

Systematics of Sr, Nd and Hf isotopes in the Yellowstone hotspot and Columbia River Flood Basalts

Abstract

The Yellowstone hotspot track is the most accessible and most well studied feature of its kind on the continents. Its 16-m.y.history began with eruption of the voluminous Columbia River basalts (CRB) and continued with the bimodal rhyolite and basaltic eruptive centers which characterize the Snake River Plain (SRP). New bulk-rock Sr, Nd and Hf isotopic data are presented here to add to the understanding of the nature of basaltic volcanism throughout the Yellowstone hotspot track. Isotopic compositions for all three elements span most of the range of compositions observed in mantle-derived basalts worldwide. ε_{Hf} values vary in concert with ε_{Nd} and $^{87}Sr/^{86}Sr$ across the region from west to east. ε_{Hf} varies from +11.3 in parts of the CRB to as low as -8.3 in some of the late basalts of the SRP. This pattern is consistent with a crustal control of the isotopic compositions of Hf, Nd and Sr, in accordance with previous observations of silicic rocks in the region. Estimated crustal contribution to Nd and Hf isotopic composition is calculated for a suite of SRP basalts, indicating as much as a 45% crustal contribution for those elements. Also reported here are 16 new $^{40}Ar/^{39}Ar$ age

determinations for selected basalt samples and plagioclase separates throughout the region.

Introduction

Although study of hotspots has been essential to the construction of modern plate tectonic theory and the development of our understanding of the Earth's mantle, continental hotspots have generally received significantly less attention from geologists than their oceanic counterparts. This is largely due to the fact that penetration of continental crust tends to create complications that can make detailed interpretation of the source components difficult. However, the interaction between hotspots and continental crust may play a pivotal role in the local evolution of the crust. The Yellowstone hotspot represents one of the most well documented and well studied continental hotspot tracks in the world (Leeman et al., 1992; Christiansen, 2005; Nash et al. 2006). It penetrates North American continental lithosphere proximal to a convergent plate boundary with the Juan de Fuca Plate (cf. Manea et al., 2009). While some have expressed doubt about a mantle plume origin for the Yellowstone hotspot (e.g., Christiansen et al. 2002), many others have presented evidence suggestive of such an origin (e.g., Craig et al. 1978; Jordan et al. 2004; Nash et al. 2006). Several studies, as reviewed briefly immediately below, have explored the detailed petrogenetic processes in this tectonic setting deploying a large array of methods including petrology, geochemistry and seismology (cf. Humphreys et al., 2000; Waite et al., 2006; Leeman et al., 2008; Leeman et al., 2009; McCurry and Rodgers, 2009).

The Yellostone hotspot is characterized by bimodal volcanism, consisting of an initial phase of explosive rhyolitic eruptions which produce large calderas, followed by basaltic volcanism which buried the calderas (Leeman 1982; Christiansen 2005; Shervais et al. 2006). Initiation of the calderas was age transgressive from SW (McDermitt Caldera, ~16 Ma) to NE (Yellowstone Caldera, ~2 Ma), over a distance of 700 km, which corresponds to a North American Plate velocity of 3-4 cm per year, assuming a stationary plume conduit. This rate and trend approximate well the speed and direction of the North American Plate measured using other methods (Leeman, 1982; Pierce and Morgan, 1992) (Fig. 4.1).

Both basaltic and rhyolitic magmatism are interpreted to have commenced with the arrival of the plume head at the base of the lithosphere at ~17 Ma, triggering the eruption of the Columbia River Flood Basalts (Geist and Richards 1993; Camp 1995; Dodson et al. 1997; Camp and Ross, 2004). The observed track of Yellowstone-Snake River Plain (YSRP) rhyolitic calderas is commonly attributed to interaction of the plume tail with the westward migrating North American Plate. The rhyolitic volcanism is interpreted to be a result largely of crustal anatexis triggered by injection of basalts into the lower crust (Leeman, 1982; Carlson 1984; Hart, 1985; Bonnichsen et al., 2008; Leeman et al., 2008).

The presence of a low-velocity anomaly beneath Yellowstone extending to a depth of 500-600 km (Humphreys et al., 2000; Yuan & Dueker, 2005; Waite et al., 2006), has been interpreted as the manifestation of a rising plume elevated in

temperature relative to the ambient mantle. However, the presence of a thick lithospheric lid might prevent decompression melting of an ascending mantle plume (Manea et al., 2009). Because the YSRP province transects Basin and Range structures that are observed south and north of the SRP (Leeman 1982; Nash et al. 2006), it is conceivable that YSRP basaltic volcanism is at least partly a consequence of regional extension (cf. Harry and Leeman, 1995; Bonnichsen et al., 2008; Leeman et al., 2008) – perhaps abetted by an upwelling mantle plume (e.g., to account for the heat required to produce anomalous magmatic volumes). On the other hand, Leeman et al. (2009) note petrogenetic, geochemical, and seismic tomographic data that point to derivation of YSRP basalts from shallow (lithospheric mantle) sources that are not unusually hot, in which case the presence of relatively fertile or hydrated mantle sources might explain the voluminous melt productivity associated with this province. Volatile budgets from Stefano et al (2010a and b) suggest that at least some of the melt components are of lithospheric origin.

Elevated $^{3}He/^{4}He$ ratios, up to 16 R_A in YSRP basalts (Craig et al., 1978; Craig, 1993; Graham et al., 2009) implicate a sub-lithospheric source for this tracer. Furthermore, Nash et al. (2006) interpret Nd and Hf isotopic compositions of rhyolites in the province to be consistent with early inputs of magmatic components (i.e., basalt) derived from a mantle plume source. Based on these and other geochemical data, various investigators have argued that as much as 30-40% of the rhyolite volume could be of mantle derivation (i.e., via reprocessing of early underplated and crustally intruded basaltic magma; Leeman et al., 2008; McCurry and Rodgers, 2009). Thus, YSRP

basaltic magmatism appears to fundamentally drive the entire petrogenetic cycle from its beginning. This study focuses on Sr, Nd and Hf isotopes of basalts in the Yellowstone hotspot, and also considers new $^{40}Ar/^{39}Ar$ ages, and trace element and major oxide compositons of the basalts to provide further insights on petrogenesis.

Methods

1. Sample collection and preparation

Twelve basalt whole-rock samples were collected throughout the CRB-SRP region targeting a variety of eruption ages and chronologic relationship to the passing hypothesized mantle plume (i.e., early and late eruptive products in the CRB and syn-caldera and post-caldera eruptive products in the SRP). Samples were checked in the field for signs of weathering; weathered samples were avoided. Samples were then rough crushed using a jaw crusher; larger chips were picked out from the cores of the crushed pieces and thoroughly investigated under the binocular microscope to further avoid any weathering and saw cuts. Chips with no visible signs of secondary alterations were then washed with de-ionized water and dilute HCl. After drying, they were ground to a powder in a ceramic-walled shatter box for isotope analysis or further crushed by hand in an agate mortar to obtain 1-2 mm chips for $^{40}Ar/^{39}Ar$ dating.

2. Major oxide and trace element analysis

Major oxides and the trace elements Sr and Zr for the bulk rock lavas were analyzed by x-ray fluorescence (XRF) and trace elements were measured by LA-ICP-MS

at the XRF and ICP-HEX-MS Laboratories of the Washington State University Geoanalytical Laboratory following the methods of Knaack et al. (1994) and Johnson et al. (1999). Replicate analyses of samples and standards were reproducible within error.

3. Dissolution, column procedures and isotopic analyses

Isotopic ratios for Sr and Nd were determined on 100-mg rock powders dissolved in HF/HNO_3 acid solutions and then processed through elemental separations by column chromatographic methods described in Mukasa et al. (1991). Each sample was loaded on a Re filament and run on a multi-collector TIMS VG Sector at the University of Michigan. During the analytical work the average value for the La Jolla Nd isotope standard was $^{143}Nd/^{144}Nd = 0.511855 \pm 11$ (n = 4) (all errors are given as 2σ) using $^{146}Nd/^{144}Nd=0.7219$ for normalization. The Sr isotopic ratios were corrected for mass-fractionation using $^{86}Sr/^{88}Sr=0.1194$. Total blanks, averaging 0.33 ng for Sr and 0.21 ng for Nd, are negligible. The procedure for determining the Hf isotopic compositions involved dissolution of 120 mg of pulverized sample in concentrated, double-distilled HF mixed with a small amount of concentrated HNO_3. Hf was separated from the sample matrix using the Ln resin procedure of Münker et al. (2001) before being analyzed on a Nu Plasma HR MC-ICPMS at the University of Michigan. The JMC-475 standard yielded a mean value of $^{176}Hf/^{178}Hf = 0.282152 \pm 6$ (n = 6). The values we report here for the unknown samples were normalized to the JMC-475 accepted value of 0.282160. The total procedural blank level was less than 0.15 ng for Hf, which is negligible. Age

corrections on the basis of $^{40}Ar/^{39}Ar$ data presented in this paper were calculated for all samples, and were negligible.

4. $^{40}Ar/^{39}Ar$ analysis and dating

Samples for $^{40}Ar/^{39}Ar$ dating were crushed gently in an agate mortar, and the 0.8-1.0 mm sieve fraction was separated from the rest of the rock and washed in super de-ionized water. Approximately 30 mg whole-rock chips were packaged in duplicate for each sample in pure Al foil. The foil packets were then placed in evacuated quartz tubes, and irradiated in the research nuclear reactor at McMaster University in Ontario, Canada. Neutron flux variation (*J*) was measured using the standard mineral Fish Canyon Tuff biotite (split 3). The age used for this standard was calibrated earlier using the MMhb-1 hornblende standard. The error-weighed mean of five analyses vs. an age of 520.4 Ma for MMhb-1 was 27.99$\pm$0.04 Ma (2σ). This value is extremely close to the age of 28.02 Ma of the Fish Canyon Tuff sanidine (Renne et al., 1994). Subsequent to irradiation, the whole-rock chips were placed in 2mm-diameter wells of a copper disk and step-heated with increasing levels of laser power. Details about the $^{40}Ar/^{39}Ar$ analytical procedures followed at the University of Michigan are given in Hall and Farrell (1995).

Results

1. Major oxide and trace element compositions of Yellowstone hotspot lavas

Major oxide and trace element compositions are presented for Yellowstone hotspot lavas in TABLE 4.1. Trace element diagrams (Fig. 4.2) indicate sizable compositional heterogeneity throughout the region, but lavas from any one area tend to be very similar. The exception to this characteristic is the three basalt samples analyzed from the Malheur Gorge (MG prefix) in eastern Oregon (Fig. 4.1). These basalts erupted over a period of at least 10 My, and record some significant variation within that region. In general, many samples across the region show strong Ba enrichment. Fewer samples show significant enrichments of Sr, Nb and Zr. Rare earth element (REE) normalized to CI chondrite diagrams (Fig. 4.3) show that many samples, particularly those that erupted east of the 0.706 Sr line (Leeman et al., 1992), show significant light (L)REE enrichment, indicating relatively deep inception of melting or varying degrees of crustal interaction. The distribution of $^{87}Sr/^{86}Sr$ is controlled by the position of the erupting lava relative to the 0.706 Sr line; this delineates in the region the transition from thick cratonized crust in the east to thin accreted arc terranes in the west (Armstrong et al., 1977; Fleck and Criss, 1985; Leeman et al., 1992; Hanan et al., 2008). Some samples show small positive Eu anomalies, indicating plagioclase accumulation in their evolution; indeed most samples have abundant plagioclase phenocrysts in thin section.

2. Sr, Nd and Hf isotopic composition of Yellowstone hotspot lavas

Twenty samples of basaltic lavas from the Yellowstone hotspot track (CRB and SRP) were analyzed for $^{87}Sr/^{86}Sr$, $^{143}Nd/^{144}Nd$ and $^{176}Hf/^{177}Hf$ isotopic ratios (TABLE 4.2). $^{87}Sr/^{86}Sr$ ranged from 0.703415 ± 0.0011 in the Picture Gorge basalts to $0.707913 \pm$

0.0008 in late SRP basalts, covering most of the range of previously observed $^{87}Sr/^{86}Sr$ in the Yellowstone hotspot (Leeman and Manton, 1971; Brandon et al. 1993). ε_{Nd} values in our sample suite range from -5.9 in an SRP basalt to +6.08 in a sample of Picture Gorge basalt in the CRB. ε_{Hf} extend from -8.3 in a SRP basalt to +11.3 in a Picture Gorge basalt. Nd and Hf isotope ratios also seem to be sensitive to the type of crust that the lavas penetrated, and vary consistently with Sr in most cases. All isotopic ratios plot along the mantle array (Figs. 4.4 and 4.5), with Picture Gorge basalts consistently showing the most depleted compositions (i.e., least radiogenic Sr and most radiogenic Nd and Hf by virtue of time-integrated records in the source components of low Rb/Sr and high Sm/Nd and Lu/Hf, respectively). SRP basalts on the other hand have the most enriched isotopic compositions, with late CRB basalts in the middle. No strong isotopic differences were noted between syn-caldera and post-caldera SRP basalts.

3. $^{40}Ar/^{39}Ar$ dates of Yellowstone hotspot lavas

A subset of 13 of the Yellowstone hotspot whole-rock samples, and plagioclase phenocryst separates where available, were dated using the $^{40}Ar/^{39}Ar$ method in order to establish a time framework for the compositional differences observed throughout the region. Most samples have good agreement between total gas, plateau, and isochron ages (TABLE 4.3, Figs. 4.10-4.13). Total gas age always has to be used with caution because this approach is at the mercy of the possible presence of xenocrystic material and secondary alteration (Frey et al., 2004). In cases where there is agreement between plateau and isochron ages, there is no statistical basis to choose one over the

other. The data processing approach yielding the smaller error has been the one adopted in the discussions presented here.

Sample ages are generally in good agreement with expected values based on petrologic and stratigraphic correlation (Camp et al., 2003; Christiansen, 2005), although several of the very young samples yielded negative ages (zero with error). The exception was sample GR-1a, a basaltic dike from the Chief Joseph dike swarm along the Grande Ronde River. This sample was expected to yield an age near 16 Ma for main-stage CRB volcanism. Instead it yielded an age of 5.89 $\pm$ 0.18 (2σ) Ma from whole rock and 11.22 $\pm$ 0.56 Ma from plagioclase separates (Fig. 4.10). Because this sample comes from a dike, resetting is more likely due to outgassing of country rocks (Hyodo et al., 1993), and seems to be confirmed by the strong disagreement between whole rock and plagioclase dates.

Two flows from the top and bottom of a vertical exposure of Gerrit basalt (named in Christiansen, 2005) at Mesa Falls, Idaho, were analyzed in order to constrain the time interval over which the Gerrit basalt flows erupted (Fig. 4.12). The Mesa Falls section exposes seven flows, of which flows #2 and #7 (counting from the bottom) were dated. The only previous date on the Gerrit basalt was 0.199 $\pm$ 0.009 Ma by weighted average of several K-Ar analyses from Obradovich (1992). The $^{40}Ar/^{39}Ar$ isochron age for flow #2 was 0.157 $\pm$ 0.146Ma, which is indistinguishable within error from the Obradovich (1992) date. Flow #7 gave a $^{40}Ar/^{39}Ar$ plateau age of 0.076 $\pm$ 0.144 Ma, also indistinguishable within error from the date for flow #2 and the Obradovich (1992) date.

The large errors on the new $^{40}Ar/^{39}Ar$ dates result from the small sample size that can be analyzed by this method.

The three samples of Malheur Gorge basalts have yielded ages from 12.274 ± 0.112 Ma to 0.96 ± 0.114 Ma (Fig. 4.11). These are the first dates measured in this area, and mostly confirm expected ages of the lavas based on stratigraphy done there by Camp et al. (2003). Camp et al. (2003) mapped Steens Basalt at the bottom of the Malheur Gorge, which should yield a date near 16 Ma (Brueseke et al., 2007), however, our oldest sample (MG-4), collected at the bottom of the gorge yielded only 12.274± 0.112 Ma. Lavas in the Jordan Valley, Oregon, are also dated for the first time in this study and give ages between 0.161 ± 0.164 Ma and 0.015 ± 0.4 Ma, confirming the youthfulness of these lavas as suggested by Hart and Mertzman (1983) (Fig. 4.11).

Discussion

1. Spatial variation in Sr, Nd and Hf isotopes

Other workers have previously noted spatial control of Pb, Sr, and Nd in basaltic and rhyolitic rocks of the Yellowstone hotspot (e.g., Leeman et al., 1992; Nash et al., 2006; Savov et al., 2009). Nash et al. (2006) show that Hf isotopes are also spatially controlled in the rhyolitic rocks. These spatially controlled variations manifest as a change from more depleted compositions in the west ($^{87}Sr/^{86}Sr$ <0.704) to more enriched compositions in the east ($^{87}Sr/^{86}Sr$ >0.706), across the transition from thin accreted arc terranes to thick cratonized continental crust (Leeman et al. 1992). This strongly implicates crustal contamination as an important factor in the overall isotopic

composition profile of Yellowstone hotspot lavas. Fig. 4.6 shows that this previously recognized pattern also occurs in our new data, and confirms the same variation in Hf isotopes for basaltic lavas in the Yellowstone hotspot as observed in the coeval rhyolite lavas of the area by Nash et al. (2006).

ε_{Hf} values for Picture Gorge basalts at ~119.5º west are above +10, but at ~118 º -117º west values drop to -3. Basalts across the SRP vary between ~0 and -8, except for caldera filling Gerrit basalts at 111º west, on the eastern edge of the SRP, which vary from -1.5 to as high as +3. This observation of a widening isotopic range in the eastern part of the SRP is mirrored in the Sr and Nd isotopic compositions ($^{87}Sr/^{86}Sr$ from 0.70531 to 0.70755 and ε_{Nd} from -3.73 to -2.8) (Fig. 4.6), as has been previously observed by Nash et al. (2006) in Yellowstone hotspot rhyolites.

ε_{Hf} values for Picture Gorge basalts (+10.6 to +11.3) are comparable to values found by Nash et al. (2006) in rhyolites of similar age (~16 Ma) indicating that both magma types may have obtained their Hf from the same source. In contrast, there is a systematic offset between ε_{Hf} values in the SRP Basalts (0 to -8) and values found by Nash et al. (2006) in rhyolites of between -6 and -10, although there is significant overlap. This is similar to Nash et al.'s 2006 observation for Nd, with rhyolite ε_{Nd} clustering near -10, and basalt ε_{Nd} clustering near -6, which is also observed in this study. Because there is a contrast between Nd and Hf isotopic compositions for basalts and rhyolites in the SRP, it is possible that at least a component of the Nd and Hf in SRP basalts was derived from a sub-cratonic source, although it has been modified significantly en route to the surface by crustal interaction.

2. Sr, Nd and Hf isotopes in Picture Gorge basalts

Samples taken from dikes within the Monument Dike Swarm, a part of the Picture Gorge basalts in the CRB, contain the most primitive mantle-like isotopic compositions of the samples analyzed ($^{87}Sr/^{86}Sr$ from 0.7034 to 0.7036, ε_{Nd} from +5.9 to +6.1, ε_{Hf} from +10.6 to +11.3 Fig. 4.4 and 4.5). Their position atop accreted arc terranes suggests that they may have undergone less crustal influence than basalts of the SRP on the thicker craton. Brandon et al. (1993) conducted a study of Pb, Nd, Sr and O isotopes in the Picture Gorge basalts to evaluate the possible extent of crustal contamination concluding that their composition was best explained in terms of derivation from normal depleted mantle with components added from accreted arc terranes during crustal interaction. The results of the present study are consistent with those of the Brandon et al. (1993) study for Sr, showing a strong positive correlation between $^{87}Sr/^{86}Sr$ and Mg# of the analyzed dike (Fig. 4.7). Both ε_{Nd} and ε_{Hf} show very little variation in the selected dike samples, indicating that they are much less sensitive to crustal interaction than is Sr.

3. Sr, Nd and Hf isotopes in Gerrit basalts

In order to evaluate crustal interaction of SRP basalts in greater detail, five flows of Gerrit basalt from a single vertical section exposed at Mesa Falls, Idaho, were analyzed for their isotopic compositions. The 1st, 2nd, 4th, 6th, and 7th flows in the section, counting from the bottom of the exposure – all with indistinguishable $^{40}Ar/^{39}Ar$ ages – were sampled. Fig. 4.8 shows stratigraphic variations in the Sr, Nd and Hf isotopic compositions along with selected major and trace elements. The flows exhibit a smooth

change in Mg# from bottom to top, with flow #2 increasing from flow #1, and then a steady decline in the upper flows. Both ε_{Nd}, and ε_{Hf} trend in agreement with Mg#, with lower, more crustal-influenced values in the upper flows, supporting an interpretation of increased crustal interaction through time. Nd and Zr concentrations mirror the isotopic trends, indicating that the Nd and Hf isotopes are influenced by crustal inputs of these elements, including for example, digestion of accessory phases such as zircon.

In contrast, $^{87}Sr/^{86}Sr$ exhibits a steady increase up-section, except for an anomalously high point in flow #2, which otherwise would be characterized as having had the least amount of crustal interaction. Sr concentration tracks consistently with the other elements, and is also consistent with $^{87}Sr/^{86}Sr$ variation for all flows other than #2, and so does not provide any satisfactory explanation for this anomaly. It should be noted that flow #2 shows somewhat unusual composition in the considered parameters, and this behavior is not clearly understood yet. Contamination from a late alteration not entirely removed during sample processing cannot be ruled out for this sample.

The very consistent behavior of Mg#, selected trace elements and Sr, Nd and Hf isotopes in this section of Gerrit basalt makes a strong case for extensive crustal interaction of these basalts, whereas flow #2 most likely preserves the most primary mantle source-like Nd and Hf values.

In order to estimate the possible contribution of the crustal component, two-component mixing calculations were performed using MORB and continental crust as end members. MORB has [Hf]=3 ppm, ε_{Hf}= +15.55, [Nd]=11 ppm, ε_{Nd}= +11.179 (Hofmann, 1988) and may approximate a mantle melt derived beneath the SRP. The

continental crust in the area has ε_{Hf}=-25 to -50, [Hf]=4 ppm and ε_{Nd}=-20 to -50, [Nd]=22 ppm (Leeman et al., 1985, Vervoort et al., 1999, Rudnick and Gao, 2004). The wide variations in epsilon values are due to the existence of highly depleted Archean basement in part of the area characterized by very low ε_{Nd} and ε_{Hf} values (Leeman et al. 1985). Based on a simple linear mixing model, the minimum crustal contribution of Hf to the analyzed Gerrit basalts is 17% to 24% and Nd 13% to 14%. Maximum estimated crustal contributions of Hf are 30% to 45% and 33% to 37% for Nd. As the Yellowstone hotspot is believed to be the result of a mantle plume (Craig et al. 1978; Jordan et al. 2004), it is likely that in reality mantle melts are somewhat more enriched than the MORB composition used for our calculations, being closer to OIB characteristics. This would reduce the crustal component further; it is likely that these values provide an upper limit estimate for the crustal contribution to Gerrit basalts. It is therefore impossible based on this information to distinguish between a MORB-like source and a mantle plume source for Gerrit basalts.

4. Sr, Nd and Hf isotopes and water

Most of the basalt samples analyzed isotopically in this study were also analyzed in a parallel study for their H_2O, CO_2, Cl, F, and S concentrations (Stefano et al., 2010a and Stefano et al., 2010b) in olivine-hosted melt inclusions. Fig. 4.9 shows the relationship between the isotopic ratios of the basalt samples analyzed in this study and the highest water concentrations obtained from olivine-hosted melt inclusions in each of those samples. Despite the fact that the isotopic composition of these basalts is largely controlled by crustal interaction, H_2O is interpreted to be of a sub-crustal source

(Stefano et al. 2010a and b). However, there appears to be some correlation between the isotopic compositions of most samples and water contents. Excluding the two most water-rich samples, there is a trend showing generally higher H_2O at more primitive isotopic compositions in all three isotopic systems that could be an additional confirmation of a mantle origin for the water in the melt inclusions. The two most H_2O-rich samples plot well off the trend defined by the other samples, indicating that H_2O concentration is controlled by processes below the crust; where these basalts acquire their isotopic signatures. Therefore any correlation between isotopic composition and H_2O concentration likely results from samples retaining higher H_2O concentration if they have undergone less crustal interaction.

Conclusions

This study has presented new data for Sr, Nd and Hf isotopes in basalts of the Yellowstone hotspot as well as new $^{40}Ar/^{39}Ar$ dates for a number of basaltic lava flows throughout the region. Sr and Nd isotope data from this study agree with data obtained for Yellowstone hotspot basalts in previous studies, and consistently require crustal contamination of some mantle-derived melts. Hf isotopic compositions have been presented for the first time in Yellowstone hotspot basalts and trend in concert with Sr and Nd. The Hf isotopic compositions were compared with data obtained from rhyolites in the region, confirming a similar offset in the isotopic compositions of the rhyolites to what has been observed previously for Nd, indicating that the basalts have a smaller component of crustally derived Nd and Hf. Isotopic ratios plotted against longitude

show the strong influence of the crust that is penetrated on the composition of erupted basalts.

Isotopic ratios and trace element compositions are considered for two small suites of basalt samples, one penetrating the accreted terranes (western part of the region) and the other penetrating cratonized continental crust (eastern part of the region). The results are consistent with crustal control of the isotopic compositions for the erupted basalts in both cases. Assuming the basalts were originally MORB-like, the crustal contribution to Nd and Hf isotopes in Gerrit basalts are estimated to be between 13% and 45% depending on the assumed composition of the crustal component. The values above would be somewhat lower if a more plume-like composition were considered. With such an important crustal control on Nd and Hf isotopic ratios, it is difficult to make a conclusive argument about the nature of the source mantle of the Yellowstone hostpot using these isotopic systems.

Whole-rock isotopic ratios plotted against the H_2O concentrations in olivine-hosted melt inclusions for the Yellowstone hotspot basalts support the interpretation that H_2O has a sub-crustal origin. This provides further support for the findings of Stefano et al. (2010a) and Stefano et al. (2010b). It is not possible to determine whether the H_2O was already present in the lithosphere or whether it was brought in by the Yellowstone plume.

References

Armstrong, R. L., W. H. Taubeneck, et al. (1977). "Rb-Sr and K-Ar Geo-Chronometry of Mesozoic Granitic Rocks and Their Sr Isotopic Composition, Oregon, Washington, and Idaho." Geological Society of America Bulletin 88(3): 397-&.

Bonnichsen, B., W. P. Leeman, et al. (2008). "Miocene silicic volcanism in southwestern Idaho: geochronology, geochemistry, and evolution of the central Snake River Plain." Bulletin of Volcanology 70(3): 315-342.

Brandon, A. D., P. R. Hooper, et al. (1993). "Evaluating Crustal Contamination in Continental Basalts - the Isotopic Composition of the Picture Gorge Basalt of the Columbia River Basalt Group." Contributions to Mineralogy and Petrology 114(4): 452-464.

Brueseke, M. E., M. T. Heizler, et al. (2007). "Distribution and geochronology of Oregon Plateau (USA) flood basalt volcanism: The Steens Basalt revisited." Journal of Volcanology and Geothermal Research 161(3): 187-214.

Camp, V. E. (1995). "Mid-Miocene propagation of the Yellowstone mantle plume head beneath the Columbia River Basalt source region." Geology 23(5): 435-438.

Camp, V. E. and M. E. Ross (2004). "Mantle dynamics and genesis of mafic magmatism in the intermontane Pacific Northwest." Journal of Geophysical Research-Solid Earth 109(B8).

Camp, V. E., M. E. Ross, et al. (2003). "Genesis of flood basalts and Basin and Range volcanic rocks from Steens Mountain to the Malheur River gorge, Oregon." Geological Society of America Bulletin 115(1): 105-128.

Carlson, R. W. (1984). "Isotopic Constraints on Columbia River Flood-Basalt Genesis and the Nature of the Subcontinental Mantle." Geochimica Et Cosmochimica Acta 48(11): 2357-2372.

Christiansen, R. L. "The Quaternary and Pliocene Yellowstone Plateau volcanic field of Wyoming, Idaho, and Montana."

Christiansen, R. L., G. R. Foulger, et al. (2002). "Upper-mantle origin of the Yellowstone hotspot." Geological Society of America Bulletin 114(10): 1245-1256.

Craig, H. (1993). "Yellowston hotspot; a continetal mantle plume." Eos, Transactions, American Geophysical Union 74: 602.

Craig, H., J. E. Lupton, et al. (1978). "Helium Isotope Ratios in Yellowstone Park and Lassen Park Volcanic Gases." Geophysical Research Letters 5(11): 897-900.

Dodson, A., B. M. Kennedy, et al. (1997). "Helium and neon isotopes in the Imnaha Basalt, Columbia River Basalt Group; evidence for a Yellowstone plume source." Earth and Planetary Science Letters 150(3-4): 443-451.

Fleck, R. J. and R. E. Criss (1985). "Strontium and Oxygen Isotopic Variations in Mesozoic and Tertiary Plutons of Central Idaho." Contributions to Mineralogy and Petrology 90(2-3): 291-308.

Frey, H. M., R. A. Lange, et al. (2004). "Magma eruption rates constrained by Ar-40/Ar-39 chronology and GIS for the Ceboruco-San Pedro volcanic field, western Mexico (vol 116, pg 259, 2004)." Geological Society of America Bulletin 116(7-8): 1040-1040.

Gao, S., R. L. Rudnick, et al. (2004). "Recycling lower continental crust in the North China craton." Nature 432(7019): 892-897.

Geist, D. and M. Richards (1993). "Origin of the Columbia Plateau and Snake River plain; deflection of the Yellowstone plume." Geology 21(9): 789-792.

Graham, D. W., Reid, M. R., Jordan, B. T., Grunder, A. L., Leeman, W. P., Lupton, J. E. (2009). "Mantle Source Provinces Beneath the Northwestern USA Delimited by Helium Isotopes in Young Basalts." Journal of Volcanology and Geothermal Research 188(1-3): 128-140.

Hall, C. M. and J. W. Farrell (1995). "Laser Ar-40/Ar-39 Ages of Tephra from Indian-Ocean Deep-Sea Sediments - Tie Points for the Astronomical and Geomagnetic Polarity Time Scales." Earth and Planetary Science Letters 133(3-4): 327-338.

Hanan, B.B., and Graham, D.W., (1996). “Lead and helium isotope evidence from oceanic basalts for a common deep source of mantle plumes.” Science, v. 272, p. 991-995, doi: 10.126/science.272.5264.991.

Hanan, B. B., J. W. Shervais, et al. (2008). "Yellowstone plume-continental lithosphere interaction beneath the Snake River Plain." Geology 36(1): 51-54.

Harry, D. L. and W. P. Leeman (1995). "Partial Melting of Melt Metasomatized Subcontinental Mantle and the Magma Source Potential of the Lower Lithosphere." Journal of Geophysical Research-Solid Earth 100(B6): 10255-10269.

Hart and Mertzman (1983). “Volcanic Stratigraphy of the Jordan Valley area.” Oregon Geology, 45(2): 15-19.

Hart, W. K. (1985). "Chemical and Isotopic Evidence for Mixing between Depleted and Enriched Mantle, Northwestern USA." Geochimica Et Cosmochimica Acta 49(1): 131-144.

Hofmann, A. W. and E. Welin (1988). "Chemical differentiation of the Earth; the relationship between mantle, continental crust, and oceanic crust." Earth and Planetary Science Letters 90(3): 297-314.

Humphreys, G., D. Schutz, K. Dueker and R. B. Smith, 2000, Plume or no plume at Yellowstone, GSA Today, vol. 10, no. 12, 1-7.

Hyodo H., York D. (1993). "The discovery and significance of a fossilized radiogenic Argon wave (Argonami) in the Earth's crust."Geophysical Research Letters, vol. 20, no. 1, pp.61-64, 08

Johnson D.M., H. P. R., and Conrey, R.M. (1999). "GeoAnalytical Lab, Washington State University." Advances in X-ray Analysis vol 41: 843-867.

Jordan, B. T., A. L. Grunder, et al. (2004). "Geochronology of age-progressive volcanism of the Oregon High Lava Plains: Implications for the plume interpretation of Yellowstone." Journal of Geophysical Research-Solid Earth 109(B10).

Knaack, C., Cornelius, S., Hooper, P.R. (1994). "TRACE ELEMENT ANALYSIS OF ROCKS AND MINERALS BY ICP-MS." Open File Report, Department of Geology, Washington State University.

Leeman, W. P. (1982). "Development of the Snake River plain-Yellowstone Plateau Province, Idaho and Wyoming; an overview and petrologic model." Bulletin - Idaho Bureau of Mines and Geology 26: 155-177.

Leeman, W. P., Schutt, D.L., Hughes, S.S. (2009). "Thermal structure beneath the Snake River Plain: Implications for the Yellowstone hot spot." Journal of Volcanology and Geothermal Research 188(1-3): 128-140.

Leeman, W. P., C. Annen, et al. (2008). "Snake River plain-Yellowstone silicic volcanism; implications for magma genesis and magma fluxes." Geological Society Special Publications 304: 235-259.

Leeman, W. P. and W. I. Manton (1971). "Strontium Isotopic Composition of Basaltic Lavas from Snake River Plain, Southern Idaho." Earth and Planetary Science Letters 11(5): 420

Leeman, W. P., M. A. Menzies, et al. (1985). "Strontium, Neodymium and Lead Isotopic Compositions of Deep Crustal Xenoliths from the Snake River Plain - Evidence for Archean Basement." Earth and Planetary Science Letters 75(4): 354-368.

Leeman, W. P., J. S. Oldow, et al. (1992). "Lithosphere-Scale Thrusting in the Western United-States Cordillera as Constrained by Sr and Nd Isotopic Transitions in Neogene Volcanic-Rocks." Geology 20(1): 63-66.

Manea, V. C., Manea M., Leeman, W.P., Schutt, D.L. (2009). "The influence of plume head-lithosphere interaction on magmatism associated with the Yellowstone

hotspot track." Journal of Volcanology and Geothermal Research 188(1-3): 68-85.

McCurry, M., Rogers, D. W. (2009). "Mass transfer along the Yellowstone hotspot track I: Petrologic constraints on the volume of mantle-derived magma." Journal of Volcanology and Geothermal Research 188(1-3): 86-98.

McDonough, W. F. and S. S. Sun (1995). "The Composition of the Earth." Chemical Geology 120(3-4): 223-253.

Mukasa S.B., Shervais J.W., Wilshire H.G., Nielson J.E., 1991. Intrinsic Nd, Pb, and Sr isotopic heterogeneities exhibited by the Lherz Peridotite Massif, French Pyrenees. J. Petrol. Spec. Lith. Issue, 117-134.

Munker, C., S. Weyer, et al. (2001). "Separation of high field strength elements (Nb, Ta, Zr, Hf) and Lu from rock samples for MC-ICPMS measurements." Geochemistry Geophysics Geosystems 2.

Nash, B. P., M. E. Perkins, et al. (2006). "The Yellowstone hotspot in space and time: Nd and Hf isotopes in silicic magmas." Earth and Planetary Science Letters 247(1-2): 143-156.

Obradovich, J. D. "Geochronology of the late Cenozoic volcanism of Yellowstone National Park and adjoining areas, Wyoming and Idaho."

Pierce, K. L. and L. A. Morgan (1992). "The track of the Yellowstone hot spot; volcanism, faulting, and uplift." Memoir - Geological Society of America 179: 1-53.

Renne, P. R., A. L. Deino, et al. (1994). "Intercalibration of Astronomical and Radioisotopic Time." Geology 22(9): 783-786.

Salters, V. J. M. and S. R. Hart (1991). "The Mantle Sources of Ocean Ridges, Islands and Arcs - the Hf-Isotope Connection." Earth and Planetary Science Letters 104(2-4): 364-380.

Savov, I. P. L., W. P.; Lee, C. A.; Shirey, S. B. (2009). "Boron isotopic variations in NW USA rhyolites: Yellowstone, Snake River Plain, Eastern Oregon." Jounal of Volcanology and Geothermal Research 188(1-3): 162-172.

Shervais, J. W., S. K. Vetter, et al. (2006). "Layered mafic sill complex beneath the eastern Snake River Plain: Evidence from cyclic geochemical variations in basalt." Geology 34(5): 365-368.

Vervoort, J. D., P. J. Patchett, et al. (1999). "Relationships between Lu-Hf and Sm-Nd isotopic systems in the global sedimentary system." Earth and Planetary Science Letters 168(1-2): 79-99.

Waite, G. P., D. L., R. B. Smith, and R. L. Allen, 2006, VP and VS structure of the Yellowstone hot spot from teleseismic tomography: Evidence for an upper mantle plume, J. Geophys. Res. vol. 111, B04303, doi:10.1029/2005JB003867.

Yuan, H. Y. and K. Dueker (2005). "Teleseismic P-wave tomogram of the Yellowstone plume." Geophysical Research Letters 32(7).

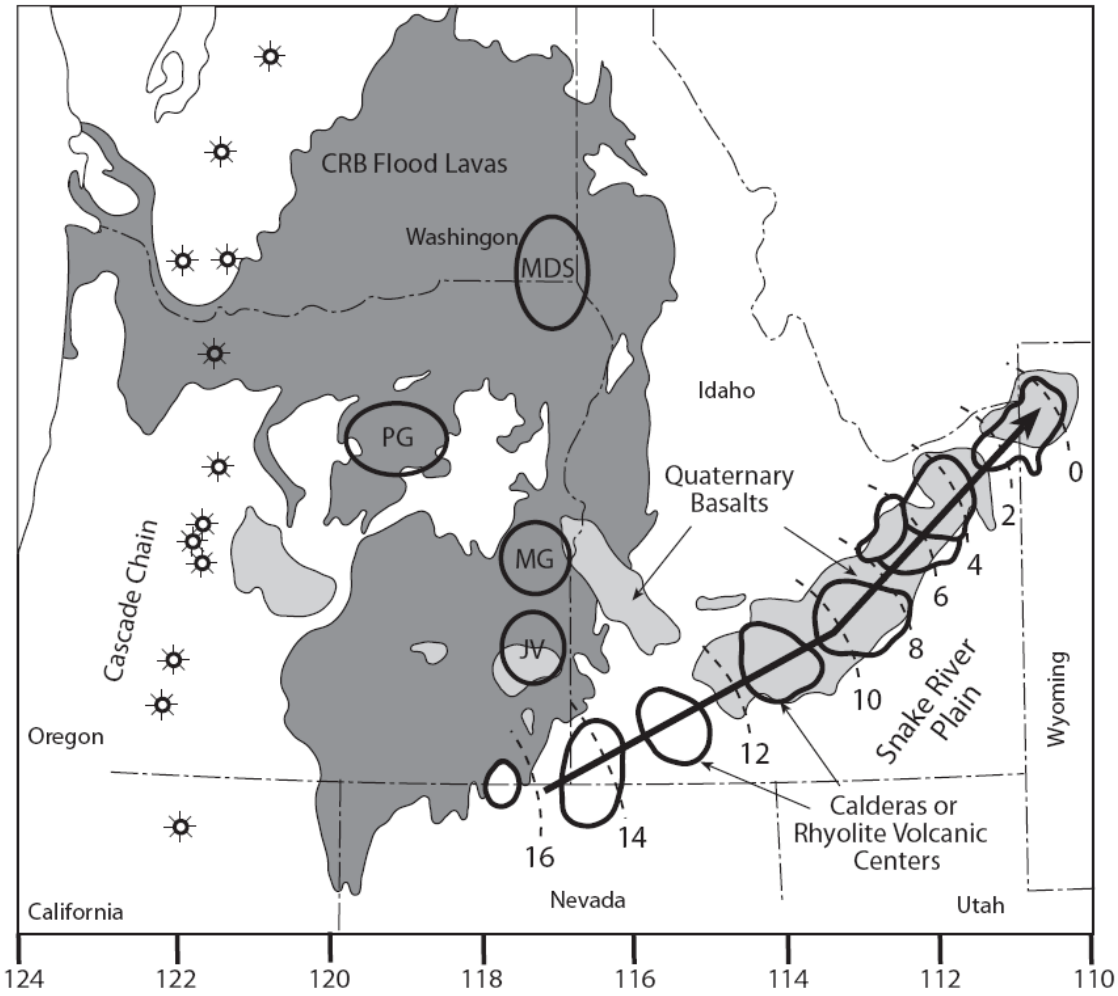

Figure 4.1. Schematic map of the Pacific Northwest region of the United States showing the Yellowstone Hotspot and CRB sample locations. Areas of the CRB sampled in this study are circled and labeled (MDS- Monument Dike Swarm, PG- Picture Gorge basalts, MG- Malheur Gorge, JV- Jordan Valley)Approximate caldera locations and ages (in Ma) are shown along the Snake River Plain. Also shown is the Cascade arc. Modified from Camp and Ross (2004).

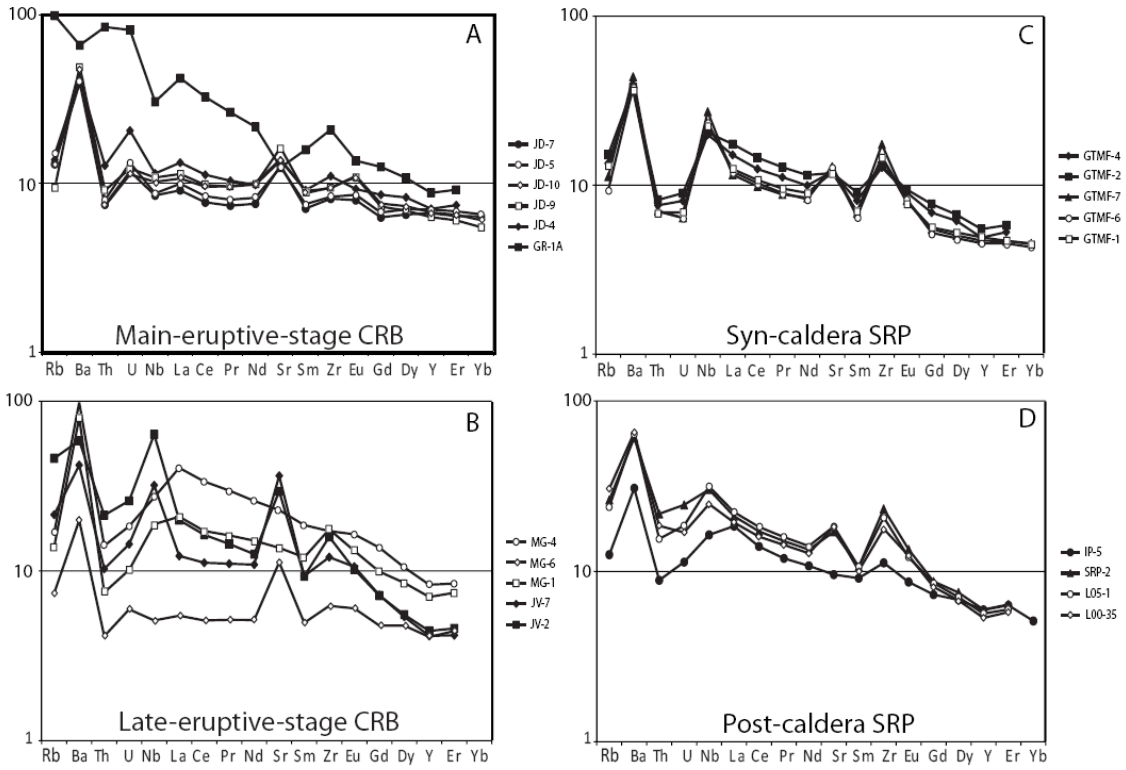

Figure 4.2. Primitive-mantle normalized (Hofmann, 1988) trace element distribution diagrams for basalts of the Yellowstone hotspot. Note the pronounced relative Ba and Sr enrichment recorded by many samples.

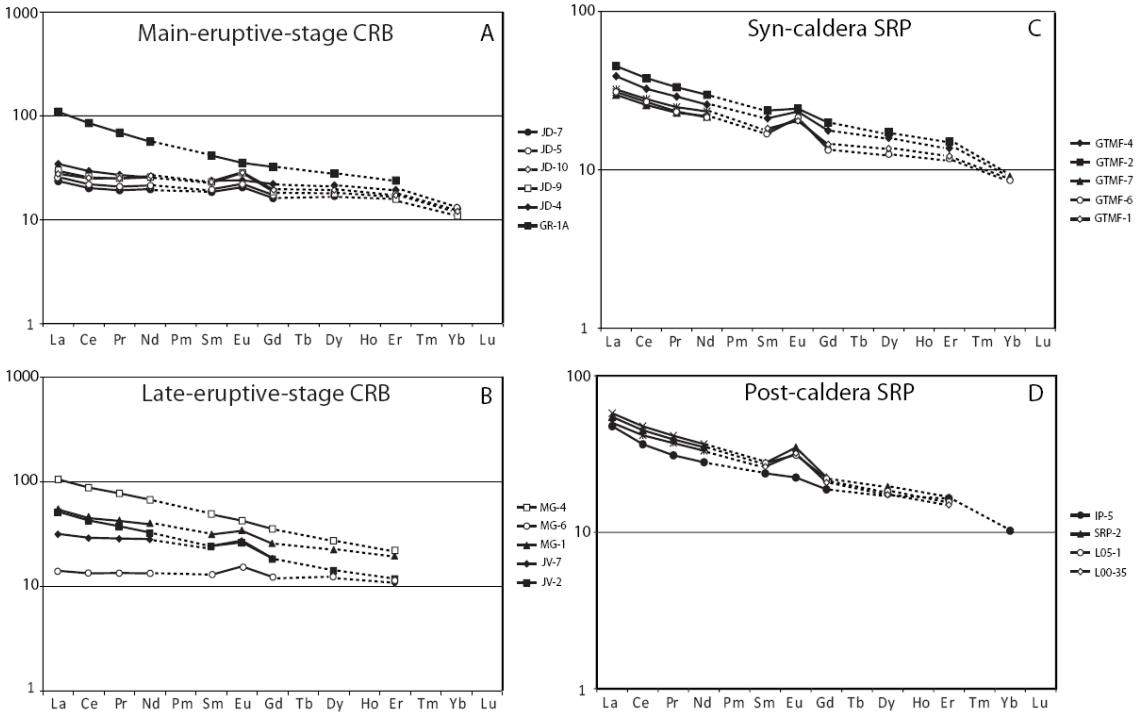

Figure 4.3. Chondrite-normalized (McDonough and Sun, 1995) rare earth element (REE) diagrams for basalts from the Yellowstone hotspot. Note the light REE enrichment shown by many samples, and the small positive Eu anomaly, also exhibited by many samples.

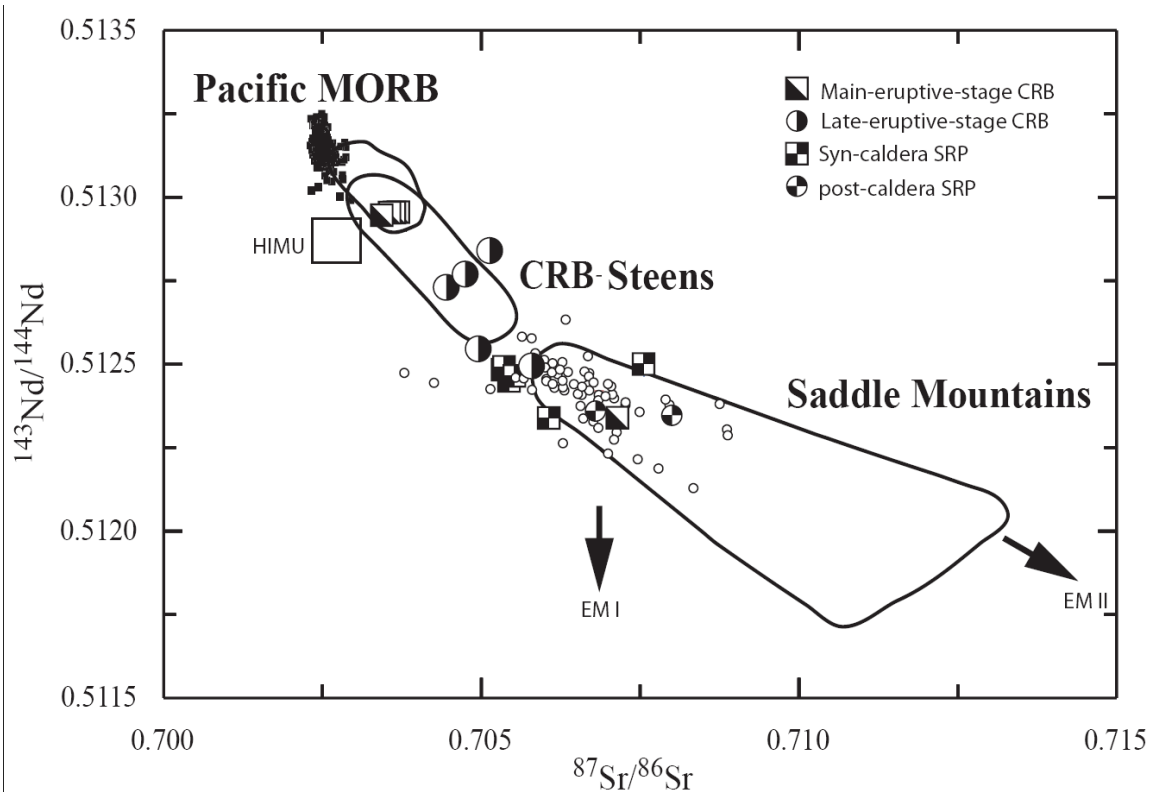

Figure 4.4. New Nd and Sr isotope data for the Yellowstone hotspot plotted with fields for the CRB/Steens basalts and Saddle Mountains basalts from Hanan et al. (2008). Small black points show Pacific MORB (Hanan and Graham, 1996), and small open circles show values for SRP basalts from Hanan et al. (2008). Also plotted are the general locations of the mantle end-members HIMU, EM I and EM II. Modified after Hanan et al. (2008).

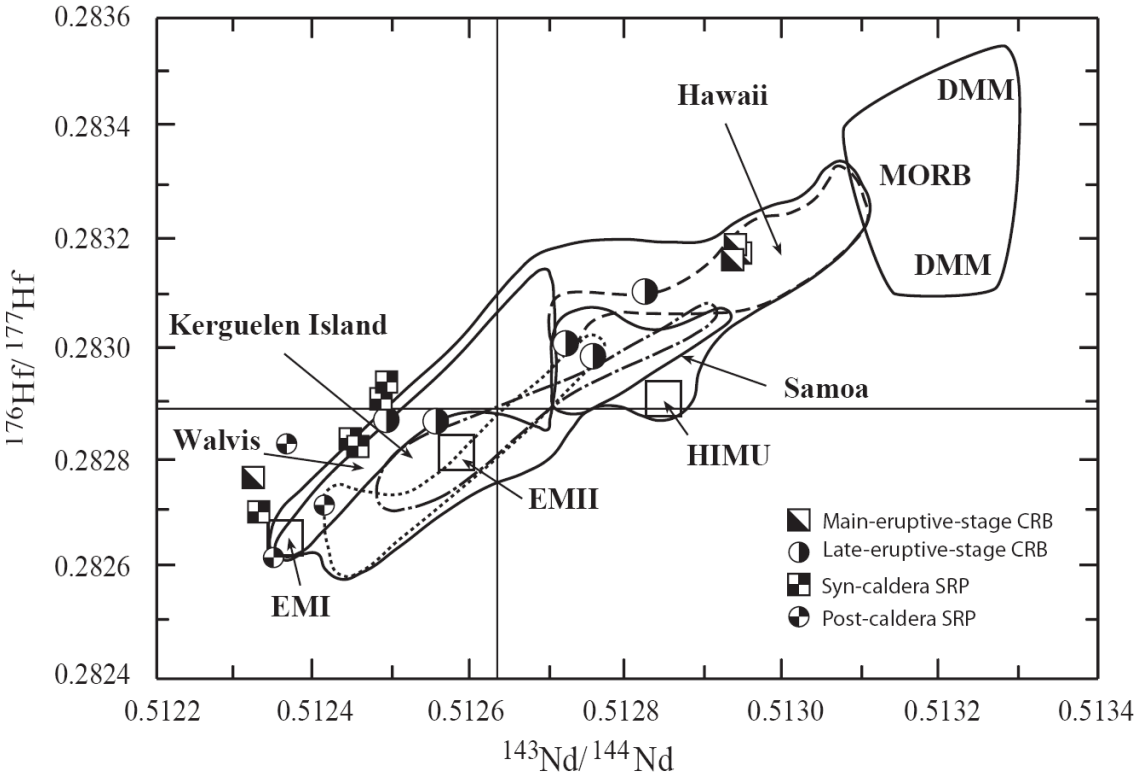

Figure 4.5. Hf and Nd isotope data for Yellowstone hotspot basalts plotted with fields for the mantle end-members DMM, HIMU, EM I and EM II as well as some general fields for a variety of OIBS for comparison. Modified from Salters and Hart (1991).

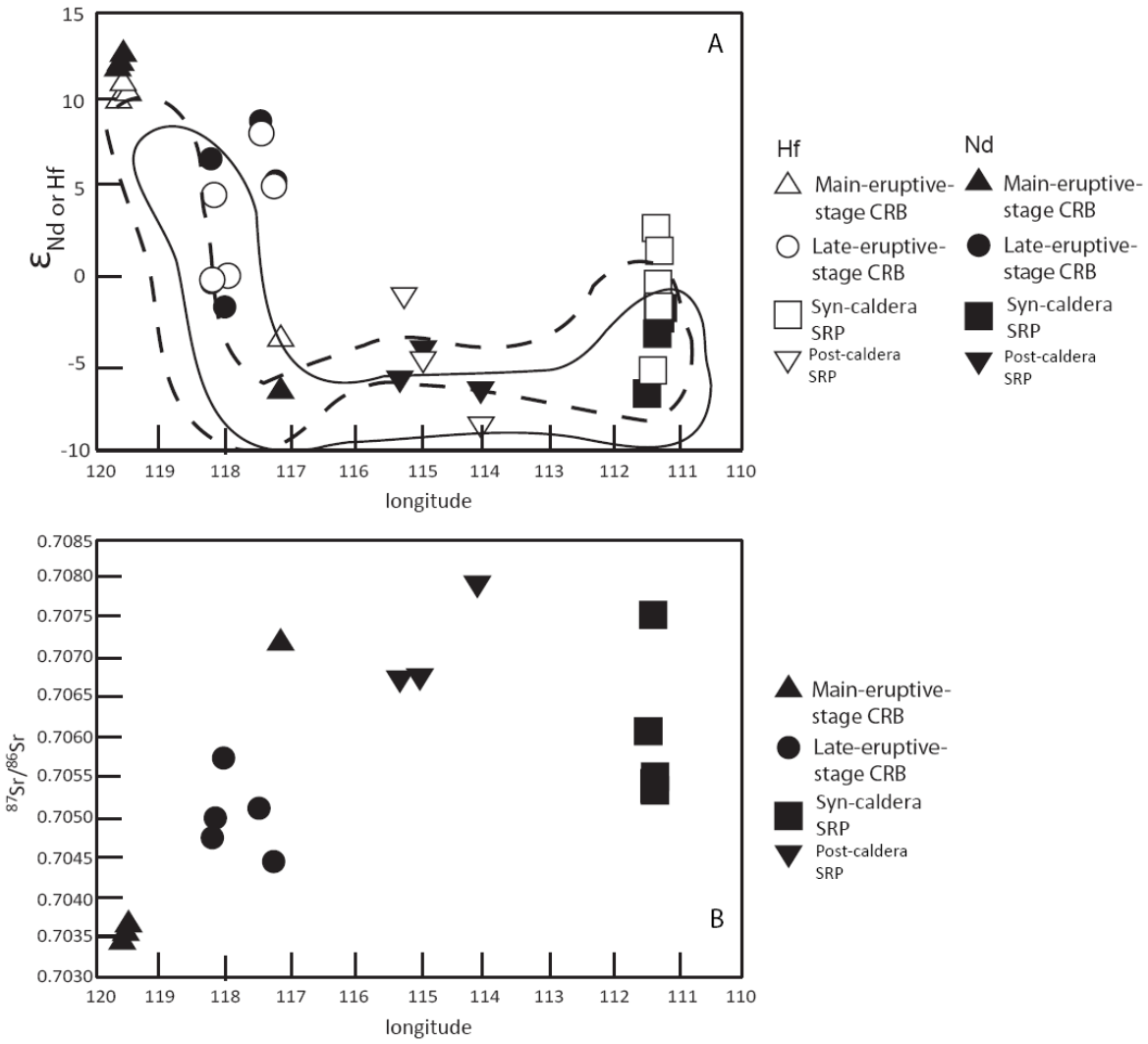

Figure 4.6. Sr, Nd and Hf isotopes of Yellowstone hotspot basalts plotted against the Longitude at which they were collected. The difference between accreted terranes in the west and cratonic crust in the east is very clear. Also note the spread in isotopic compositions in the easternmost lavas. The fields of Nd (solid line) and Hf (dashed line) as analyzed in rhyolites by Nash et al. (2006) are shown on the upper diagram for comparison.

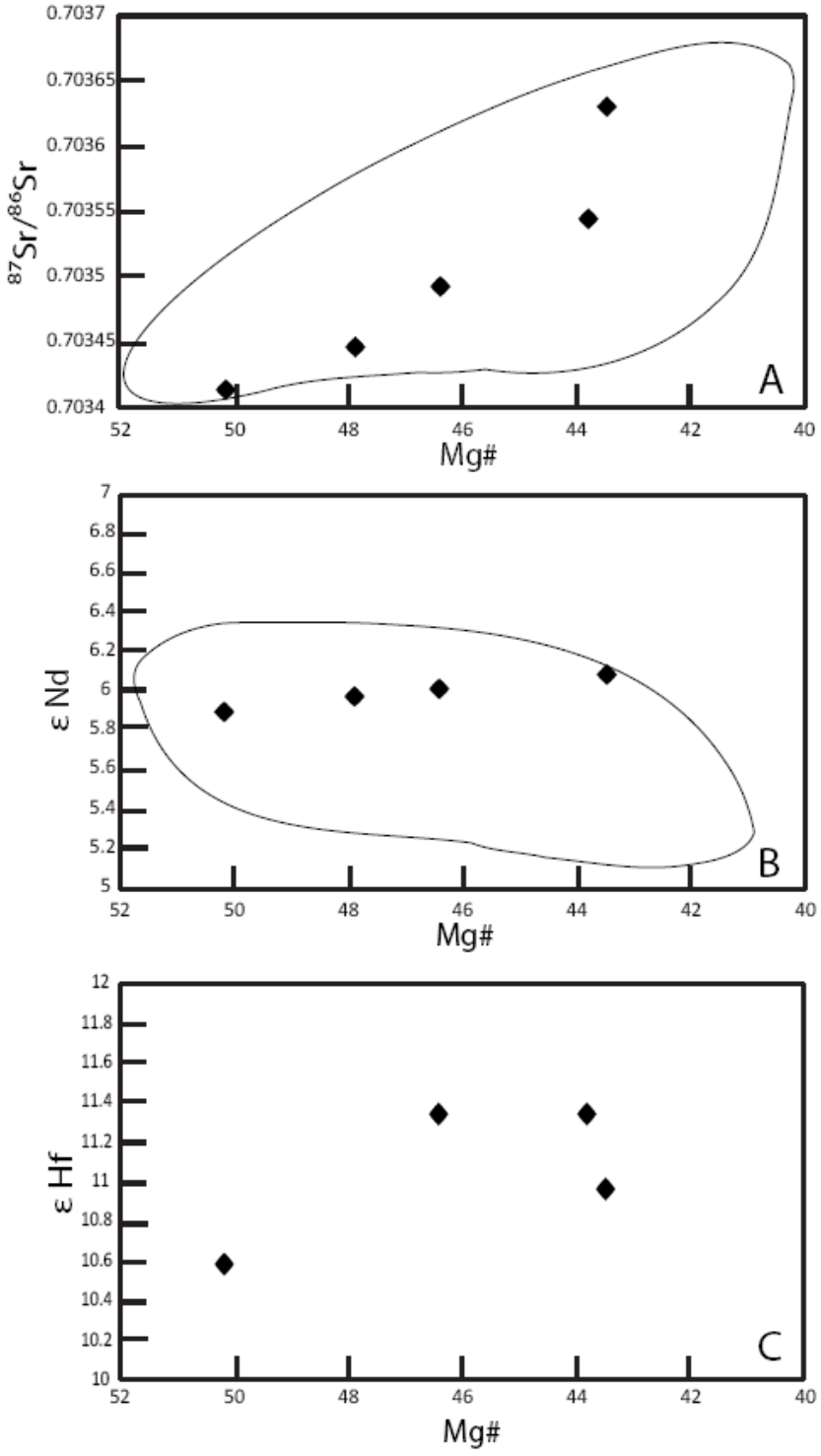

Figure 4.7. Sr, Nd and Hf isotopes of Picture Gorge basalts in the CRB plotted against the Mg# of the lava, showing a strong correlation with Sr isotopes. The fields of data collected by Brandon et al. (1993) are included for Nd and Sr. The variation in Nd and Hf isotopes is very small, and so it is difficult to tell if the same correlation is present in these isotopic systems.

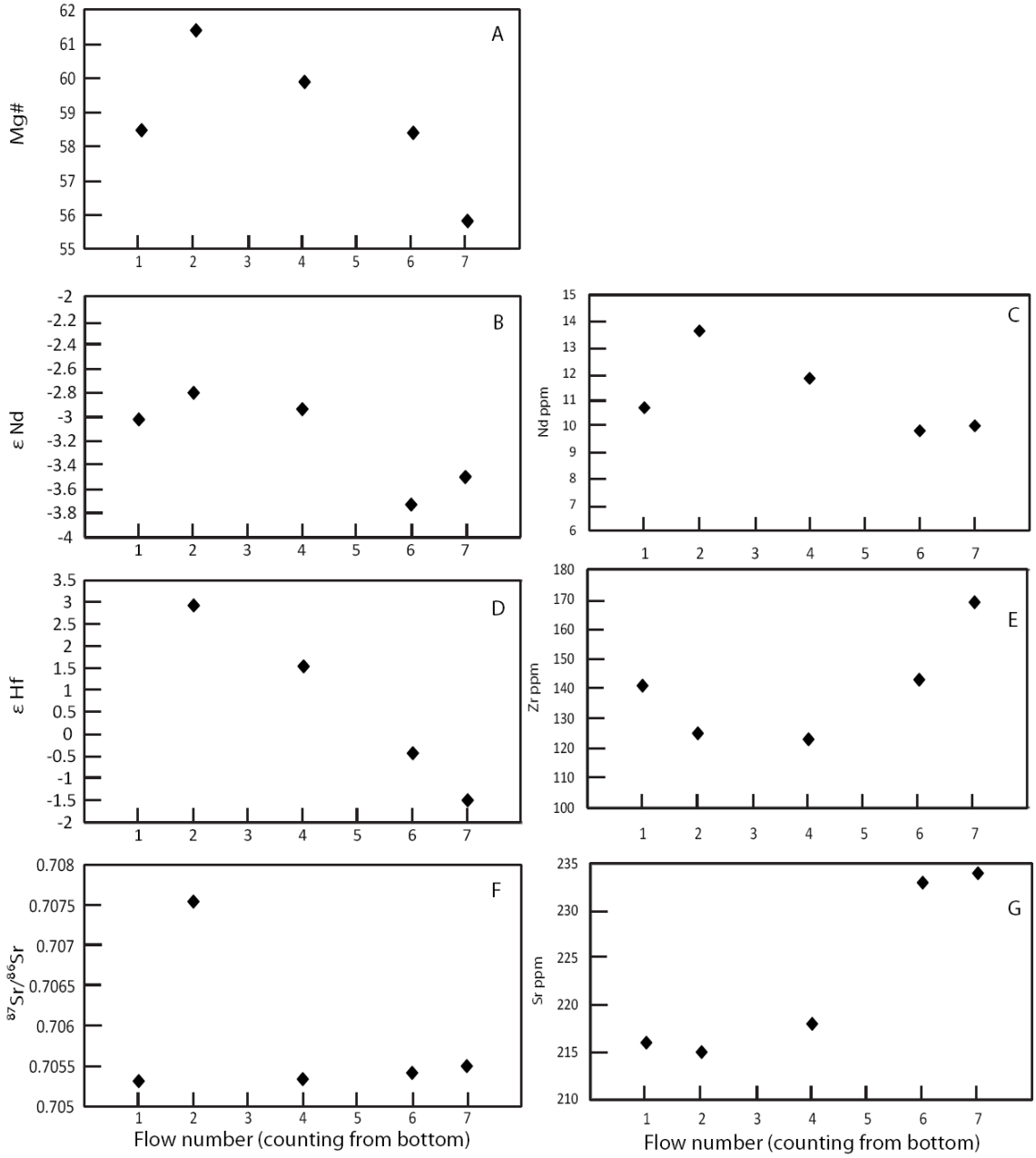

Figure 4.8. Sr, Nd and Hf isotopic compositions, Mg# and selected trace elements for a vertical section of flows of Gerrit Basalt. Data are plotted against flow number, counting from the bottom. The smooth descent of Mg# from flow #2 through #7 indicates increasing crustal interaction up section, and the isotopic compositions and trace elements vary in concert.

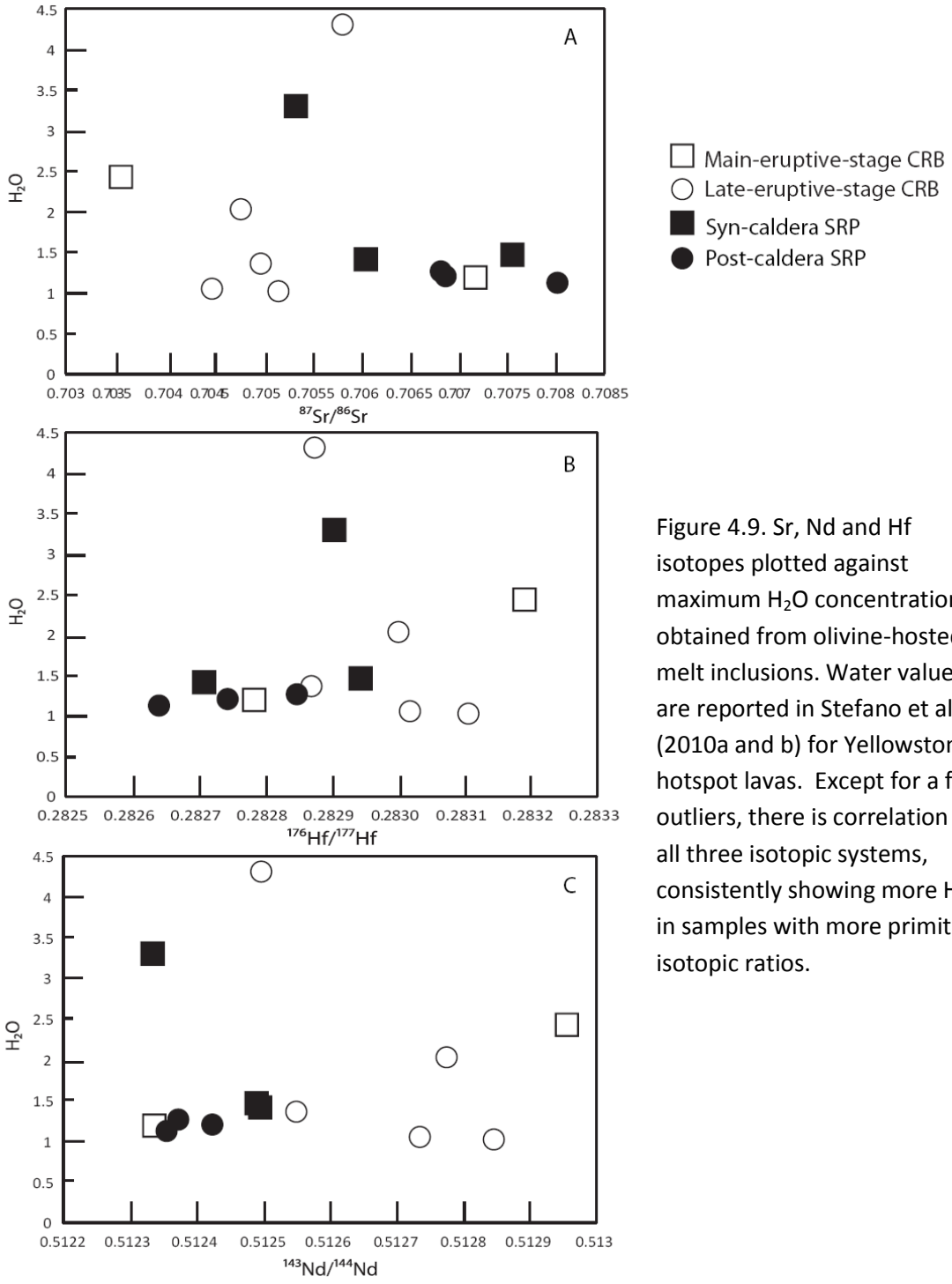

Figure 4.9. Sr, Nd and Hf isotopes plotted against maximum H_2O concentrations obtained from olivine-hosted melt inclusions. Water values are reported in Stefano et al. (2010a and b) for Yellowstone hotspot lavas. Except for a few outliers, there is correlation in all three isotopic systems, consistently showing more H_2O in samples with more primitive isotopic ratios.

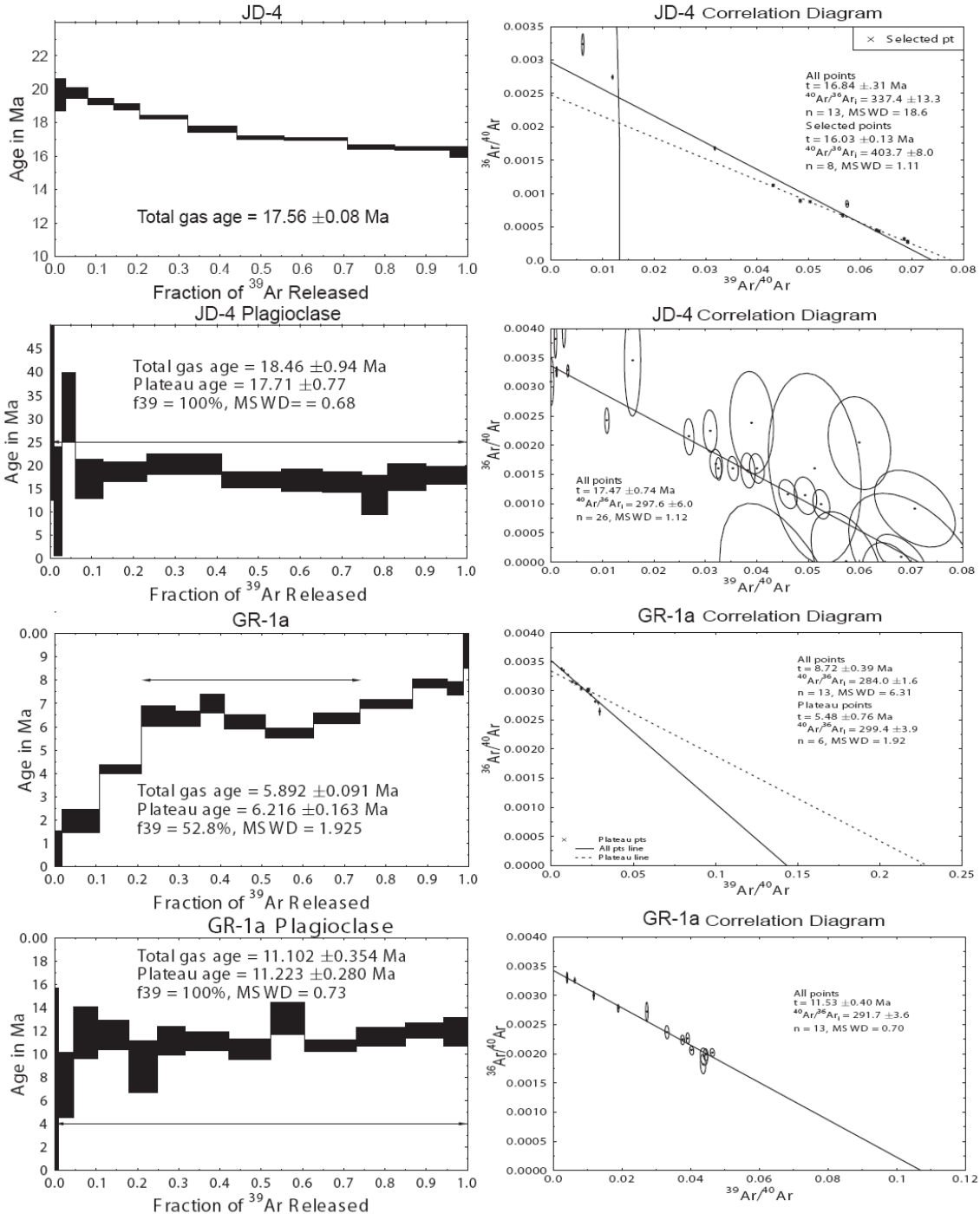

Figure 4.10. $^{40}Ar/^{39}Ar$ age spectrum and correlation (isochron) diagrams for main-eruptive- stage CRB lavas.

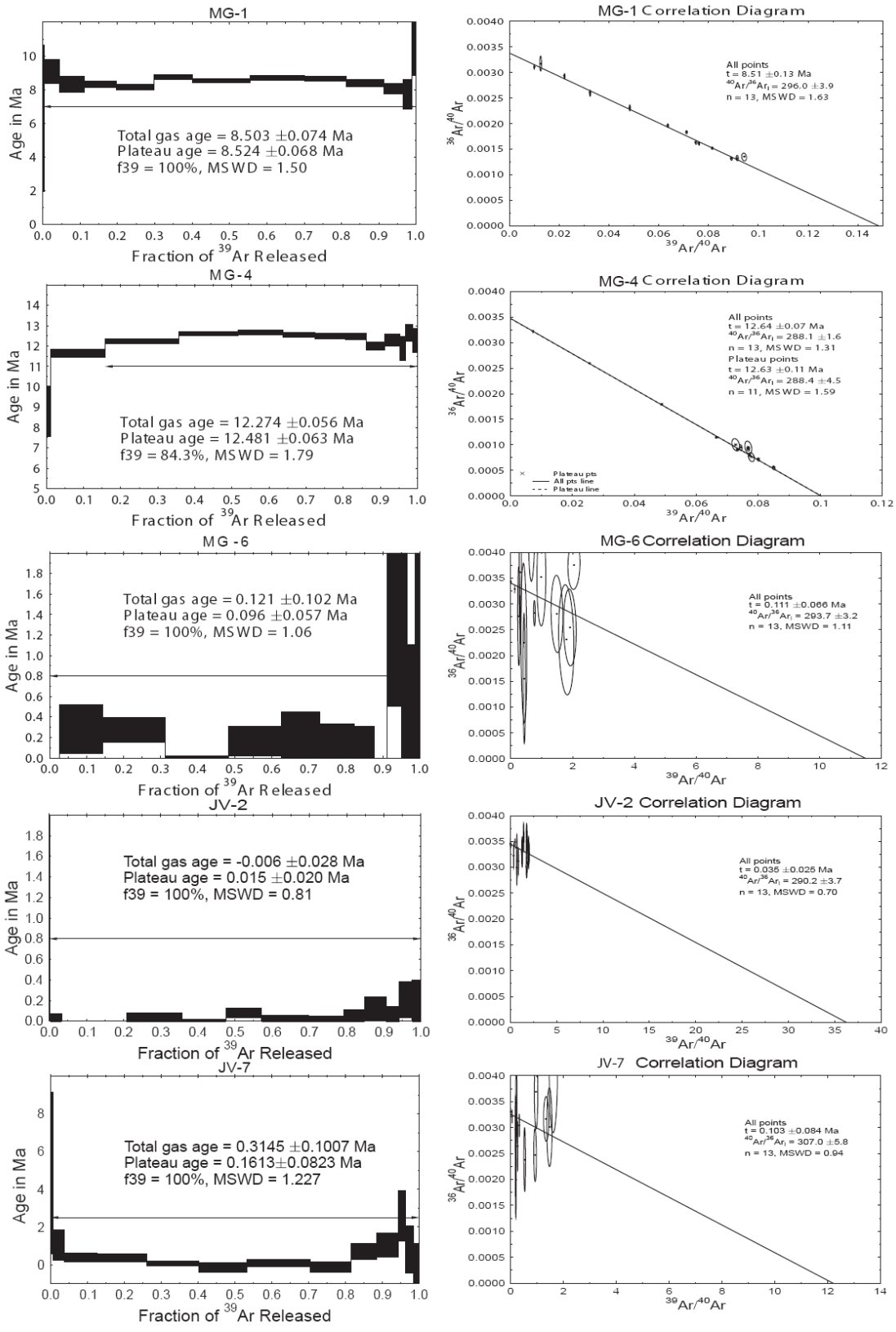

Figure 4.11. $^{40}Ar/^{39}Ar$ age spectrum and correlation (isochron) diagrams for late-eruptive- stage CRB lavas.

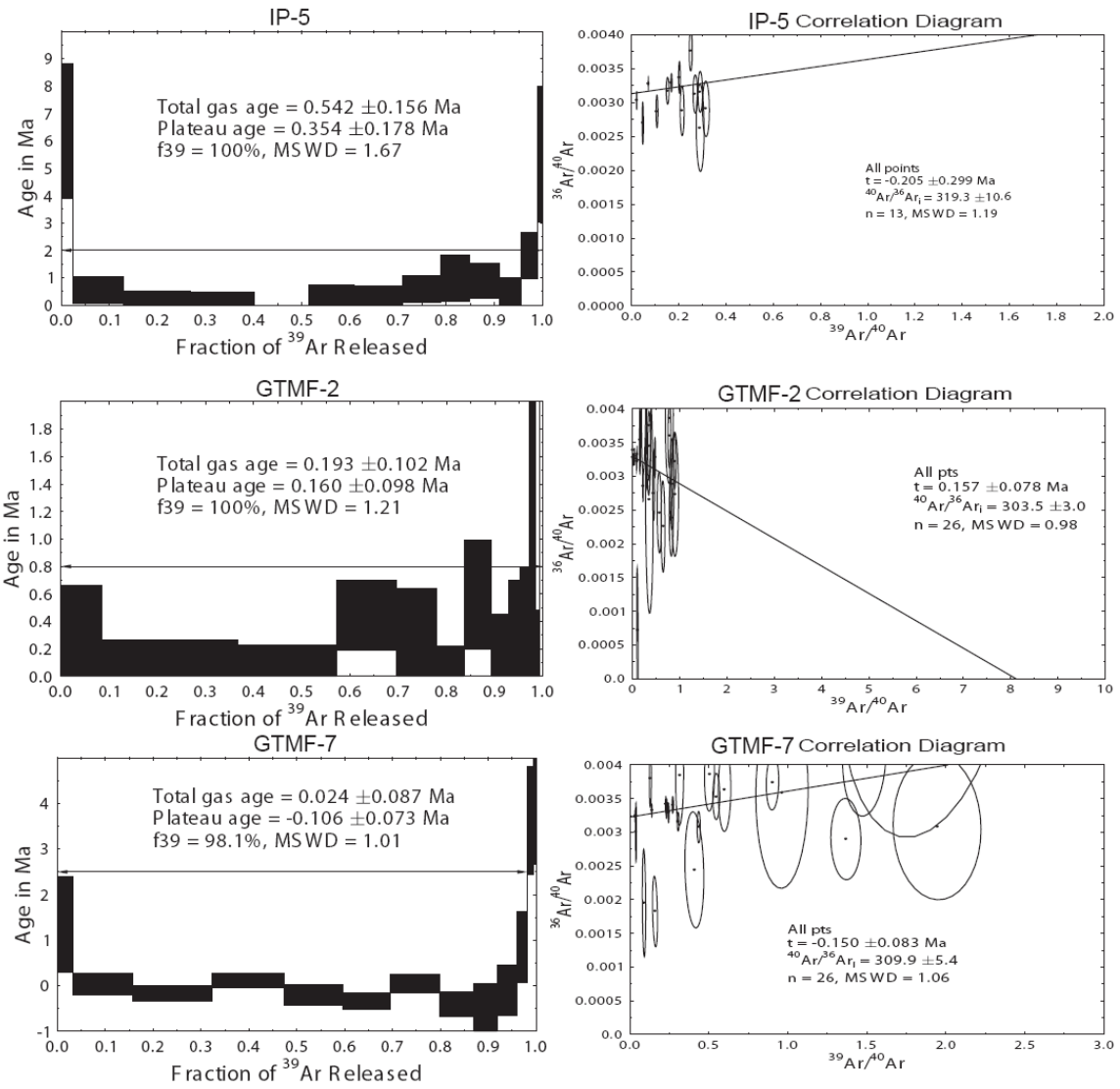

Figure 4.12. $^{40}Ar/^{39}Ar$ age spectrum and correlation (isochron) diagrams for syn-caldera SRP lavas.

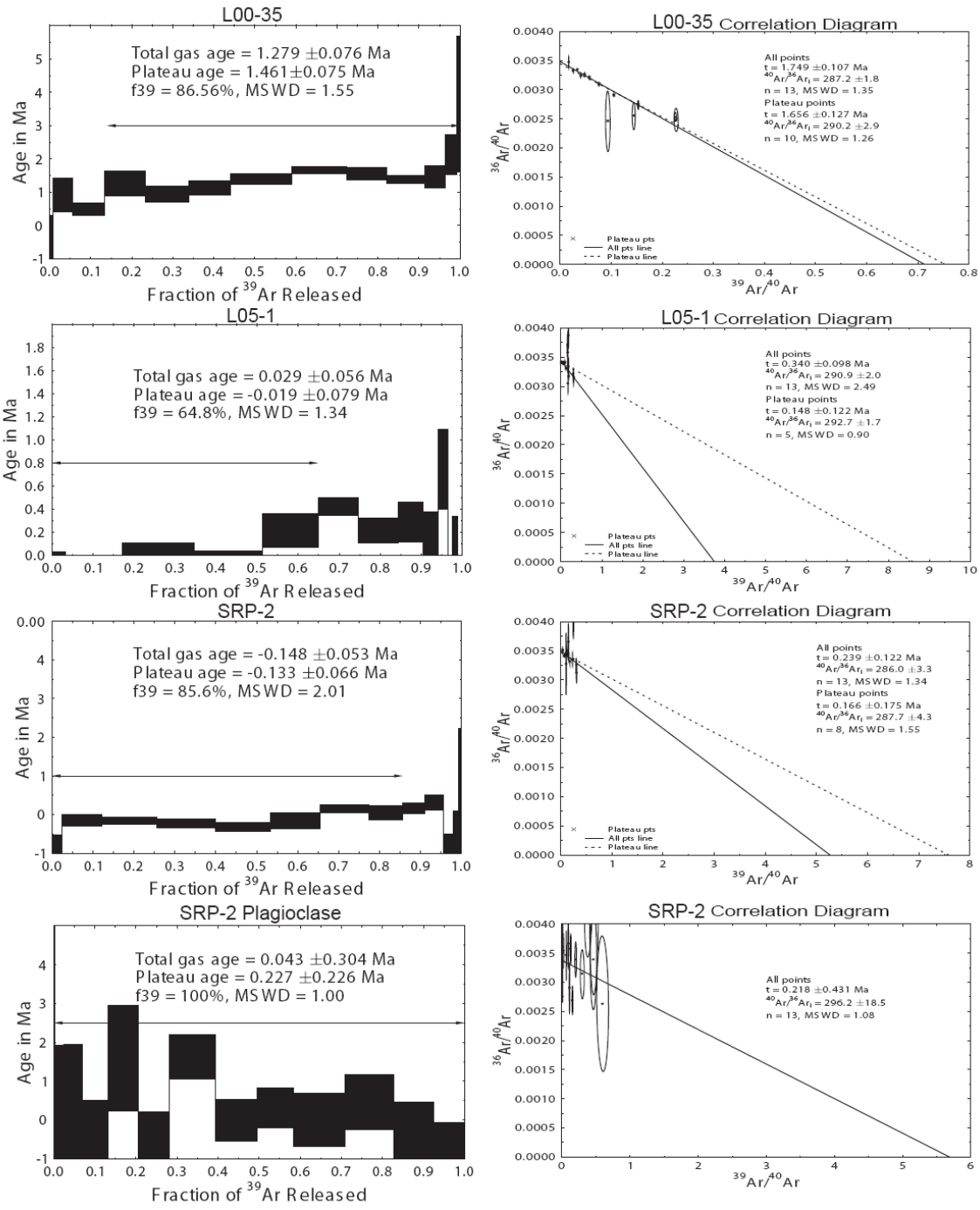

Figure 4.13. $^{40}Ar/^{39}Ar$ age spectrum and correlation (isochron) diagrams for post-caldera SRP lavas.

TABLE 4.1. Major oxide and trace elements of Yellowstone hotspot basalts

	SRP syn-caldera basalts	GTMF-1	GTMF-2	GTMF-4	GTMF-6	GTMF-7	IP-5	SRP post-caldera basalts	SRP-2	l05-1	l00-35
SiO_2		48.24	48.26	48.41	48.26	48.25	48.12		48.34	48.88	48.92
TiO_2		1.55	1.58	1.57	1.51	1.81	1.20		2.96	2.21	2.39
Al_2O_3		16.17	15.65	16.28	16.84	15.96	14.63		14.85	16.22	15.55
FeO		10.88	10.58	10.37	10.59	11.47	11.60		13.37	11.21	11.94
MnO		0.16	0.18	0.18	0.16	0.17	0.18		0.20	0.18	0.19
MgO		8.60	9.44	8.68	8.34	8.12	10.59		7.64	7.59	7.31
CaO		11.56	11.32	11.57	11.45	11.28	10.90		9.10	9.92	10.09
Na_2O		2.29	2.34	2.36	2.35	2.40	2.13		2.64	2.84	2.59
K_2O		0.41	0.45	0.42	0.38	0.43	0.36		0.72	0.66	0.80
P_2O_5		0.14	0.20	0.15	0.12	0.11	0.28		0.18	0.28	0.22
H_2O			1.46	3.30			1.41		1.09	1.15	1.01
Rb			8.10	7.20			6.70		14.00	12.80	16.40
Ba		221.75	229.00	227.00	228.70	264.85	186.00		368.00	386.00	396.00
Th		0.56	0.66	0.62	0.57	0.57	0.72		1.77	1.26	1.50
U		0.14	0.18	0.16	0.13	0.13	0.23		0.50	0.38	0.34
Nb		14.08	12.61	12.28	14.50	16.78	10.10		18.63	19.42	15.33
La		7.63	10.73	9.26	7.36	7.06	11.30		12.93	13.67	11.88
Ce		17.16	23.26	19.94	16.45	15.73	22.40		27.50	29.17	25.57
Pr		2.31	3.09	2.69	2.17	2.13	2.88		3.64	3.84	3.45
Nd		10.69	13.62	11.81	9.81	10.00	12.80		15.97	16.74	15.18
Sr			215.00	218.00			174.00		311.00	334.00	331.00
Sm		2.70	3.50	3.13	2.51	2.63	3.52		4.11	4.10	3.89
Zr			125.00	123.00			109.00		226.00	202.00	172.00
Eu		1.15	1.37	1.31	1.20	1.18	1.26		1.96	1.76	1.79
Gd		2.88	3.96	3.52	2.68	2.81	3.74		4.46	4.38	4.15
Dy		3.35	4.26	3.92	3.09	3.21	4.34		4.79	4.50	4.31
Y		19.35	21.63	19.27	17.86	18.50	23.40		23.48	22.25	21.01
Er		1.95	2.41	2.20	1.88	1.94	2.63		2.66	2.49	2.49
Yb		1.97			1.89	1.99	2.25				

Major oxide and trace element compositions of selected Yellowstone Hotspot basalts. H_2O concentrations previously published in Stefano et al. (2010a and 2010b)

TABLE 4.1. cont.

	CRB main-stage basalts	JD-4	JD-5	JD-7	JD-9	JD-10	GR-1a	CRB late basalts	MG-1	Mg-4	MG-6	JV-2	JV-7
SiO_2		51.62	50.20	50.00	50.13	50.26	54.18		48.58	49.48	48.92	49.34	48.33
TiO_2		1.45	1.51	1.50	1.88	1.86	2.10		2.06	2.21	0.91	2.09	2.34
Al_2O_3		16.48	17.00	17.14	15.29	15.05	14.08		16.11	16.07	16.84	16.86	16.65
FeO		10.42	11.64	11.77	11.77	11.67	11.62		11.36	11.83	9.46	9.96	10.27
MnO		0.18	0.18	0.18	0.18	0.17	0.19		0.19	0.20	0.17	0.16	0.16
MgO		5.06	5.09	5.08	6.07	6.60	4.83		7.57	6.52	9.53	7.40	8.25
CaO		11.02	10.95	11.00	10.81	10.73	8.52		10.42	9.31	11.18	9.41	9.80
Na_2O		2.98	2.75	2.68	3.08	2.85	2.66		2.67	3.01	2.62	3.26	3.26
K_2O		0.63	0.50	0.46	0.54	0.57	1.60		0.74	0.81	0.28	1.24	0.73
P_2O_5		0.17	0.18	0.18	0.24	0.23	0.23		0.30	0.56	0.08	0.27	0.21
H_2O		2.35					1.11		4.24	1.29	1.96	0.98	0.95
Rb		7.41					53.37		7.41	8.98	3.96	24.35	11.47
Ba		251.69	253.01	240.94	301.17	291.14	402.26		482.54	595.22	120.13	362.19	254.31
Th		1.04	0.65	0.61	0.74	0.60	6.94		0.61	1.14	0.34	1.68	0.84
U		0.42	0.27	0.24	0.25	0.23	1.66		0.21	0.37	0.12	0.50	0.29
Nb		7.10	5.40	5.25	6.70	6.32	18.93		11.62	16.75	3.15	39.03	19.74
La		8.18	6.13	5.60	7.00	6.58	25.99		12.82	24.87	3.34	12.50	7.52
Ce		18.07	13.49	12.38	15.70	15.35	52.34		27.55	53.80	8.18	26.81	17.87
Pr		2.51	1.94	1.79	2.32	2.33	6.42		3.91	7.19	1.25	3.55	2.66
Nd		11.69	9.79	9.03	11.75	12.05	25.86		17.91	30.77	6.10	15.26	12.94
Sr		249.49					226.98		249.12	415.29	204.51	534.88	661.98
Sm		3.53	2.92	2.75	3.39	3.49	6.15		4.64	7.20	1.91	3.71	3.61
Zr		107.59					203.09		170.72	166.54	60.40	153.70	117.07
Eu		1.35	1.25	1.16	1.59	1.62	1.99		1.91	2.39	0.87	1.51	1.54
Gd		4.40	3.45	3.23	3.74	3.90	6.44		5.07	7.03	2.44	3.72	3.69
Dy		5.28	4.49	4.18	4.40	4.69	6.89		5.42	6.69	3.04	3.61	3.42
Y		27.88	27.58	26.24	24.91	26.58	34.73		27.66	32.67	16.08	17.36	16.29
Er		3.10	2.85	2.67	2.52	2.72	3.83		3.09	3.50	1.84	1.92	1.74
Yb			2.89	2.81	2.42	2.67							

Major oxide and trace element compositions of selected Yellowstone Hotspot basalts. H_2O concentrations previously published in Stefano et al. (2010a and 2010b)

Table 4.2. Nd, Sr and Hf Isotopic ratios of Yellowstone hotspot basalts

	longitude	$^{143}Nd/^{144}Nd$	error	εNd	$^{87}Sr/^{86}Sr$	error	$^{176}Hf/^{177}Hf$	error	εHf
GR-1a	117.13	0.512328	0.0017	-6.04715	0.707117	0.0007	0.282774	0.0000148	-3.03861
JD-4	119.51	0.512946	0.0018	6.008138	0.703496	0.0012	0.283181	0.0000215	11.34178
JD-5	119.51				0.703546	0.002	0.283181	0.0000074	11.34235
JD-7	119.49	0.5129497	0.0011	6.080314	0.703631	0.001	0.28317	0.0000057	10.96368
JD-9	119.56	0.512944	0.0019	5.969124	0.703446	0.0013			
JD-10	119.56	0.51294	0.0018	5.891097	0.703415	0.0011	0.283159	0.0000058	10.58474
MG-1	117.99	0.5124893	0.0017	-2.90068	0.705766	0.0007	0.282866	0.0000185	0.208823
MG-4	118.15	0.512542	0.002	-1.87267	0.704932	0.0008	0.282861	0.0000141	0.042045
MG-6	118.16	0.512767	0.0017	2.516396	0.704728	0.0007	0.282992	0.0000430	4.673774
JV-2	117.22	0.512727	0.0028	1.736118	0.704434	0.0008	0.283009	0.0000159	5.285258
JV-7	117.45	0.5128378	0.0019	3.897487	0.705112	0.0015	0.283098	0.0000339	8.399915
GTMF-1	111.33	0.512483	0.0012	-3.02358	0.705314	0.0016			
GTMF-2	111.33	0.5124945	0.002	-2.79925	0.707546	0.0009	0.282943	0.0000243	2.92194
GTMF-4	111.33	0.5124877	0.0019	-2.93189	0.705339	0.0008	0.282904	0.0000318	1.552005
GTMF-6	111.33	0.5124469	0.002	-3.72778	0.705417	0.0013	0.282848	0.0000070	-0.42424
GTMF-7	111.33	0.512459	0.001	-3.49174	0.7055	0.0011	0.282818	0.0000010	-1.49544
IP-5	111.45	0.512335	0.002	-5.9106	0.706055	0.0013	0.282709	0.0000053	-5.33479
l00-35	114.08	0.5123407	0.0016	-5.79941	0.707913	0.0008	0.282625	0.0000174	-8.31884
L05-1	115.30	0.512358	0.0025	-5.46194	0.706723	0.001	0.282832	0.0000158	-0.97937
SRP-2	115.00	0.512409	0.0019	-4.46709	0.70677	0.0008	0.282728	0.0000156	-4.6671

Isotopic ratios for Nd, Sr and Hf in basalts from the Yellowstone hotspot. The longitude at which each sample was collected is given as well. Nd and Sr isotopes were analyzed on a VG sector TIMS at the University of Michigan. Hf isotopes were analyzed on a Nu-Plasma multi-collector ICP-MS. Age corrections on all values were negligible

Table 3. $^{40}Ar/^{39}Ar$ dates for selected lavas from the Yellowstone hotspot

	total gas age	error	plateau age	error	mswd	% ^{39}Ar	isochron age all pts	error	mswd	Initial $^{40}Ar/^{36}Ar$	error	isochron age plateau pts	error	mswd	Initial $^{40}Ar/^{36}Ar$	error	pts
GR-1a	5.892	0.09	6.216	0.16	1.93	52.8	5.48	0.76	1.92	299.4	3.9	5.48	0.76	1.92	299.4	3.9	
GR-1a plag	11.102	0.35	11.223	0.28	0.73	100	11.53	0.4	0.7	291.7	3.6						
JD-4	17.56	0.08					16.84	0.31	18.6	337.4	13.3	16.03	0.13	1.11	403.7	8	8
JD-4 plag	18.46	0.94	17.71	0.77	0.68	100	17.47	0.74	1.12	297.6	6						
MG-1	8.503	0.07	8.524	0.07	1.5	100	8.51	0.13	1.63	296	3.9						
MG-4	12.274	0.06	12.481	0.06	1.79	84.3	12.64	0.07	1.31	288.1	1.6	12.63	0.11	1.59	288.4	4.5	11
MG-6	0.121	0.1	0.096	0.06	1.06	100	0.111	0.07	1.11	293.7	3.2						
JV-2	-0.006	0.03	0.015	0.2	0.81	100	0.035	0.03	0.7	290.2	3.7						
JV-7	0.3145	0.1	0.1613	0.08	1.23	100	0.103	0.08	0.94	307	5.8						
GTMF-2	0.193	0.1	0.16	0.1	1.21	100	0.157	0.08	0.98	303.5	3						
GTMF-7	0.075	0.08	0.076	0.07	0.84	100	-0.15	0.08	1.06	309.9	5.4						
IP-5	0.542	0.16	0.354	0.18	1.67	100	-0.205	0.3	1.19	319.3	10.6						
l00-35	1.279	0.08	1.461	0.08	1.55	86.56	1.749	0.11	1.35	287.2	1.8	1.656	0.13	1.26	290.2	2.9	10
SRP-2	-0.148	0.05	-0.133	0.07	2.01	85.6	0.239	0.12	1.34	286	3.3	0.166	0.18	1.55	287.7	4.3	8
SRP-2 plag	0.043	0.3	0.227	0.23	1	100	0.218	0.43	1.08	296.2	18.5						
L05-1	0.029	0.06	-0.019	0.08	1.34	64.8	0.34	0.1	2.49	290.9	2	0.148	0.12	0.9	292.7	1.7	5

$^{40}Ar/^{39}Ar$ dates for Yellowstone hotspot lavas. All ages given in Ma, errors are 1-σ

Chapter 5

Conclusions

This dissertation consists of three independent chapters which shed new light on various aspects relating to the role played by volatiles, particularly H_2O, in generation of the melts that formed the Columbia River Basalts (CRB) and Snake River Plain (SRP) basalts, both of which have been attributed to the Yellowstone hotspot. Chapter 2 presents new volatile, major oxide and trace element data for olivine-hosted melt inclusions from basalt samples taken across the (SRP), Yellowstone's hotspot track. Chapter 3 presents a similar dataset created for the Columbia River Basalt group (CRB), a magmatic province, which compared to the SRP, is much larger in size, has more evolved rock compositions, and – we hypothesized – might be more hydrous. The CRB is interpreted to be the result of the initial impingement of the mantle plume hypothesized to be the source of volcanism in the Yellowstone hotspot (e.g., Geist and Richards, 1993; Jordan et al., 2004; Nash et al., 2006). Chapter 4 presents new Sr, Nd and Hf isotopic analyses as well as $^{40}Ar/^{39}Ar$ dates for a

selected subset of basalt samples from the CRB and SRP, covering the entire Yellowstone hotspot, and relating these data to volatiles.

1. Volatile distribution throughout the Yellowstone hotspot track

The central conclusion of both chapters two and three is that high volatile concentrations, particularly that of H_2O, are recorded in lavas in both the SRP and the CRB. In all cases, these high H_2O concentrations are associated with the less differentiated melt inclusion compositions. This indicates a deeper, either lithospheric or lower crustal source for the volatiles. Furthermore, in both cases, these high-volatile contents are typical of basalts which have elevated Ba concentration and Ba/Th ratios. This implicates a subduction-related source for mantle hydration in the Pacific Northwest region. The best candidate for a source is the Farallon (now Juan de Fuca) Plate, which has been subducting off the west coast of North America for ~50 My, and has been responsible for a great deal of arc volcanism resulting presumably from mantle influenced by the down- going dehydrating slab (Feeley, 2003, Leeman et al., 2004).

2. Comparison of temporal distribution of H_2O between CRB and SRP lavas

The key difference between the observed distribution of H_2O within the two distinct parts of the Yellowstone hotspot track, the CRB and SRP, is temporal, if we assume that the minimum water values obtained are near the real pre-eruptive volatile contents of the magmas, which is a fair assumption for all but the main-eruptive-stage CRB basalts. In SRP lavas, the highest observed

H_2O concentrations were found in lavas in the Yellowstone-Henry's Fork caldera system, which is the currently active part of the Yellowstone hotspot. Young basalts covering older calderas in the SRP, termed post-caldera lavas, all had lower H_2O concentrations, which were interpreted in chapter 2 to be the result of melting residual mantle that had been dehydrated by the passage of earlier transient, plume-related melts. However, this interpretation is complicated by the observation in chapter 3 that in CRB lavas, the most H_2O-rich lavas were erupted late, well after the plume had moved out of the region. Although there is some sampling bias towards the late lavas, main-stage (earlier) CRB lavas are fairly evolved and so are poor in olivine phenocrysts. A very high H_2O concentration (4.2 wt%) was observed in one of the late (8.5 Ma) CRB lava flows, whereas an older flow (12.2 Ma) in the same area yielded only 1.29 wt% H_2O. This observation strengthens the conclusion that mantle hydration in the CRB source region(s) may have increased between ~17 Ma and 8.5 Ma, and then dropped off afterwards.

As it follows from above, the datasets for the CRB and SRP are best reconciled by considering their current proximity to the subducting slab. The CRB are located just east of the active Cascades arc, meaning that the ongoing contribution of volatiles to the mantle in this region throughout the history of the Yellowstone hotspot is possible. However, the SRP is now significantly further east of the modern arc, and therefore may not be continuing to receive a new influx of volatiles. In this case the passing plume would deplete residual

volatiles in the SRP, leaving late-erupted products more volatile poor, while a continuing influx of volatiles in the CRB region allowed high volatile contents in late lavas until much later after the plume had passed than in the case of the SRP.

Our original hypothesis for this work stated that volatile concentrations would tend to be higher in the CRB because of proximity to the subducting Farallon Plate and would drop off into the SRP. However, as can be seen in Fig. 5.1, this hypothesis is at best only weakly supported by the generated data. While the highest H_2O concentrations (up to 4.2 wt%) are generally found in the west, in the CRB region, the second highest H_2O concentration (up to 3.3 wt%) is in an SRP basalt on the far eastern end of the region, indicating that proximity to the modern subduction zone cannot be the sole major control of the volatile distribution across the Yellowstone hotspot.

3. Implications for the role of volatiles in the development of continental hotspots

The high-volatile concentrations observed in the Yellowstone hotspot are somewhat surprising considering that almost all values measured, even in less volatile-rich lavas, are higher than the maximum concentrations observed in basalts of the oceanic hotspots (e.g., Hawaii, 0.9 wt% H_2O, Hauri, 2002). Although the dataset for volatile concentrations in hotspots worldwide is limited, particularly in continental hotspots, an argument can be made that this initial observation may reflect a universal characteristic of continental hotspots.

The continents are made up of buoyant crustal blocks which have been preserved through geologic time. As a result of this, most continental masses have had a significantly more protracted and complex history than any piece of oceanic crust, and have endured one or more subduction events through their lifetime, making it much more likely to find residual hydration in mantle lithosphere or even lower crust than in oceanic lithosphere. Therefore, it is reasonable to expect that hotspots penetrating continental crust are much more likely to be contaminated with volatiles by interaction with the underlying mantle lithosphere/lower crust than will oceanic hotspots. Future work on volatiles in both oceanic and continental hotspots is absolutely necessary to test this hypothesis and better constrain the distribution of volatiles in the mantle. It should also be noted that while these findings can neither confirm nor refute the presence of the hypothesized Yellowstone plume, they do provide a way to understand why melting occurred where it did, and also whether or not the plume is present.

The results of this study underline the necessity of measuring volatile concentrations in a variety of settings, particularly those traditionally assumed to be anhydrous. It is the expectation of the author that volatiles are much more important influences on where and when the mantle melts than has been previously appreciated.

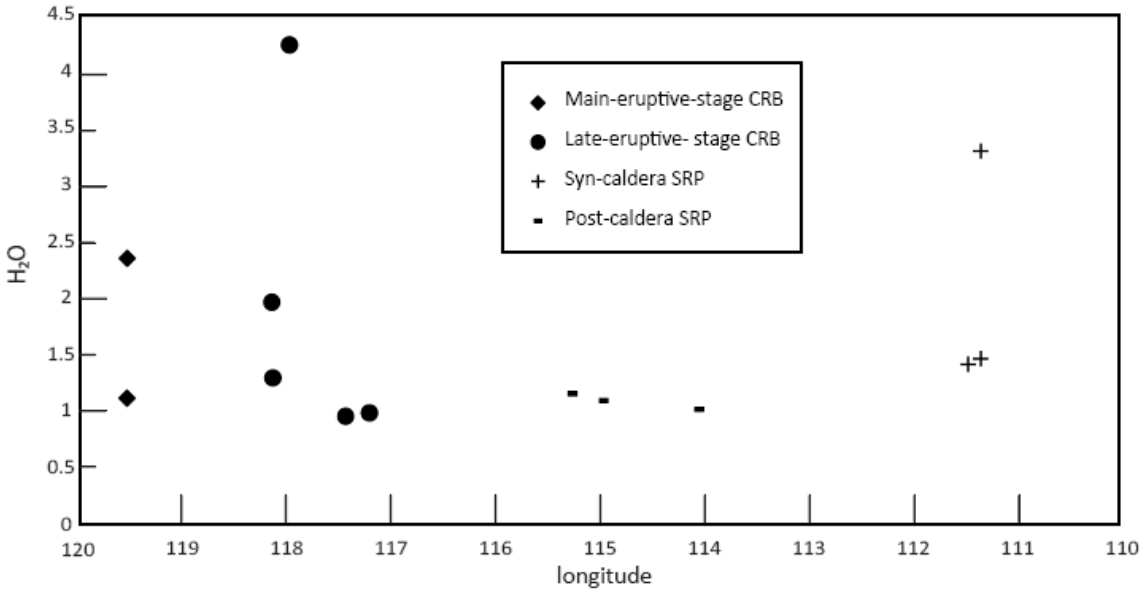

Figure 5.1. Plot of maximum H_2O concentration in olivine-hosted melt inclusions from the Yellowstone hotspot basalts. Although high-H_2O concentrations are observed at either end of the hotspot track, there is a general trend towards lower H_2O concentration eastward. As can be seen, the hypothesis that water should be more plentiful closer to the Cascades arc is at best only weakly supported.

References

Feeley, T. C. (2003). "Origin and tectonic implications of across-strike geochemical variations in the Eocene Absaroka volcanic province, United States." Journal of Geology 111(3): 329-346.

Geist, D. and M. Richards (1993). "Origin of the Columbia Plateau and Snake River plain; deflection of the Yellowstone plume." Geology 21(9): 789-792.

Hauri, E. (2002). "SIMS analysis of volatiles in silicate glasses, 2: isotopes and abundances in Hawaiian melt inclusions." Chemical Geology 183(1-4): 115-141.

Jordan, B. T., A. L. Grunder, et al. (2004). "Geochronology of age-progressive volcanism of the Oregon High Lava Plains: Implications for the plume interpretation of Yellowstone." Journal of Geophysical Research-Solid Earth 109(B10).

Leeman, W. P., S. Tonarini, et al. (2004). "Boron and lithium isotopic variations in a hot subduction zone - the southern Washington Cascades." Chemical Geology 212(1-2): 101-124.

Nash, B. P., M. E. Perkins, et al. (2006). "The Yellowstone hotspot in space and time: Nd and Hf isotopes in silicic magmas." Earth and Planetary Science Letters 247(1-2): 143-156.

Appendix A

Raw data tables for olivine-hosted melt inclusions used in this dissertation

TABLE A-1 Raw data for olivine-hosted melt inclusions used in this dissertation

wt%	JD-4-1a	JD-4-1b	JD-4-2	JD-4-3	JD-4-4	JD-4-5	JD-4-6
SiO_2	47.27	50.03	47.10	47.63	47.10	50.12	49.09
TiO_2	0.99	1.36	0.74	0.95	1.25	1.12	1.15
Al_2O_3	10.59	12.30	12.57	10.22	11.86	13.18	11.91
FeO	10.99	10.19	17.50	13.65	11.45	9.20	12.29
MnO	0.30	0.17	0.37	0.25	0.21	0.09	0.19
MgO	14.62	12.44	12.16	12.30	12.48	11.02	12.81
CaO	11.06	9.38	6.66	7.60	9.41	10.17	8.57
Na_2O	2.36	2.23	1.96	4.79	2.49	2.52	2.47
K_2O	0.40	0.45	0.13	0.56	0.46	0.48	0.46
P_2O_5	0.05	0.24	0.01	0.07	0.02	-0.01	0.12
H_2O	1.43	0.47	0.88	1.08	1.13	1.43	0.80
total	100.08	99.26	100.09	99.09	97.86	99.32	99.87
OH	1.60	1.20	1.04	0.73			1.21
ppm							
F	211.00	271.30	2084.60	481.70			294.70
S	490.00	418.00	1305.30	468.30			459.80
Cl	53.00	103.00	43.50	146.30			64.00
Sc	34.77	10.10	18.09	27.24		43.08	20.17
Rb	7.29	33.93	3.44	8.77		6.59	5.75
Sr	203.36	443.94	96.97	502.67		226.95	146.57
Y	25.36	23.59	12.08	15.85		31.47	12.53
Zr	90.49	134.14	43.08	90.04		100.60	53.24
Nb	5.01	24.13	2.32	14.37		4.75	3.79
Ba	208.66	580.37	101.74	194.13		265.75	97.82
La	7.52	22.12	3.59	8.29		7.54	5.28
Ce	18.01	49.96	8.68	20.74		18.08	11.80
Pr	2.31	6.23	1.20	2.43		2.43	1.37
Nd	11.17	24.23	5.22	14.68		12.41	7.39
Sm	2.88	5.61	1.92	3.18		4.95	2.57
Eu	1.12	2.81	0.74	1.21		1.53	1.07
Gd	3.77	4.89	2.04	4.41		4.51	2.34
Dy	5.02	3.49	2.61	2.83		6.69	2.69
Er	3.44	2.49	1.24	1.22		3.50	1.02
Yb	2.76	1.40	1.18	1.84		4.48	1.27
Th	0.82	4.15	0.29	0.77		0.49	0.44
U	0.36	1.33	0.14				0.16

Major oxides measured using EMPA, H_2O via FT-IR, volatiles (OH, F, S, Cl) by SIMS, and trace elements by LA-ICP-MS

TABLE A-1 cont.

wt%	JD-4-7	JD-4-8	JD-4-10	JD-4-11	GR-1a-1	GR-1a-2
SiO_2	48.35	47.97	49.63	49.31	41.15	47.24
TiO_2	1.38	1.75	1.25	1.36	2.45	1.90
Al_2O_3	12.12	11.18	13.20	13.08	12.11	9.56
FeO	14.21	15.04	9.74	10.90	18.23	11.74
MnO	0.24	0.28	0.17	0.16	0.35	0.28
MgO	9.26	8.84	10.75	10.48	11.93	12.24
CaO	9.11	9.40	9.79	10.47	7.06	10.42
Na_2O	2.57	2.40	2.69	2.76	3.31	5.62
K_2O	0.45	0.49	0.48	0.46	0.38	0.50
P_2O_5	0.11	0.20	0.06	-0.03	0.34	0.39
H_2O	1.05	1.53	1.12	0.92	1.10	0.69
total	98.86	99.09	98.89	99.89	98.42	100.58
OH					0.83	
ppm						
F					404.50	
S					209.00	
Cl					204.40	
Sc		32.66	31.05	28.10	12.87	
Rb		7.39	10.11	9.24	7.54	
Sr		212.09	215.76	225.37	174.42	
Y		25.74	25.21	26.21	13.06	
Zr		96.00	88.73	88.25	97.31	
Nb		6.18	6.74	6.44	15.80	
Ba		233.74	246.37	255.68	194.88	
La		8.26	8.14	7.13	8.86	
Ce		20.90	21.87	22.29	25.00	
Pr		2.86	2.42	2.65	2.68	
Nd		14.53	11.52	12.66	11.41	
Sm		5.09	4.54	3.46	2.27	
Eu		1.68	1.08	1.17	0.80	
Gd		5.73	2.35	3.68	2.53	
Dy		4.70	4.87	4.19	2.46	
Er		2.97	2.65	2.73	1.08	
Yb		2.39	2.08	2.76	1.34	
Th		0.72	0.76	0.63	0.67	
U		0.41	0.47	0.37	0.12	

Major oxides measured using EMPA, H_2O via FT-IR, volatiles (OH, F, S, Cl) by SIMS, and trace elements by LA-ICP-MS

TABLE A-1 cont.

wt%	GR-1a-5	GR-1a-6	GR-1a-7	GR-1a-8	GR-1a-9	GR-1a-10	GR-1a-11
SiO_2	50.09	48.24	48.03	53.98	54.99	50.34	49.96
TiO_2	1.16	0.91	1.03	1.24	0.74	0.96	0.08
Al_2O_3	22.85	24.99	24.67	23.00	22.63	23.49	29.72
FeO	5.81	5.20	5.48	4.64	3.87	5.47	0.67
MnO	0.08	0.14	0.09	0.08	0.04	0.10	0.01
MgO	4.01	3.21	2.92	0.57	0.26	3.65	0.17
CaO	12.15	12.38	12.54	9.52	8.66	11.35	12.93
Na_2O	2.79	3.39	3.67	4.59	4.96	3.20	4.13
K_2O	0.56	0.69	0.61	1.37	1.77	0.84	0.32
P_2O_5	0.29	0.22	0.25	0.21	0.20	0.25	-0.02
H_2O	0.66	0.81	0.68	0.63	0.86	0.60	0.62
total	100.45	100.19	99.97	99.85	98.97	100.26	98.61
OH		0.17		0.61	0.78		
ppm							
F		113.20		383.10	569.10		
S		75.00		493.20	235.70		
Cl		662.60		94.90	102.10		
Sc	12.87		10.98	12.02	11.76	10.30	
Rb	7.83	2.96	9.81	23.91	28.33	7.18	
Sr	334.43	341.56	360.62	356.24	383.19	332.99	
Y	17.85	4.43	17.35	13.34	51.25	10.40	
Zr	98.86	27.49	91.25	72.20	249.08	58.53	
Nb	12.95	3.26	11.72	8.82	34.93	8.67	
Ba	364.71	184.79	331.52	346.77	544.00	266.44	
La	19.49	6.19	17.46	13.28	66.12	11.31	
Ce	48.32	14.55	40.15	32.33	160.24	25.76	
Pr	5.20	1.59	4.58	3.57	17.89	3.35	
Nd	19.70	6.53	17.14	14.82	72.21	9.99	
Sm	4.15	1.48	3.74	3.18	11.05	2.31	
Eu	1.71	0.67	1.62	1.30	3.36	0.79	
Gd	5.68		3.56	2.46	11.42	2.10	
Dy	2.50	0.96	2.90	2.83	8.73	1.61	
Er	1.26		2.05	1.60	6.41	1.10	
Yb	1.99		1.93	0.93	5.08	0.69	
Th	0.56		0.97	2.93	11.37	0.32	
U	0.21		0.35	0.89	4.46	0.09	

Major oxides measured using EMPA, H_2O via FT-IR, volatiles (OH, F, S, Cl) by SIMS, and trace elements by LA-ICP-MS

TABLE A-1 cont.

wt%	GR-1a-12	JV-2-2	JV-2-3	JV-2-4	JV-2-5	JV-2-6
SiO_2	48.44	46.84	46.66	47.17	47.28	46.95
TiO_2	0.03	1.94	1.84	1.95	2.09	1.95
Al_2O_3	31.93	16.50	16.30	16.00	15.67	15.73
FeO	0.42	9.04	8.95	9.77	10.04	8.99
MnO	0.02	0.16	0.17	0.14	0.16	0.12
MgO	0.20	10.19	11.66	10.69	10.87	11.12
CaO	15.23	8.93	8.90	8.80	8.78	8.83
Na_2O	2.89	3.14	3.28	3.07	3.61	4.08
K_2O	0.17	1.20	1.24	1.17	1.36	1.40
P_2O_5	0.04	0.48	0.43	0.46	0.43	0.41
H_2O	0.50	0.51	0.69	0.23	0.34	0.60
total	99.88	98.93	100.12	99.45	100.65	100.17
OH	0.73	0.77	0.61			
ppm						
F	985.00	546.50	564.90			
S	420.50	863.90	849.80			
Cl	159.00	294.80	306.70			
Sc	14.87	16.68	20.84		21.81	21.22
Rb	18.69	24.49	29.24		31.21	30.57
Sr	409.05	528.73	513.75		472.65	493.51
Y	10.56	16.26	18.99		20.02	20.28
Zr	64.87	131.69	134.62		134.23	135.52
Nb	7.36	42.60	40.53		40.46	40.59
Ba	399.76	350.39	361.25		388.66	397.84
La	11.15	17.40	17.77		18.94	18.94
Ce	25.74	43.26	44.08		47.42	46.84
Pr	2.85	4.67	5.11		5.65	5.65
Nd	12.04	19.92	21.48		21.25	20.95
Sm	3.02	4.51	4.26		3.95	4.35
Eu	0.64	1.65	1.52		1.86	1.87
Gd	2.41	4.62	4.44		3.39	4.39
Dy	2.13	3.07	3.89		3.46	2.74
Er	1.49	2.04	1.26		1.63	1.80
Yb		1.42	1.76		1.64	1.71
Th	0.43	1.43	1.39		1.55	1.63
U	0.36	0.69	0.78		0.75	0.76

Major oxides measured using EMPA, H_2O via FT-IR, volatiles (OH, F, S, Cl) by SIMS, and trace elements by LA-ICP-MS

TABLE A-1 cont.

wt%	JV-2-7	JV-2-9	JV-7-1	JV-7-2	JV-7-4	JV-7-5
SiO_2	47.18	46.69	43.22	45.54	45.31	46.27
TiO_2	1.95	1.51	3.25	2.56	2.08	2.03
Al_2O_3	15.95	14.55	11.95	13.02	14.87	15.84
FeO	9.38	10.44	14.08	12.79	10.08	9.45
MnO	0.11	0.22	0.30	0.25	0.17	0.13
MgO	11.33	11.32	11.31	11.20	12.13	12.02
CaO	8.90	7.70	7.49	8.33	9.09	9.66
Na_2O	3.09	3.94	4.64	4.38	2.89	3.13
K_2O	1.20	1.22	0.95	0.80	0.68	0.68
P_2O_5	0.41	0.36	0.75	0.39	0.32	0.35
H_2O	0.52	0.76	0.94	0.67	0.48	0.58
total	100.03	98.71	98.88	99.94	98.11	100.13
OH		0.98			0.58	0.00
ppm						
F		439.80			438.10	0.00
S		61.20			974.10	104.70
Cl		74.50			333.60	13.90
Sc	17.66			32.05		31.74
Rb	27.21			25.08		7.64
Sr	515.92			469.43		204.14
Y	17.53			26.14		25.00
Zr	124.13			149.47		94.81
Nb	40.81			31.17		5.92
Ba	356.99			326.49		219.54
La	17.27			17.17		8.12
Ce	44.46			46.09		17.85
Pr	5.14			6.00		2.57
Nd	18.96			26.13		11.27
Sm	4.27			6.19		3.46
Eu	1.68			1.94		1.36
Gd	4.82			6.48		4.29
Dy	3.72			4.74		4.85
Er	1.52			2.57		2.90
Yb	1.81			2.70		2.85
Th	1.31			1.38		0.82
U	0.67			0.73		0.33

Major oxides measured using EMPA, H_2O via FT-IR, volatiles (OH, F, S, Cl) by SIMS, and trace elements by LA-ICP-MS

TABLE A-1 cont.

wt%	JV-7-6	JV-7-7	MG-1-2	MG-1-3	MG-1-5	MG-1-6
SiO_2	46.52	45.63	42.75	42.56	46.30	41.71
TiO_2	2.19	3.61	1.84	1.85	1.68	1.13
Al_2O_3	16.10	9.00	10.08	10.32	13.52	14.88
FeO	8.86	15.27	16.10	14.99	13.79	16.82
MnO	0.17	0.24	0.24	0.23	0.25	0.28
MgO	11.42	11.38	14.88	15.05	12.19	11.61
CaO	9.49	8.95	9.10	9.91	7.27	9.44
Na_2O	3.89	4.08	1.56	1.46	2.67	2.04
K_2O	0.69	1.36	0.46	0.42	0.68	0.46
P_2O_5	0.44	0.65	0.16	0.26	0.33	0.25
H_2O	0.52	0.74	2.64	3.25	1.26	1.83
total	100.29	100.92	99.82	100.30	99.95	100.46
OH			3.30	4.23	1.45	
ppm						
F			421.00	591.20	578.90	
S			2063.40	2340.60	351.40	
Cl			147.10	92.70	95.90	
Sc	20.55			23.74	14.73	14.03
Rb	12.68			3.42	6.65	5.23
Sr	637.60			198.16	222.40	272.99
Y	15.81			25.67	25.28	28.96
Zr	93.54			154.36	150.46	159.64
Nb	19.58			7.62	12.33	10.01
Ba	252.91			264.00	518.33	561.14
La	10.36			10.73	14.30	18.95
Ce	28.53			25.72	32.80	39.01
Pr	3.53			3.60	3.95	5.06
Nd	13.83			18.44	17.59	21.05
Sm	3.20			4.78	3.81	4.72
Eu	1.67			1.57	1.62	1.49
Gd	4.22			4.48	3.52	5.08
Dy	3.08			4.81	3.67	4.32
Er	1.16			2.76	2.50	2.19
Yb	1.89			3.23	2.34	2.61
Th	0.66			0.42	0.49	0.61
U	0.22			0.14	0.25	0.27

Major oxides measured using EMPA, H_2O via FT-IR, volatiles (OH, F, S, Cl) by SIMS, and trace elements by LA-ICP-MS

TABLE A-1 cont.

wt%	MG-1-7	MG-1-8	MG-1-9	MG-4-1	MG-4-2	MG-4-3
SiO_2	47.39	45.11	43.67	47.34	48.09	46.63
TiO_2	2.02	1.85	2.64	1.83	1.78	1.85
Al_2O_3	13.71	10.91	10.02	13.76	13.66	14.24
FeO	9.80	15.09	18.91	12.80	12.56	12.00
MnO	0.14	0.22	0.32	0.27	0.23	0.32
MgO	11.91	10.81	9.42	11.08	10.62	12.16
CaO	9.81	10.27	9.30	8.24	8.53	8.00
Na_2O	2.38	4.37	2.77	2.61	2.56	2.69
K_2O	0.72	0.26	0.46	0.81	0.87	0.86
P_2O_5	0.29	0.22	0.83	0.13	0.07	0.51
H_2O	0.81	0.83	0.96	0.66	0.81	0.63
total	98.97	99.94	99.31	99.53	99.77	99.88
OH	0.63	1.23				
ppm						
F	326.80	515.60				
S	470.20	1425.20				
Cl	49.10	286.20				
Sc	34.93		34.64		21.78	
Rb	7.63		8.55		12.92	
Sr	234.11		290.39		375.22	
Y	33.10		46.80		26.46	
Zr	196.18		248.68		137.69	
Nb	12.56		17.87		17.35	
Ba	451.17		1604.75		631.98	
La	16.25		26.01		22.64	
Ce	39.08		55.34		63.21	
Pr	4.90		7.27		7.17	
Nd	22.56		29.38		28.72	
Sm	5.53		6.92		7.36	
Eu	2.05		2.12		2.22	
Gd	5.44		9.17		6.97	
Dy	4.85		7.43		5.27	
Er	4.12		3.69		2.40	
Yb	2.54		3.04		2.29	
Th	0.62		0.92		0.77	
U	0.30		0.36		0.41	

Major oxides measured using EMPA, H_2O via FT-IR, volatiles (OH, F, S, Cl) by SIMS, and trace elements by LA-ICP-MS

TABLE A-1 cont.

wt%	MG-4-4	MG-4-5	MG-4-8	MG-4-9	MG-4-11	MG-4-12
SiO_2	47.51	46.80	44.61	46.59	48.37	49.15
TiO_2	1.77	1.67	1.81	1.87	2.05	1.29
Al_2O_3	13.66	13.75	13.53	14.21	16.78	7.24
FeO	12.47	12.79	16.39	15.38	13.63	21.46
MnO	0.23	0.23	0.23	0.20	0.23	0.36
MgO	11.27	12.96	11.26	11.62	7.81	8.21
CaO	8.06	7.93	8.17	8.13	8.18	7.23
Na_2O	2.57	2.58	2.37	2.71	3.46	5.37
K_2O	0.91	0.85	0.76	0.86	1.01	0.63
P_2O_5	0.00	0.19	0.38	0.47	0.51	0.64
H_2O	0.96	0.89	0.79	0.80	0.67	1.33
total	99.41	100.64	100.30	102.85	102.69	102.89
OH						
ppm						
F						
S						
Cl						
Sc	26.19		22.70	21.75		21.31
Rb	11.57		11.60	10.88		3.84
Sr	363.45		366.11	380.01		146.45
Y	28.78		25.83	26.67		18.48
Zr	146.44		131.75	133.61		106.67
Nb	16.78		17.25	17.17		6.22
Ba	583.07		580.52	563.64		228.79
La	21.42		21.69	23.65		6.81
Ce	56.82		58.50	61.90		19.28
Pr	6.33		6.64	7.18		2.69
Nd	28.25		24.91	28.73		12.56
Sm	6.29		4.70	6.21		3.51
Eu	2.11		1.75	1.98		1.01
Gd	5.65		5.49	5.83		4.69
Dy	4.68		4.92	5.00		3.28
Er	2.70		2.33	2.20		2.28
Yb	2.49		2.06	2.19		2.13
Th	1.02		0.79	1.12		0.17
U	0.27		0.31	0.29		0.21

Major oxides measured using EMPA, H_2O via FT-IR, volatiles (OH, F, S, Cl) by SIMS, and trace elements by LA-ICP-MS

TABLE A-1 cont.

wt%	MG-6-1	MG-6-3	MG-6-4	MG-6-5	MG-6-6	MG-6-7	MG-6-8
SiO_2	49.80	45.50	46.08	47.11	47.45	44.02	46.70
TiO_2	1.12	0.89	1.02	0.74	0.82	1.03	1.01
Al_2O_3	13.69	14.77	15.10	14.28	14.11	11.24	15.16
FeO	12.09	9.02	10.41	10.25	11.44	11.65	14.70
MnO	0.18	0.19	0.13	0.12	0.27	0.22	0.29
MgO	11.73	13.14	11.57	12.45	12.60	12.46	11.05
CaO	7.43	12.24	9.66	10.37	8.95	13.58	7.01
Na_2O	3.59	2.64	3.50	2.46	3.08	3.59	3.31
K_2O	0.60	0.29	0.43	0.36	0.39	0.45	0.50
P_2O_5	0.03	0.10	0.09	0.13	0.06	0.07	0.04
H_2O	1.08	1.30	1.30	1.81	0.88	1.30	0.98
total	101.34	100.09	99.28	100.08	100.04	99.61	100.76
OH					0.96		1.10
ppm							
F					100.60		119.50
S					22.00		104.40
Cl					38.00		52.80
Sc	30.60	23.71	22.45	26.36	29.22	34.82	25.47
Rb	10.97	4.05	5.68	8.73	3.98	6.15	7.08
Sr	176.71	228.85	154.91	154.09	160.19	216.84	178.58
Y	21.39	36.86	22.69	15.56	14.51	31.27	17.34
Zr	95.30	53.38	86.20	68.01	51.49	63.95	72.11
Nb	4.91	2.90	5.55	3.42	2.71	3.00	3.81
Ba	192.37	117.34	64.26	65.82	119.39	151.75	166.07
La	6.02	5.22	6.31	2.54	3.62	5.29	4.97
Ce	17.75	14.79	19.09	8.83	10.98	14.39	11.37
Pr	2.27	1.85	2.60	1.22	1.52	1.94	1.42
Nd	10.67	8.31	12.67	6.53	7.91	9.66	6.74
Sm	3.43	2.41	2.89	1.65	1.42	2.78	2.23
Eu	1.05	1.18	1.01	0.64	0.60	1.26	0.95
Gd	3.33	3.47	2.99	2.00	2.25	3.52	2.89
Dy	3.73	4.71	4.71	1.69	3.72	4.10	2.81
Er	2.25	3.81	2.29	1.20	1.64	3.51	1.87
Yb	2.50	3.71	2.53	1.61	1.32	3.94	1.74
Th	0.42	0.34	0.19			0.45	0.43
U	0.18	0.77	0.13	0.11		1.83	

Major oxides measured using EMPA, H_2O via FT-IR, volatiles (OH, F, S, Cl) by SIMS, and trace elements by LA-ICP-MS

TABLE A-1 cont.

wt%	MG-6-9	MG-6-10	L05-1-2	L05-1-3	L05-1-4	L05-1-5
SiO_2	45.77	45.47	45.29	47.19	45.39	46.08
TiO_2	0.68	0.83	2.12	2.01	2.16	2.03
Al_2O_3	14.11	15.38	13.94	14.96	14.01	14.50
FeO	13.95	10.43	10.33	10.18	10.23	10.76
MnO	0.25	0.16	0.18	0.20	0.13	0.16
MgO	11.75	13.14	11.72	12.09	11.03	11.16
CaO	8.14	10.59	9.76	9.72	10.20	10.03
Na_2O	2.57	2.03	2.73	2.81	2.54	2.42
K_2O	0.47	0.32	0.62	0.54	0.63	0.59
P_2O_5	0.04	0.09	0.60	0.47	0.70	0.44
H_2O	1.42	1.30		0.21	0.46	0.64
total	99.15	99.74	97.28	100.38	97.47	98.82
OH	1.38	1.30		0.34		
ppm						
F	109.80	134.00		654.40		
S	406.60	443.30		775.80		
Cl	86.90	31.00		106.20		
Sc		25.94		22.48		
Rb		6.08		9.94		
Sr		160.01		324.54		
Y		16.94		29.60		
Zr		92.46		191.78		
Nb		3.23		18.67		
Ba		86.05		381.78		
La		3.46		20.79		
Ce		10.06		52.74		
Pr		1.39		5.85		
Nd		6.34		28.62		
Sm		2.40		6.63		
Eu		0.88		2.17		
Gd		2.40		5.45		
Dy		3.30		4.23		
Er		1.97		3.29		
Yb		2.97		2.16		
Th				0.91		
U		0.13		0.33		

Major oxides measured using EMPA, H_2O via FT-IR, volatiles (OH, F, S, Cl) by SIMS, and trace elements by LA-ICP-MS

TABLE A-1 cont.

wt%	L05-1-6	L05-1-7	L05-1-8	L05-1-10	L05-1-12	L05-1-13
SiO_2	46.66	46.38	51.20	47.48	47.99	50.08
TiO_2	2.06	2.26	1.87	3.28	2.05	1.60
Al_2O_3	14.65	10.90	13.73	11.33	15.45	14.75
FeO	10.09	18.91	9.58	9.81	8.64	7.92
MnO	0.15	0.31	0.16	0.18	0.14	0.15
MgO	11.55	9.42	9.26	12.13	12.82	11.38
CaO	9.90	5.61	8.93	9.37	9.21	8.43
Na_2O	2.68	3.09	2.73	2.88	2.91	3.04
K_2O	0.65	1.31	0.86	1.14	0.66	1.39
P_2O_5	0.50	0.92	0.55	1.05	0.68	0.40
H_2O	0.37	0.64	0.28	0.52	0.56	0.50
total	99.27	99.75	99.16	99.17	101.10	99.63
OH		0.97				
ppm						
F		1226.00				
S		405.00				
Cl		315.60				
Sc	20.04	19.13			18.18	17.00
Rb	11.72	24.22			10.34	38.67
Sr	332.77	231.07			314.04	371.11
Y	25.55	36.79			23.20	23.11
Zr	179.81	291.82			171.38	155.78
Nb	20.19	27.01			18.51	22.53
Ba	398.13	574.78			379.11	531.84
La	20.09	30.13			19.60	30.83
Ce	57.73	77.81			54.59	78.12
Pr	6.85	8.78			5.73	8.10
Nd	27.27	34.46			26.15	30.95
Sm	5.95	7.73			5.00	5.61
Eu	2.42	2.60			2.15	1.69
Gd	4.52	6.72			4.74	5.39
Dy	6.07	6.27			5.56	5.70
Er	2.29	3.61			2.51	2.52
Yb	2.71	3.81			1.75	2.20
Th	0.52	2.13			0.67	4.72
U	0.37	0.66			0.33	0.99

Major oxides measured using EMPA, H_2O via FT-IR, volatiles (OH, F, S, Cl) by SIMS, and trace elements by LA-ICP-MS

TABLE A-1 cont.

wt%	L00-35-3	L00-35-4	L00-35-5	L00-35-6	L00-35-8	L00-35-9	L00-35-10
SiO_2	46.66	42.22	38.86	47.26	45.83	47.55	47.22
TiO_2	2.29	4.06	-0.01	1.06	2.05	2.72	2.50
Al_2O_3	12.63	11.90	0.06	11.86	12.71	14.22	13.36
FeO	11.83	16.14	18.98	16.54	17.03	11.12	10.61
MnO	0.26	0.27	0.23	0.40	0.26	0.21	0.17
MgO	11.09	11.58	42.43	9.02	8.69	8.96	10.53
CaO	9.88	7.73	0.27	5.07	8.74	10.08	10.36
Na_2O	2.36	1.99	0.00	4.70	4.48	2.68	2.53
K_2O	0.79	0.62	0.01	1.05	0.28	0.91	0.83
P_2O_5	0.58	0.77	-0.03	0.80	0.36	0.51	0.51
H_2O	0.23	0.23	0.21	0.08	1.00	0.58	0.47
total	98.59	97.53	101.00	97.84	101.44	99.54	99.09
OH		0.53				0.42	
ppm							
F		430.70				55.00	
S		91.10				172.90	
Cl		540.50				16.10	
Sc	26.16	37.75			74.29	25.73	24.31
Rb	19.51	10.20			4.62	19.08	19.55
Sr	309.45	280.87			263.82	309.40	313.80
Y	28.95	39.07			30.47	27.25	29.13
Zr	176.83	161.30			163.20	180.04	178.91
Nb	18.03	21.82			15.89	17.20	18.95
Ba	472.19	422.65			367.20	463.71	473.83
La	20.52	27.06			23.32	20.82	20.32
Ce	56.56	68.23			64.06	56.55	58.86
Pr	6.29	8.63			4.72	6.77	6.66
Nd	28.93	38.76			18.20	27.49	29.94
Sm	6.41	9.34			5.52	4.55	6.61
Eu	1.73	2.55			1.92	2.30	2.32
Gd	6.17	7.70			4.12	6.30	5.01
Dy	5.73	7.34			5.63	4.70	4.25
Er	2.29	4.32			3.36	2.96	2.72
Yb	2.17	3.96			1.13	1.71	2.52
Th	1.56	1.42			1.46	1.92	1.37
U	0.33	0.22			0.62	0.52	0.33

Major oxides measured using EMPA, H_2O via FT-IR, volatiles (OH, F, S, Cl) by SIMS, and trace elements by LA-ICP-MS

TABLE A-1 cont.

wt%	L00-35-11	L00-35-13	SRP-2-1	SRP-2-3	SRP-2-4	SRP-2-5
SiO_2	47.48	46.63	44.93	44.80	47.71	46.53
TiO_2	2.37	2.59	3.07	3.01	2.81	3.10
Al_2O_3	13.32	12.68	12.10	12.15	11.78	11.31
FeO	11.21	11.66	17.51	17.16	13.94	13.87
MnO	0.26	0.23	0.27	0.21	0.18	0.24
MgO	11.27	8.86	11.35	11.29	11.19	10.98
CaO	9.95	10.63	8.33	8.55	7.99	8.69
Na_2O	2.48	2.50	2.36	2.52	2.45	2.39
K_2O	0.81	0.78	0.78	0.75	0.93	0.80
P_2O_5	0.54	0.51	0.61	0.43	0.72	0.57
H_2O	0.49	0.49	0.21	0.22	0.32	0.24
total	100.17	97.56	101.52	101.08	100.01	98.73
OH			0.30			
ppm						
F			825.90			
S			967.90			
Cl			70.30			
Sc			29.55	25.85	24.91	25.56
Rb			17.03	18.32	22.10	17.86
Sr			262.93	275.04	256.18	280.63
Y			31.34	36.84	33.67	36.48
Zr			228.00	233.03	252.45	249.54
Nb			22.09	22.33	23.91	23.16
Ba			437.07	442.23	459.20	442.64
La			24.54	24.86	26.01	24.94
Ce			61.49	66.63	64.08	64.52
Pr			7.54	8.17	7.86	8.43
Nd			33.62	31.60	33.23	35.26
Sm			5.62	7.15	7.85	8.92
Eu			2.33	2.80	2.72	3.02
Gd			7.42	6.72	6.81	8.20
Dy			6.21	5.90	7.10	6.67
Er			3.57	3.34	3.61	3.72
Yb			3.14	3.10	2.90	4.23
Th			1.80	2.16	2.61	1.49
U			0.68	0.64	0.80	0.68

Major oxides measured using EMPA, H_2O via FT-IR, volatiles (OH, F, S, Cl) by SIMS, and trace elements by LA-ICP-MS

TABLE A-1 cont.

wt%	SRP-2-6	SRP-2-7	SRP-2-8	SRP-2-9	SRP-2-13	SRP-2-16	SRP-2-17
SiO_2	46.16	46.30	47.06	46.22	43.66	46.90	45.63
TiO_2	3.46	3.14	2.19	3.03	2.95	2.83	3.07
Al_2O_3	11.54	11.27	12.51	11.75	11.43	11.35	10.85
FeO	14.45	14.58	13.55	15.19	16.99	14.68	15.02
MnO	0.20	0.27	0.26	0.24	0.22	0.21	0.30
MgO	10.26	10.67	12.08	10.97	10.38	11.94	12.54
CaO	8.66	8.15	8.53	8.73	7.82	8.22	8.08
Na_2O	2.35	2.32	1.97	2.56	2.49	2.01	2.07
K_2O	0.78	0.80	1.12	0.72	0.81	0.72	0.73
P_2O_5	0.39	0.43	0.70	0.75	0.64	0.55	0.56
H_2O	0.25	0.29	0.25	0.20	0.52	0.81	0.56
total	98.48	98.21	100.21	100.35	97.92	100.22	99.40
OH			0.23			0.99	
ppm							
F			977.20			862.90	
S			727.00			926.50	
Cl			93.20			77.40	
Sc	28.31	26.92	26.23	27.36	24.49		28.56
Rb	17.80	17.55	17.36	17.86	19.91		16.51
Sr	275.06	257.38	253.85	265.10	268.96		243.95
Y	40.41	36.34	34.64	35.49	34.00		35.86
Zr	258.00	242.29	237.35	258.78	221.77		240.48
Nb	22.53	21.47	19.34	21.53	21.17		21.39
Ba	441.94	421.73	409.60	443.91	440.01		416.76
La	25.49	25.49	23.81	26.11	24.03		23.01
Ce	65.63	63.80	57.46	67.18	62.14		61.79
Pr	8.48	7.76	7.56	7.62	7.51		7.70
Nd	33.68	31.77	30.42	34.89	30.93		33.02
Sm	7.42	7.55	8.12	7.46	6.32		6.93
Eu	2.89	2.74	2.54	2.32	2.62		2.56
Gd	7.95	7.35	7.14	8.31	7.03		8.62
Dy	7.31	6.20	7.29	7.58	6.13		6.05
Er	4.28	4.22	3.28	3.52	2.88		3.58
Yb	2.69	3.54	2.74	3.93	3.21		3.85
Th	2.07	1.75	2.15	1.97	1.20		1.91
U	0.78	0.63	0.51	0.70	0.67		0.67

Major oxides measured using EMPA, H_2O via FT-IR, volatiles (OH, F, S, Cl) by SIMS, and trace elements by LA-ICP-MS

TABLE A-1 cont.

wt%	AYS-1	AYS-2	AYS-4	AYS-5	AYS-6	AYS-7	AYS-8
SiO_2	47.43	47.51	39.95	47.43	46.51	47.70	46.71
TiO_2	1.05	1.17	1.24	1.31	1.14	1.08	0.98
Al_2O_3	13.93	14.84	15.44	15.29	14.38	14.63	13.43
FeO	10.62	10.48	11.22	10.22	11.06	10.45	12.05
MnO	0.19	0.22	0.22	0.22	0.24	0.20	0.21
MgO	11.49	11.19	8.66	10.10	11.72	10.25	9.72
CaO	11.23	11.34	11.62	11.91	11.23	11.68	10.79
Na_2O	2.10	2.37	9.48	2.38	2.03	2.39	1.63
K_2O	0.18	0.16	0.43	0.14	0.14	0.18	0.11
P_2O_5	0.11	0.15	0.14	0.02	0.16	0.12	0.08
H_2O	0.73	0.55	1.17	0.55	0.33	0.60	0.61
total	99.06	99.97	99.56	99.56	98.94	99.30	96.33
OH	0.56	0.57	1.66		0.46		
ppm							
F	106.10	131.80	90.60		79.30		
S	881.20	805.60	1542.10		538.30		
Cl	55.70	19.50	388.80		19.00		
Sc		41.92	30.63	31.30	37.15	29.47	41.30
Rb		1.65	3.09	1.53	1.55	1.35	1.47
Sr		168.90	149.26	193.08	169.53	202.24	180.78
Y		16.03	26.05	17.17	14.55	16.40	16.73
Zr		55.36	65.09	57.53	55.72	53.71	55.77
Nb		3.36	3.81	3.83	2.84	3.50	3.39
Ba		112.53	2148.64	124.99	110.31	125.56	128.69
La		3.85	12.42	4.65	3.44	4.50	4.14
Ce		11.26	10.96	12.53	10.89	13.13	12.59
Pr		1.38	3.79	1.69	1.46	1.45	1.49
Nd		7.56	15.80	8.31	5.86	8.60	8.51
Sm		1.86	4.66	2.78	1.85	2.26	1.70
Eu		0.75	0.82	0.98	1.17	1.11	0.97
Gd		1.90	5.56	2.69	2.73	2.82	1.96
Dy		4.00	5.39	2.48	3.15	2.47	4.29
Er		1.54	3.96	2.06	1.83	2.28	1.72
Yb		1.29	3.68	1.69	1.92	1.47	1.58
Th			0.83	0.17			
U			0.10				

Major oxides measured using EMPA, H_2O via FT-IR, volatiles (OH, F, S, Cl) by SIMS, and trace elements by LA-ICP-MS

TABLE A-1 cont.

wt%	AYS-9	OS-1	OS-2	OS-3	OS-5	OS-6
SiO_2	47.66	48.83	45.48	39.19	47.94	48.31
TiO_2	1.15	1.57	1.11	2.07	0.99	1.19
Al_2O_3	16.02	13.71	13.63	14.72	14.23	15.04
FeO	9.49	11.84	11.58	16.52	10.50	10.66
MnO	0.19	0.12	0.21	0.28	0.19	0.22
MgO	9.96	9.38	11.10	7.56	13.01	10.92
CaO	11.68	9.73	11.40	9.21	10.27	11.08
Na_2O	2.57	3.18	2.04	8.06	2.20	2.10
K_2O	0.16	0.42	0.22	0.09	0.23	0.20
P_2O_5	0.17	0.25	0.05	0.25	0.08	0.08
H_2O	0.68	0.41	0.54	0.52	0.44	0.20
total	99.72	99.44	97.36	98.47	100.09	99.99
OH			0.77			
ppm						
F			164.00			
S			703.60			
Cl			24.40			
Sc	30.23		99.70		28.27	
Rb	1.33		6.27		4.93	
Sr	190.55		150.71		173.52	
Y	16.33		20.08		16.23	
Zr	49.48		71.79		52.01	
Nb	3.25		3.04		4.29	
Ba	128.63		167.21		141.65	
La	4.52		4.87		5.19	
Ce	12.63		12.67		13.71	
Pr	1.83		1.25		1.51	
Nd	8.07		5.75		6.93	
Sm	2.41				2.35	
Eu	0.94		1.30		0.95	
Gd	3.67				2.73	
Dy	2.98		3.21		2.93	
Er	1.65				1.38	
Yb	1.07				1.24	
Th					0.72	
U					0.18	

Major oxides measured using EMPA, H_2O via FT-IR, volatiles (OH, F, S, Cl) by SIMS, and trace elements by LA-ICP-MS

TABLE A-1 cont.

wt%	OS-7	OS-8	OS-10	OS-11	OS-12	OS-13
SiO_2	37.47	38.63	47.31	46.60	47.87	48.25
TiO_2	1.64	0.07	1.09	1.27	1.10	1.09
Al_2O_3	15.78	0.47	14.86	16.60	15.38	15.48
FeO	13.96	13.70	9.50	9.86	9.88	10.39
MnO	0.18	0.23	0.12	0.22	0.17	0.21
MgO	9.10	41.91	12.17	10.45	11.78	11.25
CaO	10.93	0.36	10.85	11.33	11.13	11.29
Na_2O	0.40	0.08	2.45	2.30	2.27	2.19
K_2O	0.25	0.01	0.16	0.28	0.17	0.14
P_2O_5	0.18	0.00	0.19	0.02	0.15	0.13
H_2O	2.21	0.55	0.55	1.64	0.46	0.42
total	92.12	96.01	99.25	100.57	100.36	100.84
OH				2.10		
ppm						
F				141.00		
S				681.90		
Cl				72.90		
Sc					26.86	32.19
Rb					1.08	1.37
Sr					188.87	190.63
Y					14.45	16.28
Zr					49.57	52.25
Nb					3.11	3.26
Ba					125.90	128.19
La					3.90	3.54
Ce					11.71	11.29
Pr					1.32	1.48
Nd					7.43	7.04
Sm					1.55	2.21
Eu					1.20	1.26
Gd					2.19	3.53
Dy					2.59	2.93
Er					1.28	1.29
Yb					1.23	1.57
Th						
U						

Major oxides measured using EMPA, H_2O via FT-IR, volatiles (OH, F, S, Cl) by SIMS, and trace elements by LA-ICP-MS

TABLE A-1 cont.

wt%	IP-5-1	IP-5-3	IP-5-4	IP-5-5	IP-5-6	IP-5-7	IP-5-8
SiO_2	45.69	47.68	47.41	45.21	45.12	44.20	44.95
TiO_2	2.12	1.21	1.11	1.24	1.26	0.79	1.13
Al_2O_3	10.64	16.05	15.67	15.81	14.23	15.23	14.57
FeO	12.83	8.64	7.35	11.22	10.08	8.35	8.65
MnO	0.28	0.11	0.18	0.18	0.17	0.17	0.15
MgO	11.09	11.95	15.59	12.56	13.31	10.29	13.34
CaO	11.07	11.41	9.84	11.24	10.90	12.18	10.99
Na_2O	4.83	2.16	2.42	1.58	1.80	4.43	3.45
K_2O	0.78	0.21	0.26	0.21	0.26	0.20	0.27
P_2O_5	0.32	0.25	0.04	0.19	0.32	0.10	0.09
H_2O	0.75	0.71	0.71	0.31	0.79	1.24	1.14
total	100.42	100.37	100.59	99.76	98.24	97.17	98.71
OH							
ppm							
F							
S							
Cl							
Sc	57.68	24.10			25.34	27.25	26.97
Rb	9.86	4.00			4.83	1.42	3.97
Sr	139.86	186.66			156.94	110.05	159.47
Y	43.00	16.69			19.14	16.57	19.45
Zr	209.19	70.56			77.58	45.20	81.63
Nb	15.45	7.74			7.54	3.40	7.83
Ba	308.95	154.91			181.46	148.62	170.88
La	21.33	7.46			7.08	3.87	7.98
Ce	44.03	21.37			22.05	10.04	21.69
Pr	5.61	2.59			2.72	1.37	2.77
Nd	28.30	11.20			11.20	6.46	12.44
Sm	6.28	3.30			3.51	1.68	3.27
Eu	2.01	0.94			1.18	0.78	1.11
Gd	6.93	1.87			3.04	2.15	3.64
Dy	7.60	3.12			3.21	2.58	3.65
Er	4.44	1.95			1.89	2.59	2.71
Yb	4.05	2.09			2.07	1.81	1.91
Th	1.52	0.21			0.20	0.17	0.22
U	0.46	0.06			0.13		0.11

Major oxides measured using EMPA, H_2O via FT-IR, volatiles (OH, F, S, Cl) by SIMS, and trace elements by LA-ICP-MS

TABLE A-1 cont.

wt%	IP-5-9	IP-5-10	IP-5-11	IP-5-12	IP-5-13	GTMF-2-2
SiO_2	46.93	45.64	47.93	46.68	46.33	47.26
TiO_2	1.14	1.10	1.72	1.17	1.16	1.58
Al_2O_3	15.73	15.43	11.19	16.17	14.93	14.49
FeO	7.39	8.09	13.54	7.92	7.41	9.68
MnO	0.13	0.16	0.30	0.14	0.17	0.21
MgO	13.41	11.96	10.18	11.07	11.98	11.70
CaO	10.80	11.22	8.66	11.30	9.84	11.10
Na_2O	2.01	1.97	4.97	2.19	5.46	2.37
K_2O	0.28	0.22	0.60	0.23	0.41	0.55
P_2O_5	0.15	0.29	0.27	0.07	0.16	0.26
H_2O	1.01	0.95	1.58	0.62	1.06	0.63
total	98.97	97.03	100.94	97.56	98.90	99.84
OH					1.10	
ppm						
F					421.90	
S					858.60	
Cl					243.00	
Sc	23.29			50.03	28.09	29.67
Rb	5.14			4.58	4.53	10.58
Sr	173.98			170.61	161.31	209.19
Y	15.74			21.33	17.31	23.44
Zr	63.03			93.33	86.07	116.48
Nb	6.81			6.83	7.02	13.21
Ba	158.23			139.20	177.25	293.59
La	6.90			7.91	8.83	14.01
Ce	20.44			19.35	20.60	35.99
Pr	2.38			2.42	2.29	4.24
Nd	9.43			13.28	11.43	18.59
Sm	2.52			3.91	2.69	4.11
Eu	1.30			1.12	0.91	1.22
Gd	3.36			4.18	2.72	3.56
Dy	3.18			2.34	2.97	4.05
Er	1.90			2.38	1.79	2.49
Yb	1.88			3.55	1.85	2.70
Th	0.18				0.53	0.43
U	0.10				0.18	0.26

Major oxides measured using EMPA, H_2O via FT-IR, volatiles (OH, F, S, Cl) by SIMS, and trace elements by LA-ICP-MS

TABLE A-1 cont.

wt%	GTMF-2-3	GTMF-2-4	GTMF-2-5	GTMF-2-6	GTMF-2-7	GTMF-2-9
SiO_2	46.24	48.63	46.95	43.69	45.15	46.23
TiO_2	1.42	2.24	1.52	1.76	1.28	1.74
Al_2O_3	15.04	11.78	16.42	13.97	14.71	16.26
FeO	8.13	10.92	9.41	12.32	8.27	9.40
MnO	0.13	0.19	0.14	0.22	0.18	0.14
MgO	12.25	13.42	9.74	9.49	12.97	7.47
CaO	11.40	10.39	11.73	11.13	11.12	12.12
Na_2O	2.14	2.44	2.08	3.95	3.35	2.64
K_2O	0.33	0.55	0.43	0.61	0.33	0.54
P_2O_5	0.31	0.50	0.30	0.33	0.31	0.48
H_2O	0.55	0.91	1.07	1.02	0.51	0.69
total	97.93	101.97	99.80	98.50	98.18	97.71
OH						
ppm						
F						
S						
Cl						
Sc	22.26	38.66	23.29	25.02		
Rb	7.20	12.51	7.78	7.08		
Sr	200.76	175.12	194.10	1284.48		
Y	19.89	31.50	21.94	22.19		
Zr	90.61	167.24	126.35	126.01		
Nb	10.31	18.34	14.11	17.63		
Ba	185.54	342.46	207.47	2916.14		
La	9.33	18.51	11.85	8.81		
Ce	27.34	46.56	32.69	22.25		
Pr	3.22	5.58	4.13	2.94		
Nd	14.31	21.71	16.32	12.74		
Sm	3.98	4.60	4.53	3.35		
Eu	1.40	1.80	1.27	1.49		
Gd	3.66	6.06	4.18	4.21		
Dy	4.01	5.49	3.30	4.05		
Er	2.00	3.32	2.06	2.37		
Yb	1.27	4.09	1.81	2.54		
Th	0.31	0.64	0.40	0.37		
U		0.28	0.14	0.28		

Major oxides measured using EMPA, H_2O via FT-IR, volatiles (OH, F, S, Cl) by SIMS, and trace elements by LA-ICP-MS

TABLE A-1 cont.

wt%	GTMF-2-10	GTMF-2-11	GTMF-2-12	GTMF-2-13	GTMF-4-3	GTMF-4-6
SiO_2	44.75	45.59	46.13	44.27	39.30	46.37
TiO_2	1.28	1.31	0.99	1.52	2.72	1.59
Al_2O_3	13.66	14.72	11.93	13.99	12.25	14.66
FeO	11.04	10.61	18.06	11.37	14.59	8.80
MnO	0.16	0.19	0.30	0.12	0.22	0.21
MgO	13.99	11.91	12.68	14.15	11.17	10.80
CaO	10.41	11.10	4.96	11.13	14.90	11.26
Na_2O	2.74	3.35	2.96	2.11	2.09	2.30
K_2O	0.42	0.37	0.71	0.37	0.33	0.35
P_2O_5	0.21	0.29	0.28	0.21	0.43	0.27
H_2O	1.17	0.78	0.58	1.21	1.53	0.91
total	99.82	100.22	99.58	100.43	99.53	97.54
OH	1.27		1.00			
ppm						
F	400.70		689.10			
S	1369.20		423.40			
Cl	182.10		128.50			
Sc	25.59			32.18		
Rb	6.42			5.77		
Sr	158.44			135.01		
Y	18.62			19.83		
Zr	126.59			122.08		
Nb	14.56			12.05		
Ba	488.21			205.66		
La	7.16			8.51		
Ce	22.27			23.01		
Pr	2.58			2.93		
Nd	13.02			12.56		
Sm	3.35			3.55		
Eu	1.23			0.95		
Gd	4.81			3.80		
Dy	3.23			2.83		
Er	2.32			2.33		
Yb	2.07			1.64		
Th	0.40			0.38		
U	0.17			0.16		

Major oxides measured using EMPA, H_2O via FT-IR, volatiles (OH, F, S, Cl) by SIMS, and trace elements by LA-ICP-MS

TABLE A-1 cont.

wt%	GTMF-4-7	GTMF-4-8	GTMF-4-20	GTMF-4-21
SiO_2	45.61	47.23	38.59	43.00
TiO_2	1.34	1.51	1.52	1.91
Al_2O_3	13.03	13.96	14.03	14.20
FeO	10.84	10.04	14.73	11.93
MnO	0.20	0.13	0.21	0.21
MgO	15.81	12.22	9.60	13.37
CaO	9.85	10.45	11.09	11.07
Na_2O	1.50	1.92	1.48	0.92
K_2O	0.35	0.34	0.41	0.29
P_2O_5	0.29	0.27	0.35	0.26
H_2O	1.70	0.47	2.00	1.87
total	100.51	98.54	94.01	99.03
OH	2.00		3.30	
ppm				
F	362.30		459.50	
S	1700.10		897.80	
Cl	185.70		1099.50	
Sc	24.82	56.57		
Rb	5.25	6.84		
Sr	271.26	197.95		
Y	22.19	24.29		
Zr	131.27	117.51		
Nb	13.86	11.59		
Ba	2779.98	205.42		
La	12.83	12.88		
Ce	27.13	28.91		
Pr	3.58	3.16		
Nd	15.53	17.61		
Sm	3.40	4.50		
Eu	1.40	1.31		
Gd	5.02	4.24		
Dy	4.79	3.41		
Er	2.63	2.33		
Yb	1.87	1.26		
Th	0.34	0.67		
U	0.21			

Major oxides measured using EMPA, H_2O via FT-IR, volatiles (OH, F, S, Cl) by SIMS, and trace elements by LA-ICP-MS

Appendix B

Plot of water by FT-IR and by SIMS

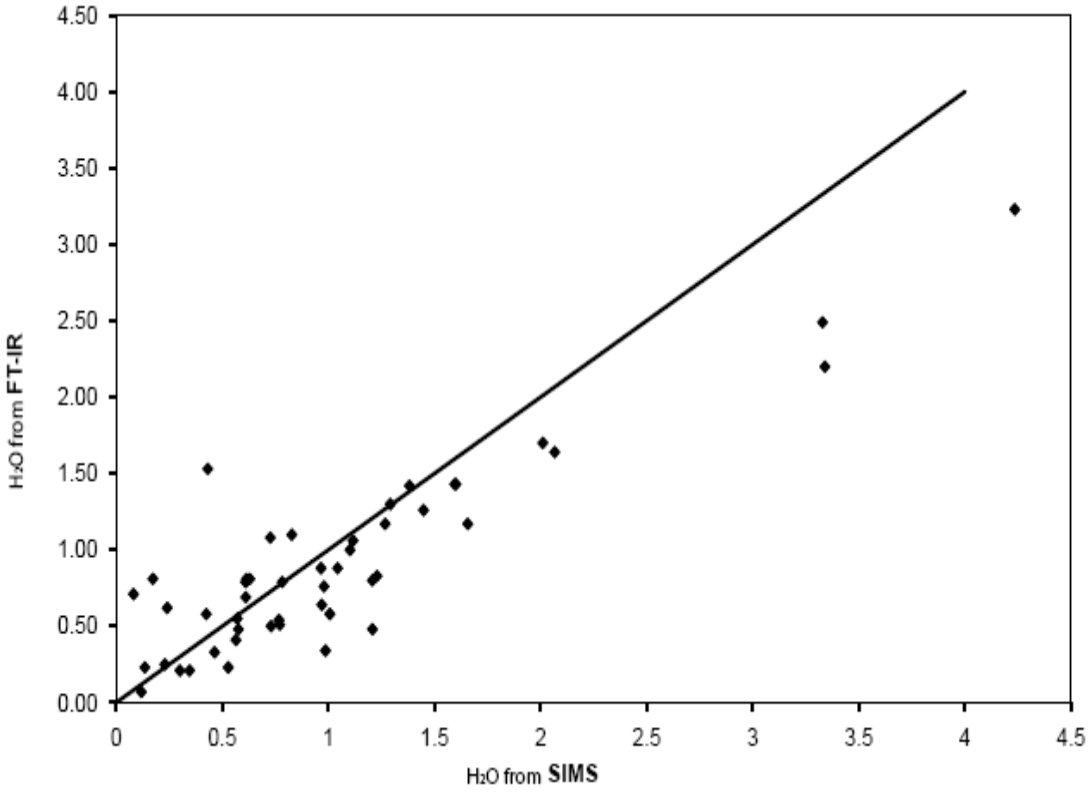

Figure B-1 Plot of H_2O values as measured by FT-IR vs SIMS for olivine-hosted melt inclusions used in chapters 2 and 3 that were analyzed by both methods. The heavy black line indicates 1:1 correlation, showing that FT-IR tends to underestimate H_2O at higher concentrations.

Appendix C

Standards used for EMPA analysis of olivine-hosted melt inclusions

TABLE C-1. Standards used for major element analysis in olivine-hosted melt inclusions using EMPA.

standard	description	elements standardized
ALBL	Langwitz Vals Albite	Na, Al
PX69	Natural Diopside 69-27	Mg, Si, Ca
GKFS	St. Gothard Adularia	K
ILM	Natural Ilmenite	Ti
BHRH	Broken Hill Rhodonite	Mn
FESI	Synthetic Ferrosilite	Fe
BACL	Barium Chlorine Apatite	P

Standards used for EMPA analysis of major elements in olivine-hosted melt inclusions. Standards were analyzed using the same analytical conditions as the melt inclusions